Title

Systematic variations in argon diffusion in feldspars: Constraints on diffusion lengthscales, diffusive anisotropy, and non-linear Arrhenius arrays and implications for noble gas thermochronometry

Author

Cassata, William

Publication Date

2012

Peer reviewed|Thesis/dissertation

Systematic variations in argon diffusion in feldspars: Constraints on diffusion lengthscales, diffusive anisotropy, and non-linear Arrhenius arrays and implications for noble gas thermochronometry

By

William Cassata

A dissertation submitted in partial satisfaction of the

requirements for the degree of

Doctor of Philosophy

in

Earth and Planetary Science

in the

Graduate Division

of the

University of California, Berkeley

Committee in charge:

Professor Paul R. Renne, Chair
Professor Donald J. DePaolo
Professor Eric B. Norman

Spring 2012

Abstract

Systematic variations in argon diffusion in feldspars:
Constraints on diffusion lengthscales, diffusive anisotropy, and non-linear Arrhenius arrays
and implications for noble gas thermochronometry

By

William Cassata

Doctor of Philosophy in Earth and Planetary Science

University of California, Berkeley

Professor Paul R. Renne, Chair

Information about the time-dependent production and temperature-dependent diffusion of radiogenic argon in feldspars can be used to constrain the thermal evolution of meteorites, mountain belts, intrusive magmatic bodies, and a host of other Earth and planetary processes. To better asses the accuracy of such thermal models, an understanding of the mechanisms, pathways, and processes by which argon diffuses in feldspars is required. In this thesis I present step-heating diffusion experiments conducted on feldspars with diverse compositions, structural states, and microstructural characteristics. The experiments reveal systematic variations in diffusive behavior that appear closely related to these variables, with apparent closure temperatures for 0.1-1 millimeter grains of ~200 to 400 °C (assuming a 10 °C/Ma cooling rate). Given such variability, there is no broadly applicable set of diffusion parameters that can be utilized in feldspar thermal modeling; sample-specific data are required. Diffusion experiments conducted on oriented cleavage flakes do not reveal directionally-dependent diffusive anisotropy to within the precision limits of our approach. Additional experiments aimed at constraining the physical significance of the diffusion domain are presented and indicate that unaltered feldspar crystals with or without coherent exsolution lamellae diffuse at the grain scale, whereas feldspars containing hydrothermal alteration and/or incoherent sub-grain intergrowths do not. Arrhenius plots for argon diffusion in feldspars appear to reflect a confluence of intrinsic diffusion kinetics and structural transitions that occur during incremental heating experiments. These structural transitions, along with sub-grain domain size variations, cause deviations from linearity (i.e., upward and downward curvature) on Arrhenius plots. Detailed descriptions of the structural responses of different feldspars to heating are given, and an atomistic model for coincident Arrhenius behavior is proposed. The resulting implications for accurately extrapolating laboratory-derived diffusion parameters to natural settings and over geologic time are discussed. The data indicate that considerable inaccuracies may exist in published thermal histories obtained using multiple diffusion domain (MDD) models fit to exsolved alkali feldspar Arrhenius plots, where the inferred Ar partial retention zones may be anomalously hot.

To my wife,

Julie

Acknowledgements

I would like to thank my advisor, Paul Renne, for encouraging me to pursue argon diffusion in feldspars, and for providing me with the resources, facilities, and guidance to work on a broad array of research problems while at Berkeley. He has been an inspirational mentor, advisor, and collaborator, for which I am ever grateful.

I would also like to thank David Shuster for expanding my research horizon beyond the terrestrial realm to include planetary science, an endeavor of which I have grown quite fond. In my time at Berkeley I learned much about the scientific method, experimental design, and collaborative research through my interactions with David.

I am also grateful to Tim Becker for his expertise, and patience, in the lab. Tim has been an invaluable resource for me during the past five years, and his approach to experimental design and technical diagnostics will be my guide in the future.

Al Deino and Greg Balco are thanked for laboratory assistance, Sean Mulcahey and Kent Ross for electron microprobe assistance, Darren Mark and Kevin Righter for generously providing samples, Tim Teague for making thin sections and grain mounts, and Becky Smith for orienting cleavage flakes using an SEM. I am grateful to Rudy Wenk for helpful discussions regarding feldspar structures and for access to his collection of plagioclase samples.

I acknowledge financial support from the U.S. National Science Foundation Petrology and Geochemistry Program (grant EAR- 0838572 to P.R.R. and D.L.S.) and the Ann and Gordon Getty Foundation. I was supported by a National Science Foundation Graduate Research Fellowship.

Contents

Chapter 1.

Introduction

1.1 Thermochronometry

Minerals containing radioactive isotopes accumulate decay products over time. If the rate of decay is known and the parent and daughter isotopes are quantitatively retained, one can determine the age of a rock by comparing the relative isotopic abundances. However, transmutations caused by radioactive decay tend to yield daughter products that are not compatible in host minerals (e.g., noble gases), and are therefore readily lost by dissolution-reprecipitation reactions, metamorphic recrystallization, and/or thermal diffusion. The latter process, which is ubiquitous within Earth's crust, is highly sensitive to the size and charge of the diffusant, composition and structure of the host mineral, and ambient temperature. As a result, minerals present in a given rock often yield different radioisotopic ages that reflect mineral-specific diffusion kinetics and the time-temperature history of the rock. For example, a granite that is slowly uplifted to Earth's surface from depth progressively cools through the closure temperatures (Dodson, 1973) for argon diffusion in hornblende, biotite, and alkali feldspar, where the closure temperature represents the temperature of a mineral at the time given by its radioisotopic age and is determined empirically via laboratory diffusion experiments. Minerals with higher closure temperatures yield older apparent ages and vice versa. By interpolating between these ages a cooling history can be reconstructed, provided that the mineral-specific closure temperatures are known. Thus one can exploit open-system behavior to determine the thermal history, or thermochronometry, of a rock.

Thermochronometry by the $^{40}Ar/^{39}Ar$ technique provides insights into an array of planetary processes that span immense time and temperature regimes, from rapid and high temperature bolide impact events (e.g., Cassata et al., 2010) to mountain uplift occurring over plate tectonic timescales at near surface temperatures (e.g., Richter et al., 1991). Applications of thermochronometry continue to grow in number and diversity in the Earth and planetary sciences, and numerical models based on thermochronometric data have become increasingly sophisticated (e.g., Braun, 2005; Cassata *et al.*, 2010; Ehlers, 2005; Ehlers *et al.*, 2005; Reiners *et al.*, 2005; Reiners and Shuster, 2009; Shuster *et al.*, 2005, 2010; Simoes *et al.*, 2007). Feldspars, being rich in potassium (K) and abundant in most terrestrial and extraterrestrial rocks, are ideal targets for thermochronometry. Ar diffusion in K-feldspar has been a topic of extensive research throughout the past 40 years, due, in part, to the ease with which high-resolution age and kinetic data can be simultaneously acquired (e.g., Foland, 1974; Lovera et al., 1989; 1991; 1997; 2002; Harrison et al., 1991; Arnaud and Kelley, 1997; Wartho et al., 1999). The kinetics of Ar diffusion plagioclase, the most abundant mineral in

Earth's crust, have been less extensively researched, although various samples have been analyzed for specific thermochronometric applications (e.g., Berger and York, 1981; Harrison and McDougall, 1981; Onstott et al., 1989; Renne et al., 1990; 1996; Boven et al., 2001; Garrick-Bethell et al., 2009; Cassata et al., 2009; Shuster et al., 2009). In general, inferred activation energies (E_a) for Ar diffusion in feldspars vary between 100 and 350 kJ/mole and frequency factors ($\ln(D_o/a^2)$) span fourteen orders of magnitude (see reviews by Lovera et al., 1997; Cassata et al., 2009; Forster and Lister, 2010). Despite years of research, an explanation for such variability has proven elusive, and our basic understanding of the mechanisms, pathways, and processes by which Ar diffuses within feldspars remains, in many regards, fragmentary.

In a seminal paper on Ar diffusion in orthoclase, Foland (1974) established that physical grain dimensions define, at least in some instances, the diffusive lengthscale, based on equivalent values for the diffusion coefficient D obtained from grains that differed in size by a factor of four. Likewise, physical grain dimensions are inferred to be the effective diffusive lengthscale for He transport in apatite, titanite, and zircon (Harrison & Zeitler, 2005). Subsequent observations of non-linear Arrhenius arrays for Ar diffusion in alkali feldspar and tiered age spectra, neither of which are consistent with a uniform distribution of Ar within a single diffusion domain, prompted the development of multiple diffusion domain (MDD) theory (Lovera et al., 1989; 1991; Harrison et al., 1991). According to MDD theory, deviations from linearity manifest on essentially all alkali feldspar step-heating Arrhenius plots reflect the exhaustion of sub-grain domains of increasing size, each of which is non-interacting and stable during and following cooling through the Ar partial retention zone. Such sub-grain domains are often reconcilable with microscopic characteristics of a sample (e.g., fractures and/or cleavage planes), but in other instances are more ambiguous. Interestingly, "gem-quality" alkali feldspars that have been shown to diffuse at the grain-scale based on *in-situ* observations of surface to core concentration gradients obtained using a UV-laserprobe (Arnaud and Kelley, 1997; Wartho et al., 1999) also yield non-linear Arrhenius arrays when incrementally degassed, which indicates that such behavior may not solely arise due to a range in sub-grain domain sizes. Although a causal explanation remains elusive, deviations from linearity have nonetheless been interpreted in terms of sub-grain domain structure, and MDD theory applied to alkali feldspars is widely utilized to constrain thermal histories in a variety of tectonic settings (e.g., Richter et al., 199l; McLaren and Dunlap, 2006; Karlstrom et al., 2010).

Since the development of MDD theory, it has drawn considerable criticism from thermochronologists and mineralogists that challenge the validity of fundamental assumptions underlying the approach. In particular, the assumption that sub-grain domains are non-interacting (i.e., separated by infinite reservoirs) has been called into question, prompting the development of a multi-path approach to diffusion modeling (volume plus pipe/short-circuit diffusion; Lee, 1995). It has also been suggested that non-linearity observed on alkali feldspar Arrhenius plots reflects the confluence of complex chemical, microtextural, and structural changes that occur both over geologic time and during laboratory heating, and that cooling histories cannot be derived from age spectra and Arrhenius plots (Parsons, 1999). Moreover, the assumption that diffusive loss of Ar is Fickian (i.e., Ar moves from a region of high to low

concentration with a magnitude proportional to the concentration gradient) has been disputed (Villa, 2006). Villa (2010) argues that discordance observed on $^{40}Ar/^{39}Ar$ age spectra depends more on the availability of recrystallization-enhancing fluids than on a heat source.

Efforts to resolve apparent inconsistencies between MDD theory and mineralogical observations are on-going. McLaren et al. (2007) found that alkali feldspars with pristine, strain-controlled cryptoperthite from the Klokken syenite yielded thermal histories consistent with independent constraints, whereas alkali feldspars with patch (locally recrystallized) perthite did not, presumably due to domain modification and Ar loss resulting from fluid-rock interactions. Likewise, Lovera et al. (2002) cautioned against the use of recrystallized alkali feldspars in MDD modeling, noting a lack of correlation between age spectra and diffusion data. By obtaining *in-situ* ^{40}K-^{40}Ca ages using secondary ion mass spectrometry, Harrison et al. (2010) confirmed that both K and Ca were mobilized by non-thermal, fluid-assisted recrystallization in Klokken feldspars, rendering them poor candidates for MDD modeling. Increasingly, detailed microstructural investigations are being used in coordination with $^{40}Ar/^{39}Ar$ data to better constrain complex thermal histories and determine which alkali feldspars are suitable for thermochronometry (e.g., Sanders et al., 2007; McLaren and Reedy, 2008; Parsons et al., 2010; Heizler et al., 2007; 2010; Short et al., 2010).

Notwithstanding the aforementioned studies, myriad unanswered questions remain regarding the physical significance of the diffusion domain, the stability of the diffusion domain, both over geologic time and during laboratory heating experiments, the isotropy of diffusion, the potential importance of structural state on diffusivity, and the possible pressure-dependence of diffusivity. To address these fundamental questions, we conducted diffusion experiments on feldspars whose diverse compositions, structural states, and microstructural characteristics span the natural variability of ternary feldspars. In this paper we present the results of these diffusion experiments and, together with existing data on Ar diffusion in silicates, develop a framework for interpreting Arrhenius non-linearity and systematic inter-sample variability in laboratory-derived diffusion parameters. We close with a discussion on accurately extrapolating laboratory-derived diffusion parameters to natural settings and over geologic time.

Chapter 2.

Samples and Methods

2.1 Samples

Diffusion experiments were conducted on feldspars that (1) range in composition from nearly pure orthoclase to nearly pure anorthite, (2) have diverse microtextures, (3) range in structural state from fully ordered to fully disordered, and (4) derive from diverse lithologies, including granites, pegmatites, basalts, gabbros, meteorites, tuffs, and metamorphic rocks. An electron microprobe (EPMA) was used to characterize the spatial distribution of K, Na, and Ca in each sample. Many of the specific samples discussed in this paper have been the topic of extensive mineralogical research throughout the past 50 years and have been characterized using transmission electron microscopy (TEM) and x-ray diffraction (XRD) techniques. Brief descriptions of each sample and compositional data are given in Table 2.1 and throughout the text.

Table 2.1: Sample information

Sample	Locality	Phase	Lithology	Structure	An	Ab	Or
BMk	Benson Mines, NY, USA	Orthoclase	Granitic Pegmatite	*C2m*	0.0	3.0	97.0
XTALk	Ecstall Pluton, BC, Canada	Orthoclase	Granodiorite Pluton	*C2m/C1*	0.1	11.3	88.6
MADk	Itrongay, Madagascar	Cyptoperthite	Granitic Pegmatite	*C2m/C1*	0.2	5.6	94.6
BV-8k	Bushveld Complex, S. Africa	Perthite	Gabbro	*C2m/C1*	0.8	22.6	76.6
FCs	Fish Canyon Tuff, CO, USA	Sanidine	Rhyolitic Ignimbrite	*C2m*	1.0	27.0	72.0
GSs	Gulf of Salerno, Italy	Sanidine	Rhyolitic Ash	*C2m*	3.7	30.5	65.8
ECCa	Easy Chair Crater, NV, USA	Anorthoclase	Alkali Basalt Lava	*C1*	10.8	71.8	17.4
GRAp	Extraterrestrial (GRA 06128)	Albite/Olig.	Plutonic Achondrite	*C1*	14.1	84.1	1.9
ML-15p	Mono Lake, CA, USA	Oligoclase	Rhyolitic Ash (#15)	*C1*	19.6	74.2	6.2
XTALp	Ecstall Pluton, BC, Canada	Oligoclase	Granodiorite Pluton	*C1*	20.8	77.7	1.5
FCp	Fish Canyon Tuff, CO, USA	Olig./Andesine	Rhyolitic Ignimbrite	*C1*	29.8	61.7	4.5
BG-1p	Bushveld Complex, S. Africa	Andesine	Gabbro	*C1*	38.9	59.4	1.7
PR-92p	Paraná-Etendeka LIP, Brazil	Andesine	Rhyodacite Lava	*C1*	41.1	54.6	4.3
NCp	Nain Complex, NL, Canada	Labradorite	Anorthosite	e_1/e_2	49.4	47.9	2.7
HMS-2p	Klamath Mtns., CA, USA	Labradorite	Basaltic Sill	*C1*	52.8	44.2	3.0
SURTp	Surtsey, Iceland	Labradorite	Alkali Basaltic Lava	*I1*	59.6	39.6	0.8
OREGp	Plush, OR, USA	Labradorite	Basaltic Lava	*I1*	63.9	35.4	0.7
BV-8p	Bushveld Complex, S. Africa	Labradorite	Gabbro	e_1	67.4	31.3	1.3
DCp	Duluth Complex, MN, USA	Bytownite	Anorthosite	$e_1/P1$	74.7	24.9	0.4
VZ699	Verzasca Valley, Switzerland	Bytownite	Granitoid	$e_1/P1$	86.2	13.5	0.3
SW-1	Stillwater Comlpex, MT, USA	Bytownite	Anorthosite	$e_1/P1$	86.7	13.0	0.3
GV-09	Grass Valley, CA, USA	Anorthite	Anorthosite	*P1/T*	94.2	5.2	0.6
JAPp	Miyake, Japan	Anorthite	Basaltic Lava	*T*	96.2	3.7	0.1
TROCp	Lunar (76535)	Anorthite	Plutonic Troctolite	*P1*	96.2	3.5	0.3

2.2 Experimental Methods

Individual equant to elongate crystal fragments and cleavage-bounded sheet like flakes devoid of obvious microfractures were hand-picked under a binocular microscope and irradiated for 50 to 200 hours at the Oregon State University TRIGA reactor in the Cadmium-Lined In-Core Irradiation Tube (CLICIT) facility. Following irradiation, single grains were loaded into small packets (~5 x 3 x 1 mm^3) made from high-purity Pt-Ir alloy tubes and incrementally degassed using feedback-controlled laser heating with either a 30 or 150 W diode laser (λ = 810 ± 10 nm). Temperature was monitored using a type-K thermocouple mounted within the Pt-Ir packets or using an optical pyrometer coaxially aligned with the diode laser. To account for the temperature dependent emissivity of the Pt-Ir packets, we routinely calibrated the single-color pyrometer output against a type-K thermocouple under high vacuum (<10^{-8} torr) and under the same conditions as the diffusion experiments (i.e., same viewport, coverslide, focal point, etc.). Additional information regarding the heating and temperature measurement methodology can be found in Cassata et al. (2009) and Shuster et al. (2010).

During experimental heating, the samples were held at temperatures between 300 and 1500 °C for durations of 180 to 15000 seconds. Typical durations required to reach set-point temperatures were <10 seconds. Samples cool to significantly below set-point temperatures in roughly equivalent durations. Precision on all temperature measurements is better than 5 °C. Accuracy on type-K thermocouples is approximately 0.4% (Croarkin et al., 1993). The precision of the pyrometer-to-thermocouple calibration is ~10 °C (Cassata et al., 2009). Following heating, the released argon was purified using two SAES getters (one hot and one cold), analyzed using a Mass Analyzer Products 215c mass spectrometer, and measured statically on a Balzers SEV-217 electron multiplier using procedures similar to those described by Renne et al. (1998). Most crystals were heated in excess of their nominal melting temperatures and were completely fused following incremental heating.

Raw isotope measurements were corrected for interfering nuclear reaction products (Renne et al., 2005), ^{37}Ar and ^{39}Ar decay, spectrometer discrimination, and extraction line blanks. Using the fraction of degassed Ca-derived ^{37}Ar for plagioclase or K-derived ^{39}Ar for alkali feldspar and the duration of each extraction, we calculate the diffusion coefficient (D) normalized to the characteristic length scale (D/a^2) using the equations of Crank (1975) following the algorithm of Fechtig and Kalbitzer (1966). Uncertainties in D/a^2 values were calculated based on the analytical precision of each step. Spherical geometry was used for equant to elongate grains and infinite sheet geometry for cleavage flakes. Inaccurate or inappropriate choices of diffusion geometry result in erroneous vertical displacements of Arrhenius arrays, with maximum and typical errors of 2.2 and <0.5 natural log units, respectively (Huber et al., 2011). The temperature dependence of the diffusion coefficients was quantified from weighted linear regression models of $\ln(D/a^2)$ against T^{-1}. Incremental releases of ^{36}Ar, ^{38}Ar, and ^{40}Ar were also measured, but will not be discussed in this paper. Systematic mass-dependent variations in ^{37}Ar and ^{39}Ar diffusivity were not observed (discussed in Chapter 8), nor were systematic variations in diffusivity related to irradiation duration.

Chapter 3.

What defines the diffusion domain?

3.1. Evidence for grain-scale diffusion in compositionally homogeneous and cryptoperthitic feldspars

To determine whether or not the physical crystal dimensions define the diffusion domain in unaltered, compositionally homogeneous and cryptoperthitic feldspars and to test for diffusive isotropy, we conducted detailed diffusion experiments on thin cleavage flakes of two extensively studied alkali feldspars: a cryptoperthite ($An_{0.2}Ab_{5.5}Or_{94.3}$) from a shallowly emplaced pegmatite near Itrongay, Madagascar (Coombs, 1952) and an orthoclase ($An_{0.0}Ab_{3.0}Or_{97.0}$) from a pegmatite in Benson Mines near Star Lake, New York, USA (Foland, 1974). Detailed descriptions of the mineralogy, albite lamellae, and "tweed" microtexture characteristic of the orthoclase lamellae in our sample of Madagascar cryptoperthite can be found in Arnaud and Kelley (1997), Wartho et al. (1999), and Parsons and Lee (2005). Benson Mines orthoclase was described by Foland (1974) as clear and colorless, compositionally homogeneous, and without alteration, zoning, or twinning. Our sample of Benson Mines orthoclase has a pinkish hue due to small, pervasively distributed iron oxide inclusions.

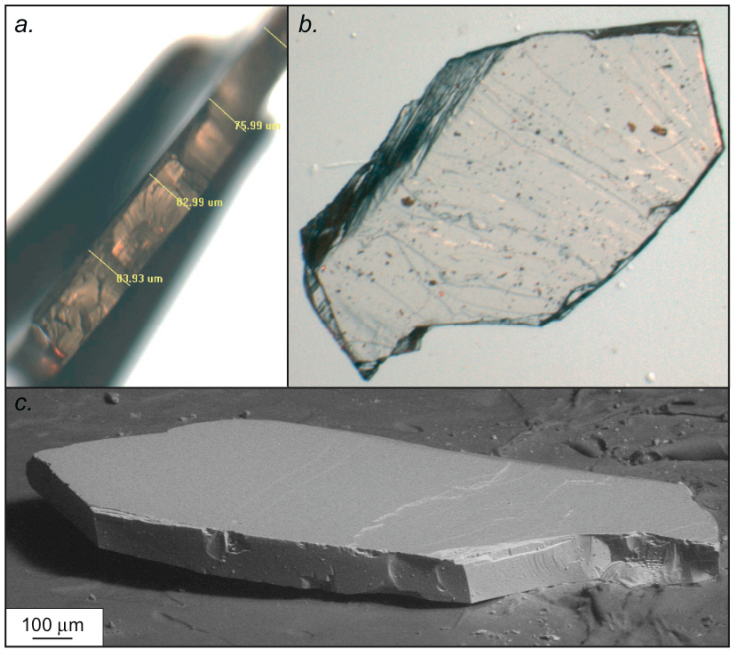

Figure 3.1: Images of typical cleavage flakes analyzed for Ar diffusion kinetics. (**a**) Binocular microscope image and thickness measurement of a Plush labradorite {001} cleavage flake. (**b**) Binocular microscope image of a Benson Mines orthoclase {001} cleavage flake. (**c**) Scanning electron microscope image of the same Benson Mines orthoclase cleavage flake shown in (**b**). Cleavage flake orientations were determined using electron backscatter diffraction patterns (see text for details).

If sub-grain features such as "tweed" domain boundaries or cryptoperthite lamellar interfaces define the diffusion domain (i.e., define a in D/a^2), then individual fragments of a microtexturally homogeneous megacryst should yield the same value of D/a^2 at a given temperature irrespective of macroscopic grain dimensions. Conversely, if physical grain dimensions define the diffusion domain, then the fractional loss of gas (i.e., the calculated

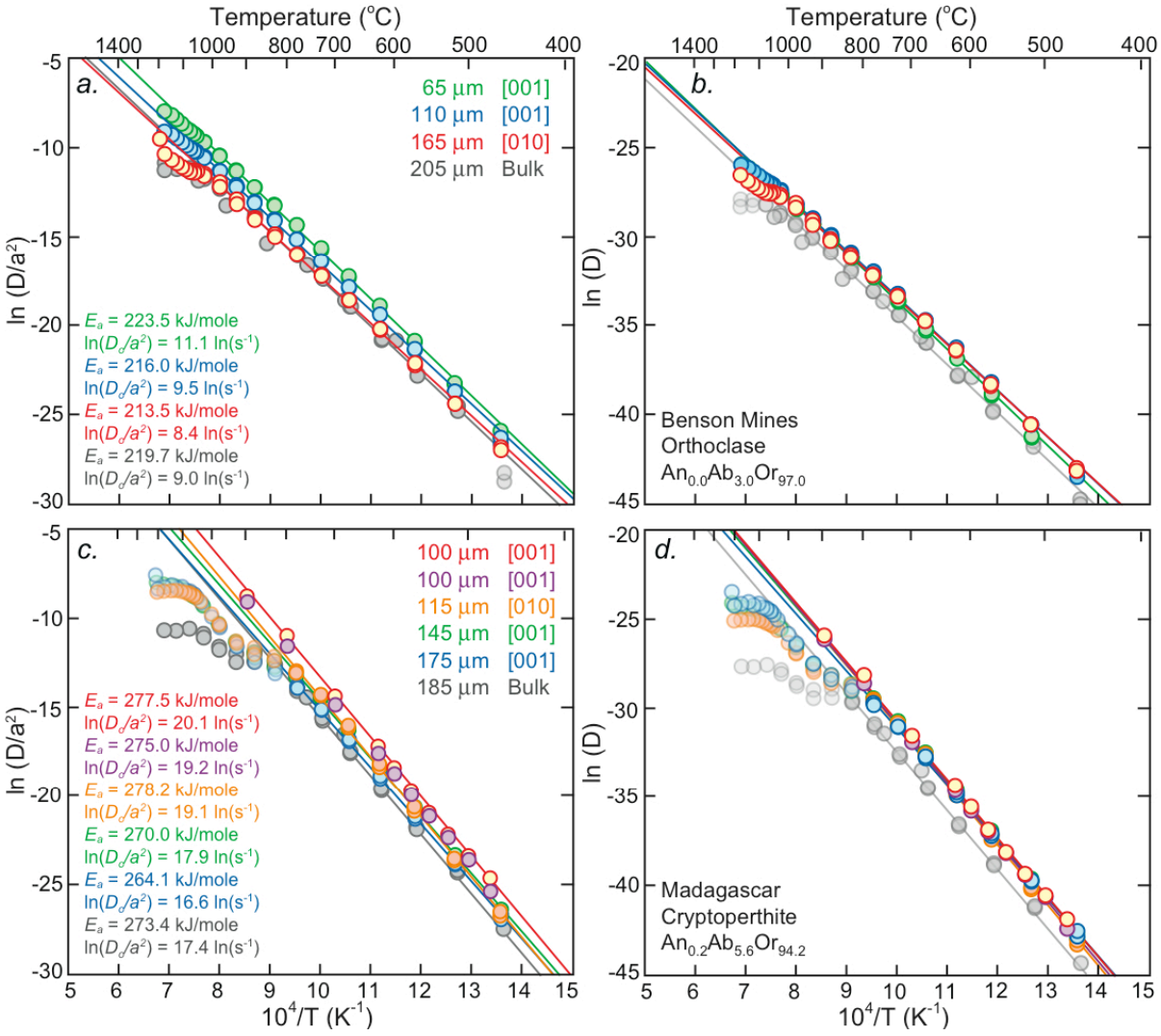

Figure 3.2: Arrhenius plots for prograde heating of (**a**,**b**) Benson Mines orthoclase (^{39}Ar) and (**c**,**d**) Madagascar cryptoperthite (^{39}Ar) crystals, calculated using equations for infinite sheet geometry for cleavage flakes and spherical geometry for equant (bulk) grains. Uncertainties in D/a^2 values are generally smaller than the symbols, but are not shown. Cleavage flake thickness and equant grain radii are listed in (**a**) and (**c**). Data shown in (**b**) and (**d**) were calculated by multiplying the D/a^2 values shown in (**a**) and (**c**) by half the thickness of the cleavage flake or the equant grain radius. Anisotropy is not resolvable between {001} and {010} cleavage flakes at low-T (<800 °C). Apparent discrepancies between equant grain and cleavage flake D values can be explained by our use of spherical geometry to model tetragonal prisms (see text for discussion; Huber et al., 2011).

D/a^2 value) associated with a given temperature extraction should vary inversely with the square of grain size. Thus by analyzing cleavage flakes that differ in thickness, one can assess whether or not the diffusion domain is defined by sub-grain features. We analyzed individual cleavage flakes that varied in thickness by a factor of two. Care was taken to select grains with high aspect ratios (e.g., >10:5:1) so as not to bias D/a^2 values calculated using analytical solutions for infinite sheet geometry[1]. Following grain selection, the width of each cleavage flake was measured using a binocular microscope (Fig. 3.1). Half the thickness of each grain was assumed to be the relevant diffusive lengthscale for infinite sheet geometry. The results of the diffusion experiments are shown both normalized and un-normalized to the measured half-widths in Figure 3.2.

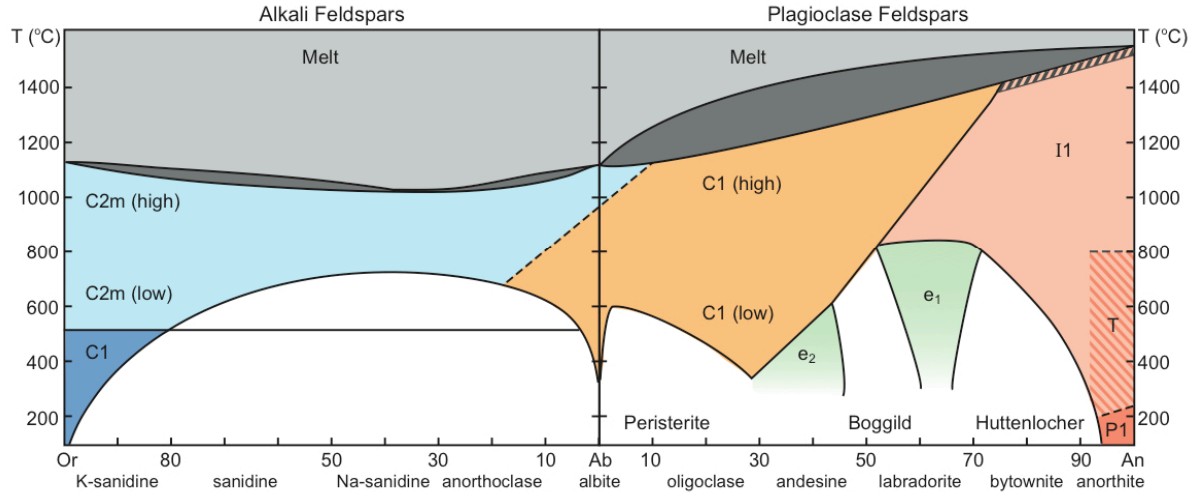

Figure 3.3: Phase diagram for alkali and plagioclase feldspars [redrafted and modified from Parsons (2010)]. Dashed and solid lines represent displacive and order-disorder transitions, respectively. *C1*, *I1*, *P1*, *T*, e_1, and e_2 feldspars are triclinic. *C2m* feldspars are monoclinic. A detailed description of *T*-anorthite is given in the text. The striped field above the *I1* field represents a metastable extension of the *C1* field.

By inspection of Figure 3.2 it is evident that thinner cleavage flakes yield higher values of D_o/a^2 at a given temperature and vice versa. When multiplied by the square of the cleavage flake half-width, each aliquot yields equivalent values of D at a given temperature. Thus differences in D_o/a^2 values can be explained by differences in macroscopic grain dimensions, which indicates that the physical crystal dimensions define the diffusion domain in these unaltered cryptoperthite and orthoclase feldspars. Wartho et al. (1999) reached an equivalent conclusion based on *in-situ* laser ablation observations of grain-scale, rim to core concentration gradients in preheated fragments of Madagascar cryptoperthite. Likewise, Foland (1974) and Foland and Xu (1991) inferred grain scale diffusion from fragments of Benson Mines orthoclase based on bulk loss experiments. It follows that the non-linearity observed at high-T on the Madagascar cryptoperthite Arrhenius plot (Fig. 3.2) is conclusively

[1] Grains with aspect ratios that deviate from ideal infinite sheet geometry yield erroneously high D/a^2 values, where the maximum error is 2.2 natural log units for a perfect sphere (Huber et al., 2011).

not due to a distribution of sub-grain domain sizes (discussed in detail in Chapter 5).

3.2. Evidence for grain-scale diffusion in exsolved plagioclase feldspars

In at least some instances, plagioclase crystals with sub-micron to micron-sized exsolution lamellae associated with slow cooling beneath the Huttenlocher and Boggild solvi (Fig. 3.3) appear diffuse at the grain scale. To illustrate this point we use data obtained from a gabbroic labradorite/bytownite ($An_{\sim 70}$) from the Bushveld Complex, South Africa (Cassata et al., 2009). SEM images of the plagioclase crystals discussed herein reveal sub-micron intergrowths (Fig. 3.4a), which, based on the composition, are *e*-plagioclase and anorthite

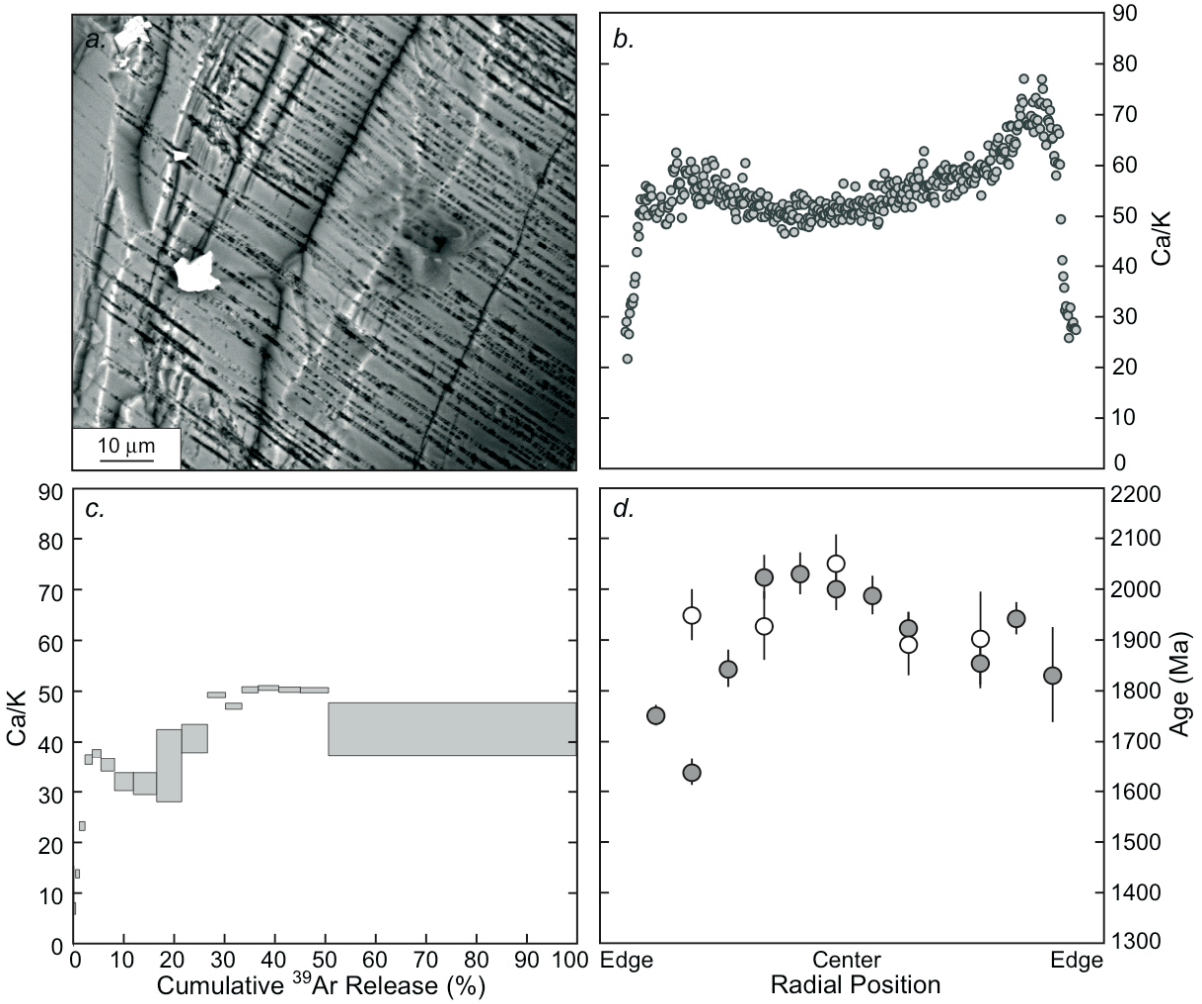

Figure 3.4: (**a**) Scanning electron microscope image of an HF-etched labradorite crystal from the Bushveld Complex. (**b**) Compositional data from an electron microprobe grain traverse. (**c**) $^{37}Ar_{Ca}/^{39}Ar_K$ spectrum derived from an incremental degassing experiment (Cassata et al., 2009). (**d**) *In-situ* $^{40}Ar/^{39}Ar$ dating results from UV-laserprobe grain traverses. The $^{37}Ar_{Ca}/^{39}Ar_K$ spectrum exhibits similar compositional variations to those observed *in-situ* by EPMA, indicating initial extractions sample gas from grain margins. Likewise, *in-situ* $^{40}Ar/^{39}Ar$ ages reveal young apparent ages at grain margins, consistent with grain scale diffusion.

lamellae resulting from slow-cooling beneath the Huttenlocher solvus, consistent with observations of other plagioclase crystals from the Bushveld Complex (e.g., McLaren, 1974). They exhibit normal zoning, with significant (up to 2X) K enrichment and subtle (<15%) Ca depletion near grain margins (Fig. 3.4b; Cassata et al., 2009). In Figure 3.4 we show an SEM image of an HF-etched crystal, compositional data from an electron microprobe traverse, an $^{37}Ar_{Ca}/^{39}Ar_K$ spectrum, and *in-situ* UV-laserprobe $^{40}Ar/^{39}Ar$ dating results. The $^{37}Ar_{Ca}/^{39}Ar_K$ spectrum obtained from the step-wise degassing of a ~1 mm crystal fragment (Fig. 3.4c) mirrors the rim to core compositional variations observed *in-situ* by EPMA (Fig. 3.4b). If this sample comprised a distribution of sub-grain domains, the Ca/K spectra would homogenize rim to core compositional variations in Ca and K, which is not observed. Likewise, age spectra (Cassata et al., 2009) conform to single-domain diffusion theory (i.e., they are not tiered) and *in-situ* laser ablation $^{40}Ar/^{39}Ar$ dating experiments reveal young apparent ages at grain margins that increase toward the center (Fig. 3.4d). Thus it appears that the physical grain dimensions of this sample define the diffusion domain and therefore micron-scale, strain-controlled intergrowths of *e*-plagioclase and anorthite do not provide pathways for efficient loss of Ar to grain surfaces.

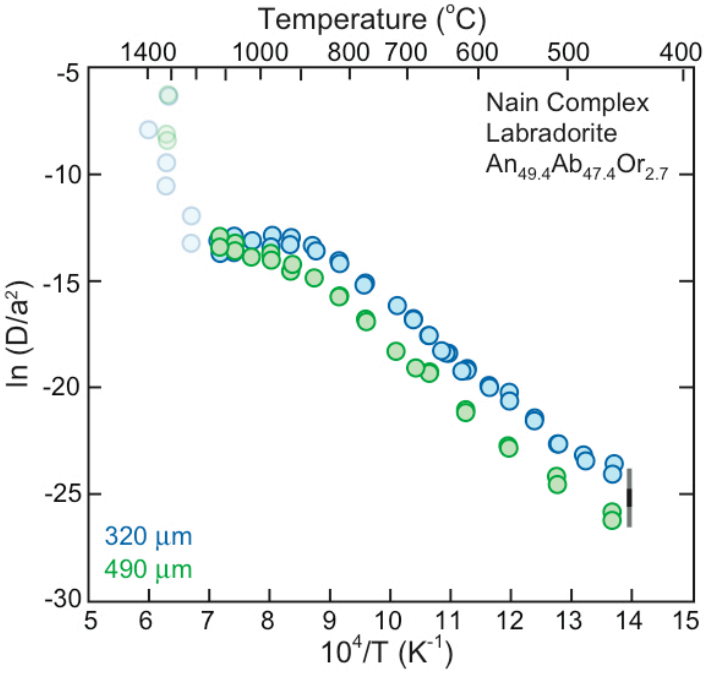

The lack of correlation between lamellar microstructure and diffusive loss is further illustrated by diffusion experiments conducted on Schiller labradorite crystal fragments ($An_{49.5}Ab_{47.9}Or_{2.6}$) from the type locality near Nain, Canada (e.g., Wenk and Nakajima, 1980). The labradorite crystals comprise ~100 nm thick exsolution lamellae with compositions of ~An_{35} and ~An_{65}, each of which has a modulated *e*-plagioclase structure with albite-like and anorthite-like domains separated by anti-phase boundaries (APBs; Wenk and Nakajima, 1980). The lamellar interfaces are mostly coherent, but contain some dislocations at

Figure 3.5: Arrhenius plots for prograde heating of Nain Complex labradorite (^{37}Ar) crystals, calculated using equations for spherical geometry. Uncertainties in D/a^2 values are generally smaller than the symbols, but are not shown. Approximate grain radii (listed in the lower left corner) are based on estimated grain volumes calculated from the total yield of ^{37}Ar, assuming spherical geometry. The vertical black bar shown at low-T represents the expected offset between the arrays based on differences in grain size. The vertical gray bar represents additional discrepancies that might arise due to geometric variations. Grains with aspect ratios that deviate from ideal spherical geometry yield erroneously low D/a^2 values, where the maximum error is 2.2 natural log units (Huber et al., 2011).

misaligned *e*-plagioclase fringes (Wenk and Nakajima, 1980). The sample also contains sparsely distributed, ~1 um thick, K-rich exsolution lamellae and zircon and magnetite inclusions. Arrhenius arrays obtained from equant crystal fragments that differ in size by a factor of approximately 1.5 have nearly identical structure but are displaced vertically, where the larger grain yields lower D/a^2 values at a given temperature (Fig. 3.5). At low-T, the offset between arrays (~1.4 natural log units) is slightly larger than expected based on grain size variations (~0.8 natural log units), which may be due to differences in the aspect ratios of the individual crystals (discussed above; Huber et al., 2011). If exsolution lamellae defined the diffusion domain, each fragment, regardless of size, would yield the same D/a^2 value at a given temperature because they have the same lamellar microstructure. Therefore our experiments corroborate the conclusion of Parsons (1999) that strain-controlled, coherent microstructures do not provide fast-pathways for diffusion, but rather define interfaces within complex domains. We discuss the curvilinear structure of the Arrhenius arrays shown in Figure 3.5 at greater length in Chapter 5.

3.3. Evidence for sub-grain domains in altered, fractured, and inter-grown feldspars

To contrast with the previous sections, here we present results of diffusion experiments conducted on fragments of deuterically altered alkali feldspar from the Bushveld Complex, South Africa ($An_{0.8}Ab_{19.0}Or_{80.2}$). The alkali feldspar crystals contain strain-controlled, coherent to semicoherent film perthite with ~1 um thick Na-rich lamellae and ~3 um thick K-rich lamellae (Fig. 3.6). Deuteric alteration is pervasive, with incoherent (microporous) patch and vein perthite replacing film perthite (e.g., Parsons et al., 2005). Arrhenius arrays obtained from crystals that differ in size by a factor of approximately 2.5 do not reveal size-dependent vertical displacements (Fig. 3.6). The similarity of the low-T portions of the Arrhenius plots, irrespective of the macroscopic grain dimensions, suggests that each crystal fragment contains comparably sized sub-grain domains. These experiments corroborate the conclusions of Parsons (1999) that deuteric microtextures provide efficient pathways for Ar loss, and thus define diffusion domains.

Arrhenius arrays consistent with a range of diffusive lengthscales were also obtained from microstructurally complex plagioclase crystals that contain sub-grains and/or alteration. For example, in Panel 1 of Figure 3.7 we show a backscattered electron image of a bytownite ($An_{86.2}Ab_{13.5}Or_{0.3}$) from a metamorphosed Alpine granitoid from Verzasca Valley in Switzerland (VZ699; Wenk, 1979). The granitoid was subjected to regional-scale, amphibolite facies metamorphism (Wenk, 1979). Plagioclase crystals comprise sub-micron intergrowths of anorthite and *e*-plagioclase (Wenk, 1979) associated with slow-cooling beneath the Huttenlocher solvus (Fig. 3.3) and contain quartz sub-grains and alkali feldspar intergrowths. The Arrhenius array obtained from this sample (Fig. 3.7a) is sub-horizontal and consistent with incoherent sub-grain boundary interfaces between quartz, plagioclase, and alkali feldspar defining diffusion domains. In Panel 2 of Figure 3.7 we show a backscattered electron image of a bytownite ($An_{86.7}Ab_{13.5}Or_{0.3}$) from an anorthosite from the Stillwater Complex, a layered mafic intrusion in Montana, USA. Comparable feldspars from the Stillwater Complex (Nord et al., 1974) comprise sub-micron (~125 Å) *e*-plagioclase and

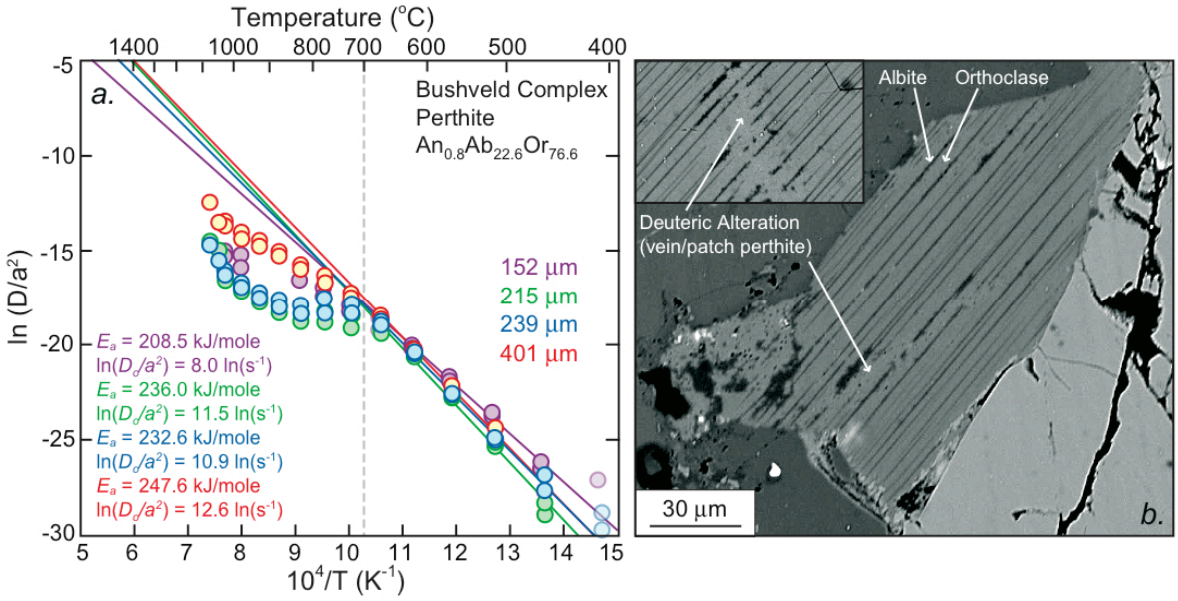

Figure 3.6: (**a**) Arrhenius plots for prograde heating of Bushveld Complex perthite (^{39}Ar) crystals, calculated using equations for spherical geometry. Uncertainties in D/a^2 values are generally smaller than the symbols, but are not shown. Approximate grain radii (list in the lower, left corner) are based on estimated grain volumes calculated from the total yield of ^{39}Ar, assuming spherical geometry. (**b**) Backscattered electron microprobe images illustrating the perthitic microtexture. The crystals comprise strain-controlled film perthite with ~1 um thick Na-rich lamellae (darker) and ~3 um thick K-rich lamellae (lighter) and deuteric patch and vein perthite crosscutting and obscuring the film perthite. The Arrhenius arrays do not reveal size-dependent vertical displacements, which indicates these crystals comprise sub-grain domains that are probably defined by the porous, microcrystalline deuteric alteration.

anorthite exsolution lamellae associated with slow-cooling beneath the Huttenlocher solvus (Fig. 3.3). The plagioclase crystals are extensively altered, with veins of muscovite and porous, microcrystalline Na-rich feldspar replacing bytownite. The non-linear Arrhenius array obtained from this sample (Fig. 3.7b) is consistent with alteration veins defining diffusion domains. In Panel 3 of Figure 3.7 we show a backscattered electron image of an anorthite ($An_{94.2}Ab_{5.2}Or_{0.6}$) from a plutonic anorthosite near Grass Valley, California, USA (Rainey and Wenk, 1978). The feldspar comprises *P1*- and *I1*-anorthite (Fig. 3.3) domains separated by APB's (McLaren and Marshall, 1974) and contain large muscovite inclusions and plagioclase sub-grains. The sample is extensively altered, with patches of Na-rich feldspar replacing anorthite. Again, the Arrhenius array obtained from this sample (Fig. 3.7c) is sub-horizontal and consistent with a range in diffusive lengthscales. While plagioclase crystals from the Alpine granitoid may represent viable candidates for thermal modeling because the timing of formation and subsequent integrity of the diffusion domains can be assessed, the altered plagioclase feldspars from the Stillwater Complex and Grass Valley are poor candidates for thermochronometry, as the domain structure may have been modified during or following cooling through the Ar partial retention zone.

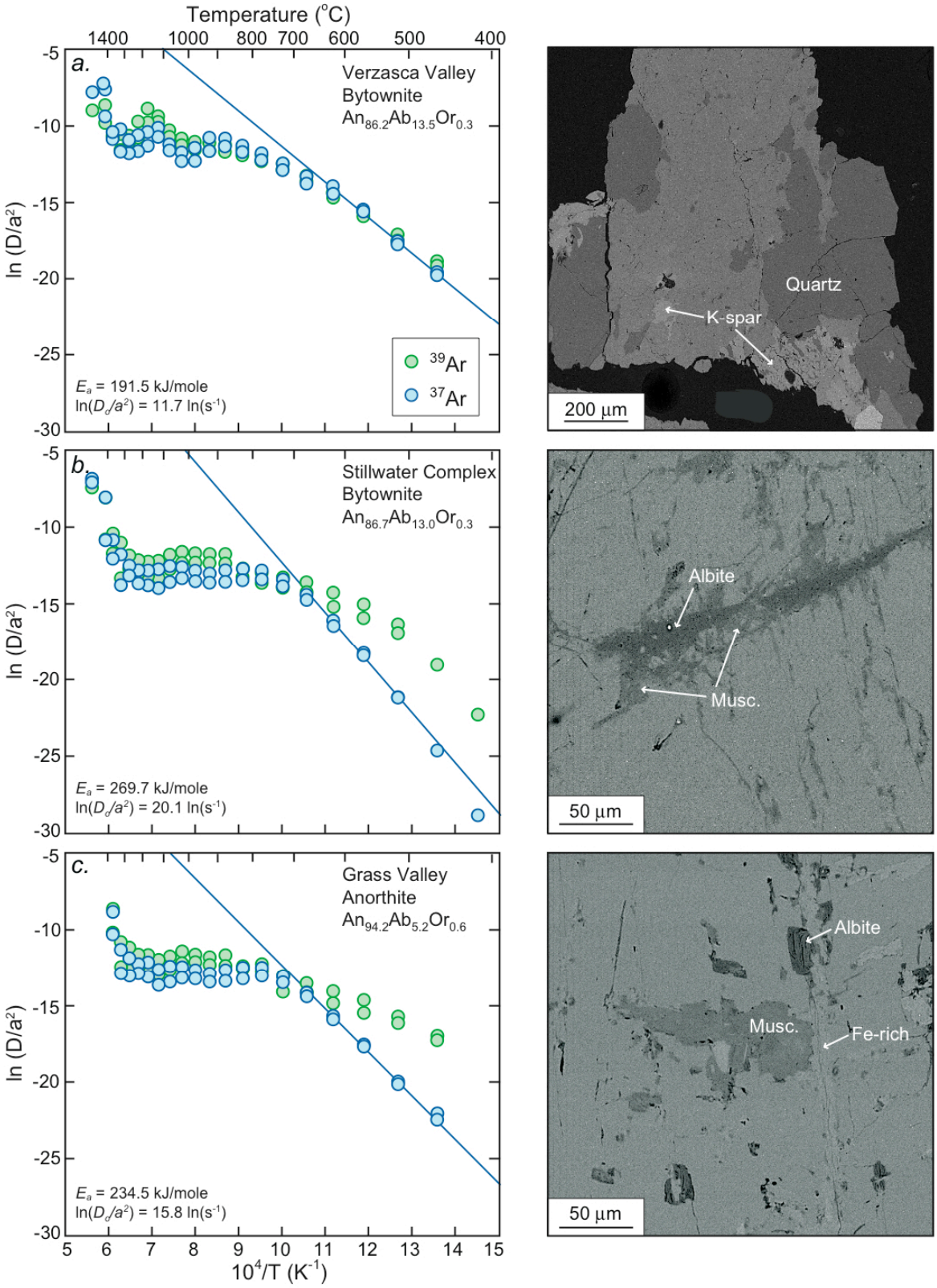
Temperature (°C)
1400
1000
800
700
600
500
400
a.
Verzasca Valley
Bytownite
An86.2Ab13.5Or0.3
39Ar
37Ar
Ea = 191.5 kJ/mole
ln(Do/a2) = 11.7 ln(s-1)
b.
Stillwater Complex
Bytownite
An86.7Ab13.0Or0.3
Ea = 269.7 kJ/mole
ln(Do/a2) = 20.1 ln(s-1)
c.
Grass Valley
Anorthite
An94.2Ab5.2Or0.6
Ea = 234.5 kJ/mole
ln(Do/a2) = 15.8 ln(s-1)
ln (D/a2)
10^4/T (K-1)
Quartz
K-spar
200 µm
Albite
Musc.
50 µm
Albite
Musc.
Fe-rich
50 µm

Figure 3.7: Arrhenius plots for prograde heating and backscattered electron microprobe images of (**a**) bytownite from a metamorphosed Alpine granitoid, (**b**) bytownite from the Stillwater Complex, and (**c**) anorthite from Grass Valley. D/a^2 values were calculated using equations for spherical geometry. Uncertainties in D/a^2 values are generally smaller than the symbols, but are not shown. The Alpine granitoid contains quartz sub-grains and alkali feldspar intergrowths. The Stillwater Complex bytownite contains veins of muscovite and porous, microcrystalline Na-rich feldspathic alteration. The Grass Valley anorthite contains large muscovite inclusions, plagioclase sub-grains, and Na-rich feldspathic alteration. The Arrhenius arrays obtained from these samples are sub-horizontal and consistent with alteration surfaces and incoherent sub-grain boundary interfaces between quartz, plagioclase, and alkali feldspar defining diffusion domains.

3.4. Summary

Feldspar crystals that are devoid of hydrothermal alteration and incoherent sub-grain intergrowths diffuse at the grain scale, except where broken by cleavage planes or fractures. Coherent lamellar interfaces typical of *e*-plagioclase intergrowths and strain-controlled perthite and anti-perthite do not define domain boundaries, but rather represent complex interfaces within composite domains. Minor inclusions within otherwise coherent crystals appear not to affect the domain structure, even when present in fairly large quantities. There is certainly some upper size limit beyond which feldspar crystals are invariably fractured or cleaved. In our experience, grains larger than ~1 mm usually yield non-linear Arrhenius arrays typical of material containing multiple diffusive length-scales. Routine examination of samples using an electron microprobe is generally sufficient to assess the nature of the diffusion domain and determine the suitability of a given mineral for thermochronometry.

Chapter 4.

Is diffusion isotropic?

4.1. Diffusion experiments on oriented cleavage flakes

To determine whether diffusion is isotropic in feldspars, we conducted detailed diffusion experiments on cleavage-bounded sheet-like flakes with high aspect ratios (>10:5:1). The lattice orientations of these crystal fragments were determined by electron backscatter diffraction (EBSD) with a Zeiss EVO scanning electron microscope (SEM) using TSL-OIM software. We isolated {001} and {010} cleavage flakes from five coherent, unaltered feldspars that, as shown previously (see Chapter 3) and below, diffuse at the grain scale: Benson Mines orthoclase (described above), Madagascar cryptoperthite (described above), a Ca-rich anorthoclase from Easy Chair Crater (ECC) in Lunar Craters Volcanic Field, Nevada, USA (Righter et al., 1993), a labradorite from the 1963 eruption of Surtsey volcano, Iceland (Wenk, 1966), and a bytownite from a lava flow near Plush, Oregon, USA (Stewart et al., 1966; Wenk et al., 1980). ECC anorthoclase crystals occur as centimeter-sized mega-xenocrysts entrained in an alkali basalt matrix (Righter et al., 1993) and are compositionally homogeneous at the micron-scale ($An_{10.8}Ab_{71.8}Or_{17.4}$). We have no detailed information regarding the microtexture or degree of Al-Si ordering in ECC anorthoclase. Surtsey labradorite crystals occur as large, glass-coated phenocrysts from a phreatic alkali-olivine basalt eruption, are compositionally homogeneous at the micron-scale ($An_{59.5}Ab_{39.6}Or_{0.9}$), and retain Al-Si order, as constrained by the presence of e-reflections in x-ray diffraction patterns typical of the *e*- and *I1*-plagioclase structures (Wenk, 1978; Wenk et al., 1980; Wenk and Nakajima, 1980). Plush bytownite crystals occur as large (cm-sized) phenocrysts in a massive basalt, are compositionally homogeneous at the micron-scale ($An_{63.9}Ab_{35.4}Or_{0.7}$), and contain regularly space, sub-micron *e*-plagioclase and anorthite intergrowths (Wenk et al., 1980; Wenk and Nakajima, 1980) consistent with slow-cooling beneath the Huttenlocher solvus (Fig. 3.3).

In addition to cleavage flakes that isolate diffusion normal to the {001} and {010} crystal faces (approximately equivalent to the *b* and *c* axes), experiments were conducted on equant grains, which include diffusion normal to the {100} crystal face (approximately equivalent to the *a* axis). For the cleavage flakes, the relevant diffusion dimension for infinite sheet geometry is half of the total thicknesses normal to the {001} and {010} crystal faces, which we measured using a binocular microscope (Fig. 3.1; Table 4.1). For the bulk crystals, grain volumes were calculated based on the total yield of ^{37}Ar or ^{39}Ar (for plagioclase and K-feldspar, respectively) and grain geometries were assumed to be spherical.

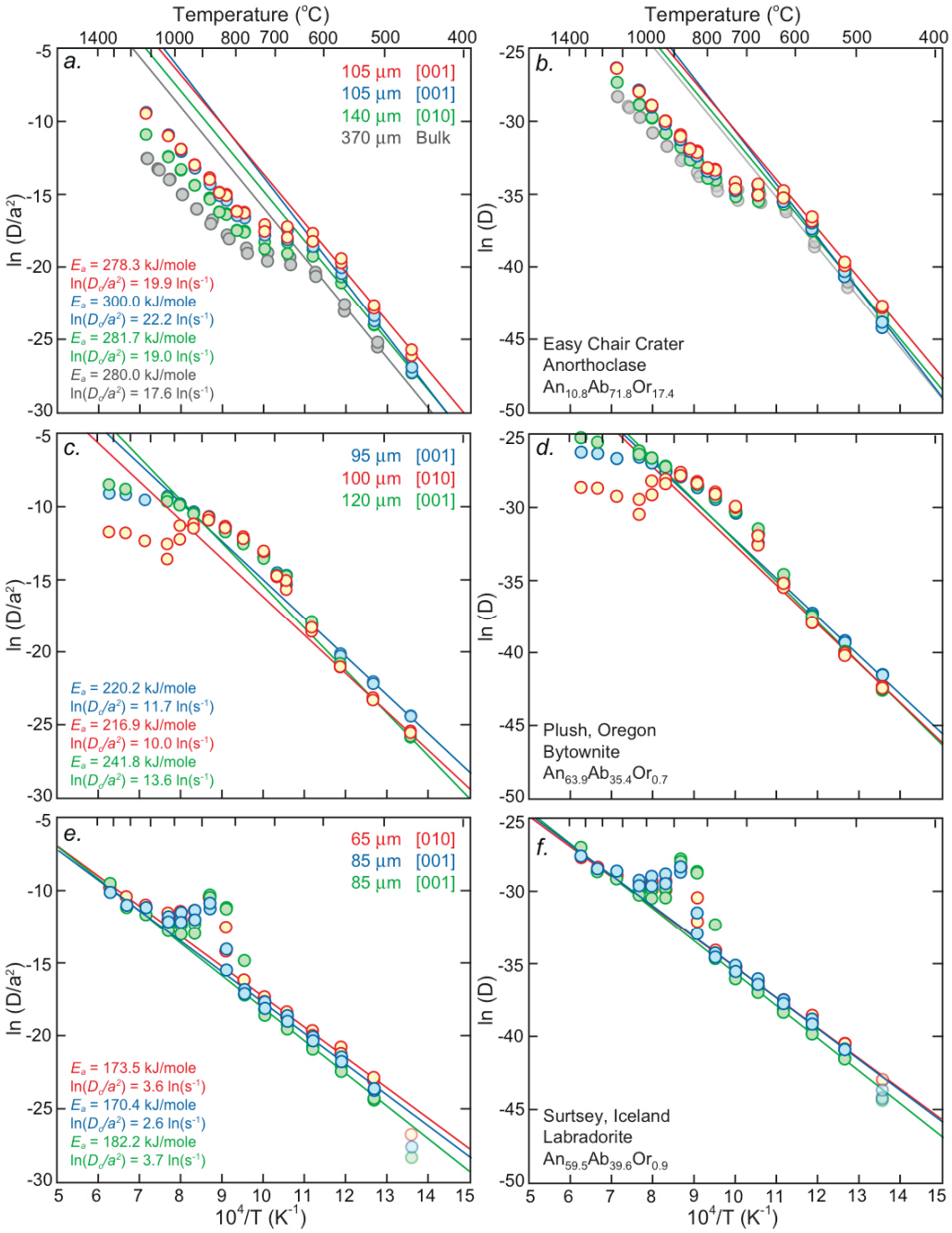

Figure 4.1: Arrhenius plots for prograde heating of (**a**,**b**) Easy Chair Crater anorthoclase (^{39}Ar), (**c**,**d**) Plush bytownite (^{37}Ar), and (**e,f**) Surtsey labradorite (^{37}Ar) crystals, calculated using equations for infinite sheet geometry for cleavage flakes and spherical geometry for equant (bulk) grains. Uncertainties in D/a^2 values are generally smaller than the symbols, but are not shown. Cleavage flake thickness and equant grain radii are listed in (**a**), (**c**), and (**e**). Data shown in (**b**), (**d**), and (**f**) were calculated by multiplying the D/a^2 values shown in (**a**), (**c**), and (**e**) by half the thickness of the cleavage flake or the equant grain radius. Anisotropy is not resolvable between {001} and {010} cleavage flakes at low-T (<800 °C). Apparent discrepancies between equant grain and cleavage flake D values can be explained by our use of spherical geometry to model tetragonal prisms (see text for discussion; Huber et al., 2011).

Anisotropy is not resolvable in the [100], [010], and [001] crystallographic directions at temperatures below ~900 °C (Figs. 3.2 and 4.1). Regardless of size and orientation, each grain yields *D* values that agree to within approximately 0.5 natural log units or better (Table 4.1); these minor differences can be explained by subtle variations in grain geometry (Huber et al., 2011) and thus limit the precision of the approach. Because Ar diffusion in feldspars appears to be isotropic, the appropriate geometry for thermal modeling is one that most closely resembles the physical grain dimensions, or the shape of sub-grain domains if applicable.

Table 4.1: Summary of cleavage flake diffusion parameters

Sample Phase	Thickness (μm)	Orientation	$E_a \pm 1\sigma$ (kJ/mole)	$\ln(D_o/a^2) \pm 1\sigma$ ($\ln(s^{-1})$)	$\ln(D_o) \pm 1\sigma$ ($\ln(m^2s^{-1})$)
Easy Chair Crater	105	[001]	278.3 ± 19.5	19.9 ± 2.8	0.2 ± 2.8
Anorthoclase	140	[010]	281.7 ± 20.0	19.0 ± 2.9	-0.1 ± 2.9
	105	[001]	300.0 ± 21.2	22.2 ± 3.1	2.5 ± 3.1
			286.0 ± 11.5		**0.8 ± 1.7**
Surtsey, Iceland	85	[001]	182.2 ± 7.1	3.7 ± 0.9	-16.4 ± 0.9
Labradorite	85	[001]	170.4 ± 5.8	2.6 ± 0.8	-17.5 ± 0.8
	65	[010]	173.5 ± 5.8	3.6 ± 0.8	-17.1 ± 0.8
			174.5 ± 3.6		**-17.1 ± 0.5**
Plush, Oregon	95	[001]	220.2 ± 17.9	11.7 ± 2.6	-8.2 ± 2.6
Labradorite	120	[001]	241.8 ± 26.6	13.6 ± 4.0	-5.8 ± 4.0
	100	[010]	216.9 ± 24.1	10.0 ± 3.6	-9.8 ± 3.6
			224.0 ± 12.5		**-8.1 ± 1.9**
Benson Mines	65	[001]	223.5 ± 3.3	11.1 ± 0.4	-9.6 ± 0.4
Orthoclase	110	[001]	216.0 ± 3.4	9.5 ± 0.4	-10.1 ± 0.4
	165	[010]	213.5 ± 3.3	8.4 ± 0.4	-10.4 ± 0.4
			217.7 ± 1.9		**-10.0 ± 0.2**
Madagascar	145	[001]	270.0 ± 7.9	17.9 ± 1.0	-1.2 ± 1.0
Cyptoperthite	175	[001]	264.1 ± 7.5	16.6 ± 1.0	-2.1 ± 1.0
	100	[001]	277.5 ± 9.1	20.1 ± 1.2	0.3 ± 1.2
	100	[001]	275.0 ± 6.2	19.2 ± 0.8	-0.6 ± 0.8
	115	[010]	278.2 ± 7.9	19.1 ± 1.0	-0.4 ± 1.0
			272.8 ± 3.4		**-0.8 ± 0.4**

Easy Chair Crater, Benson Mines, and Madagascar results based on ^{39}Ar.
Plush and Surtsey results based on ^{37}Ar.

Above ~900 °C, anisotropy is resolvable in Benson Mines orthoclase, Madagascar cryptoperthite, Surtsey labradorite, and Plush bytownite (Figs. 3.2 and 4.1). In each instance, diffusion in the [001] direction is faster than in the [010] and [100] directions, although the magnitude of anisotropy is variable. We hypothesize that anisotropic diffusion develops at high-T due to anisotropic changes in thermal expansion. In particular, a slowing or cessation of *c*-axis thermal expansion at high-T (e.g., Brown et al., 1984), with continued expansion along the *a*- and *b*-axes, would result in slower diffusion normal to the *c*-*b* and *c*-*a* planes (approximately equivalent to [100] and [010]) than the *a*-*b* plane (approximately equivalent to [001]). A systematic review of the thermal expansion behavior of feldspars and a detailed discussion of the proposed relationship between thermal expansion and Ar diffusivity is given in Chapter 5.

Chapter 5.

Non-linear Arrhenius arrays

5.1. Introduction

In Chapters 3 and 4 we showed that physical crystal dimensions define the diffusion domain of unaltered feldspars and that diffusion is isotropic to within our resolution (approximately a factor of 2). We further showed that Arrhenius arrays obtained from single-domain grains are nonetheless non-linear, exhibiting curvature or other departures from linearity at high temperatures (Figs. 3.2, 3.5, and 4.1). Such non-linearity, when not attributable to multiple diffusion domains, indicates that (1) the relative importance of different diffusion mechanisms (i.e., interstitial, cation exchange, vacancy migration, etc.) varies discontinuously with temperature, and/or (2) the diffusive medium (i.e., the structure of the feldspar lattice) varies discontinuously with temperature. This observation has significant implications for the application of MDD theory to feldspar thermochronometry. If deviations from linearity arise in single-domain feldspars due to structural or mechanistic changes, then similar behavior presumably occurs in multiple-domain feldspars. Thus while myriad feldspars undeniably contain sub-grain domains (e.g., Figs. 3.6 and 3.7), it may not be possible to infer meaningful domain distribution parameters from Arrhenius plots. In this section we review the evidence that curvature manifest on Arrhenius plots obtained from unaltered feldspars is unrelated to a range in diffusive lengthscales. We then speculate on the crystallochemical causes of such behavior and discuss the resulting implications for thermochronometry.

5.2. Evidence that Arrhenius non-linearity reflects structural or mechanistic changes

Arrhenius arrays obtained from crystal fragments degassed using the same heating schedule yield qualitatively identical Arrhenius arrays that are displaced vertically according to grain size variations (Figs. 3.2 and 4.1). For example, ECC anorthoclase (Fig. 4.1) yields linear Arrhenius arrays between 400 and 600 °C that give way to downward curvature between 650 and 800 °C, and ultimately re-establish linear Arrhenius relationships between 800 °C and the ~1100 °C melting temperature. In each of four aliquots, the offset between the low-T and high-T linear Arrhenius arrays is approximately 2 natural log units. Smaller grains yield higher $\ln(D_o/a^2)$ values and vice versa. If we assume for the moment that curvature observed between 650 and 800 °C reflects the progressive exhaustion of sub-grain diffusion domains of increasing size, then the consistent ~2 natural log unit offset between low-T and high-T arrays requires a consistent ~2.7X variation in sub-grain domain size. The vertical displacements between arrays [i.e., differences in $\ln(D_o/a^2)$] require that smaller grains have smaller sub-

grain domains and vice versa. Clearly this is illogical, as individual fragments of a homogeneous megacryst *a priori* differ only in size. Not surprisingly, all aliquots yield a coincident value of D_o when D_o/a^2 is multiplied by the square of the grain radius (Fig. 4.1). Thus the ~2 natural log unit displacement of the Arrhenius array must reflect an intrinsic change in the diffusive medium or diffusion mechanism(s). The same argument can be applied to each of the samples shown in Figures 3.2, 3.5, and 4.1.

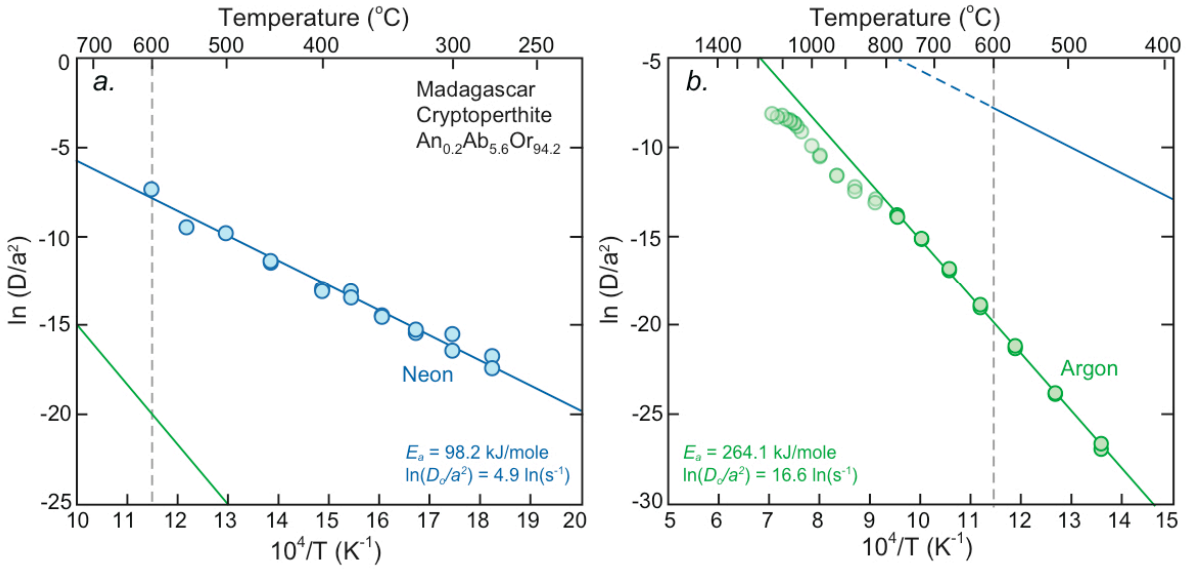

Figure 5.1: Arrhenius plots for (**a**) neon and (**b**) argon diffusion in Madagascar cryptoperthite crystals, calculated using equations for infinite sheet (Ar) and spherical (Ne) geometries. Uncertainties in D/a^2 values are generally smaller than the symbols, but are not shown. Linear regressions fit the Ar and Ne Arrhenius arrays are shown in both plots in green and blue, respectively. The temperature at which Ne is exhausted (600 °C) is denoted with a vertical, dashed gray line. The Arrhenius array for Ar diffusion exhibits curvature at ~800 °C, whereas Ne yields a linear Arrhenius array, which indicates that crystallochemical changes occurring at high-T may contribute to Arrhenius non-linearity. Neon diffusion data are from Gourbet et al. (2012).

The results of Ne and Ar diffusion experiments in Madagascar cryptoperthite further illustrate the point (Fig. 5.1). ^{22}Ne was synthetically produced by the reaction ^{23}Na(n,np)^{22}Ne during neutron irradiation (Cassata, 2011). The Arrhenius array for Ar diffusion exhibits pronounced downward curvature at ~800 °C (Fig. 5.1). Due to the significantly higher diffusivity of Ne in this alkali feldspar (Gourbet et al., 2012), it was possible to completely degas ^{22}Ne at temperatures below which we observe non-linearity on the Ar Arrhenius plot, and a single, linear Arrhenius array was obtained. Because K and Na, and therefore ^{39}Ar and ^{22}Ne, are uniformly distributed in this sample, Ar and Ne *a priori* share the same domain distribution[2]. The linearity of the Ne Arrhenius arrays confirms that crystal fragments of this feldspar

[2] Subtle variations in the relative concentrations of ^{39}Ar and ^{22}Ne may exist at grain margins due to differences in recoil distance, but such localized, sub-micron variations are volumetrically insignificant.

represent coherent, single diffusion domains (discussed above in Chapter 3). The curvature observed at high-T on the Ar Arrhenius plot therefore unambiguously reflects a crystallochemical change.

While almost all feldspars that we analyzed yielded Arrhenius arrays that curve downward at some temperature above 600 °C, plagioclase crystals with compositions between ~An_{40} and An_{100} having the *I1*-, *P1*-, *T*-, or *e*-plagioclase structures (Fig. 3.3) are unique in that Arrhenius arrays invariably curve upward prior to higher temperature downward curvature (i.e., the diffusivity increases significantly faster than expected from upward extrapolation of a linear, lower-T Arrhenius relationship; Fig. 5.2). Such upward curvature cannot be explained by range in diffusive lengthscales, unless the original diffusive lengthscale is reduced during the course of incremental heating by fracturing or cleaving. While there is no reason that Ca-rich plagioclase feldspars should cleave or fracture more readily than other feldspars, we obtained SEM images of a selection of samples subjected to a typical incremental heating schedule to confirm that these crystals remain intact. In no case was cleaving or fracturing observed. Furthermore, retrograde heating subsequent to upward curvature yields ln(D/a^2) values that

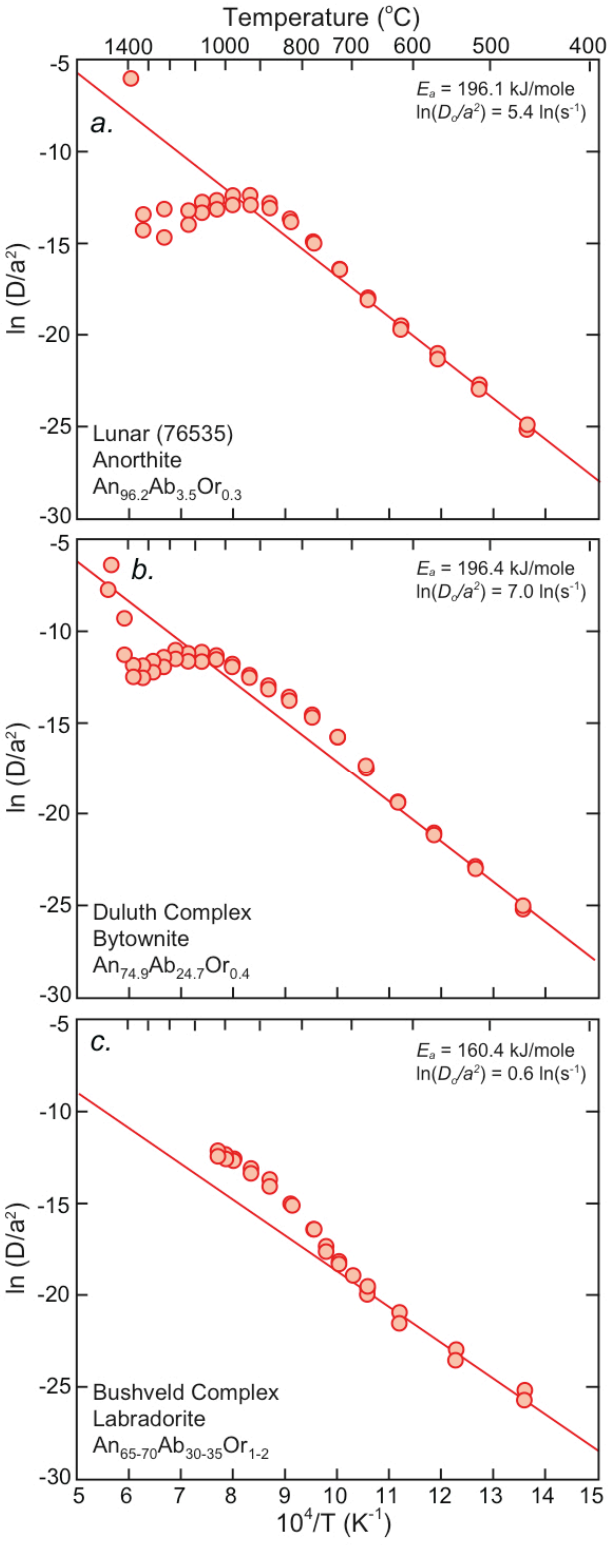

Figure 5.2: Arrhenius plots for prograde heating of (**a**) lunar (from troctolite 76535) anorthite (^{37}Ar), (**b**) Duluth Complex bytownite (^{37}Ar), and (**c**) Bushveld Complex labradorite (^{37}Ar) crystals, calculated using equations for spherical geometry. Uncertainties in D/a^2 values are generally smaller than the symbols, but are not shown. All feldspars with compositions between ~An_{40} and An_{100} having the *I1*-, *P1*-, *T*-, or *e*-plagioclase structures (such as these samples), yield Arrhenius arrays that curve upward between 600 and 800 °C, and then downward at higher-T.

approach those observed in prior prograde heating cycles at lower-T (i.e., upward curvature is reversible; discussed below). Although upward, reversible curvature is consistent with temperature-dependent anisotropy (i.e., different E_a's for diffusion along different crystallographic axes; Huber et al., 2011), such an explanation can dismissed on the grounds that both equant grain fragments and {001} and {010} cleavage flakes yield indistinguishable Arrhenius arrays (Figs. 3.5 and 4.1). Therefore, these observations can only be explained by a change in the nature of diffusion, either resulting from structural modifications to the feldspar lattice or a significant variation in the mechanisms of diffusion.

5.3. Molecular dynamics considerations

In this section we couple observations of Ar diffusion in feldspars with molecular dynamics (MD) simulations of solid-gas interactions and experimental data on the physical properties of feldspars over a range of temperatures to better understand causes of non-linear Arrhenius arrays. At this point it is worth reviewing the atomic motions that facilitate Ar diffusion through the feldspar lattice, which include the direct exchange, vacancy, direct interstitial, and interstitialcy mechanisms. During direct exchange, an Ar atom occupying a cation or anion vacancy exchanges position with a neighboring cation or anion. Similarly, during diffusion by the interstitialcy mechanism, an Ar atom occupying an interstitial site displaces a cation or anion to a neighboring interstitial site. Thus the direct exchange and interstitialcy mechanisms require cationic and/or anionic movements (i.e., the breaking of bonds). The observation that noble gas diffusion is orders of magnitude faster than cation and anion diffusion, particularly at low temperatures (see reviews by Baxter, 2010; Cherniak, 2010), seems to require that the direct interstitial mechanism, wherein an Ar atom moves from one interstitial site to the next without net motion of the cations or anions, is the dominant mode of transport within the lattice (e.g., Voltaggio, 1985). Diffusion through vacancies, as well as along extended linear and planar defects (e.g., fission tracks in zircon), is presumably also important, although these features are volumetrically minor.

Molecular dynamics simulations (e.g., Watanabe et al., 1995; Reich et al., 2007; Du et al., 2008; Saaduone et al., 2009) provide insights into the potential energy barriers that must be overcome for diffusion to proceed by the direct interstitial mechanism (e.g., Born-Mayer or Lennard-Jones potentials). The energy required to traverse a given interstitial lattice configuration depends on quantum mechanical interactions (e.g., electron shell repulsions and dispersion forces) between noble gas atoms and relevant cations and/or anions (e.g., Dove, 2001). Thus atomic properties of the atoms (e.g., van der Waals radii, electron densities, charges, etc.), as well as their crystallographic arrangement (i.e., bond lengths and angles), determine the potential energy barrier to diffusion. At a given temperature, a bulk diffusion coefficient typically reflects the migration of hundreds of billions of atoms through a variety of differing interstitial lattice configurations arranged in a regular and repeating manner defined by the crystal structure. Different interstitial environments have different potential energy barriers to be overcome and impart different vibrational frequencies upon Ar atoms (Reich et al., 2007; Saaduone et al., 2009). Interstitial configurations with low potential energy barriers are most frequently traversed, provided that their vibrational frequencies are

similar, and the interconnectedness and availability of such interstitial lattice configurations within the crystal structure determines the pathway of most efficient escape. The greatest potential energy barrier that is traversed along a given crystallographic axis should, in theory, approximate the E_a for diffusion in that direction if the lattice is static (i.e., bond lengths and angles do not undergo changes) when subject to heating or cooling. The apparent E_a for bulk crystal diffusion is, *a priori*, intermediate between the highest and lowest values of the individual crystallographic directions, and need not be continuous (i.e., a crystal with directionally-dependant potential energy barriers may not yield a linear Arrhenius array, but the slope will always be intermediate between the E_a for diffusion along the individual crystallographic directions). In Figure 5.3 we show Arrhenius arrays that would result from degassing two hypothetical cubic grains that have directionally-dependent potential energy barriers. Note that the apparent E_a*'s* obtained are not equivalent to any of three individual crystallographic axes. When the contrast in potential energy barriers is modest (Fig. 5.3a), linear Arrhenius arrays are obtained. When the contrast is significant (Fig. 5.3b), the apparent

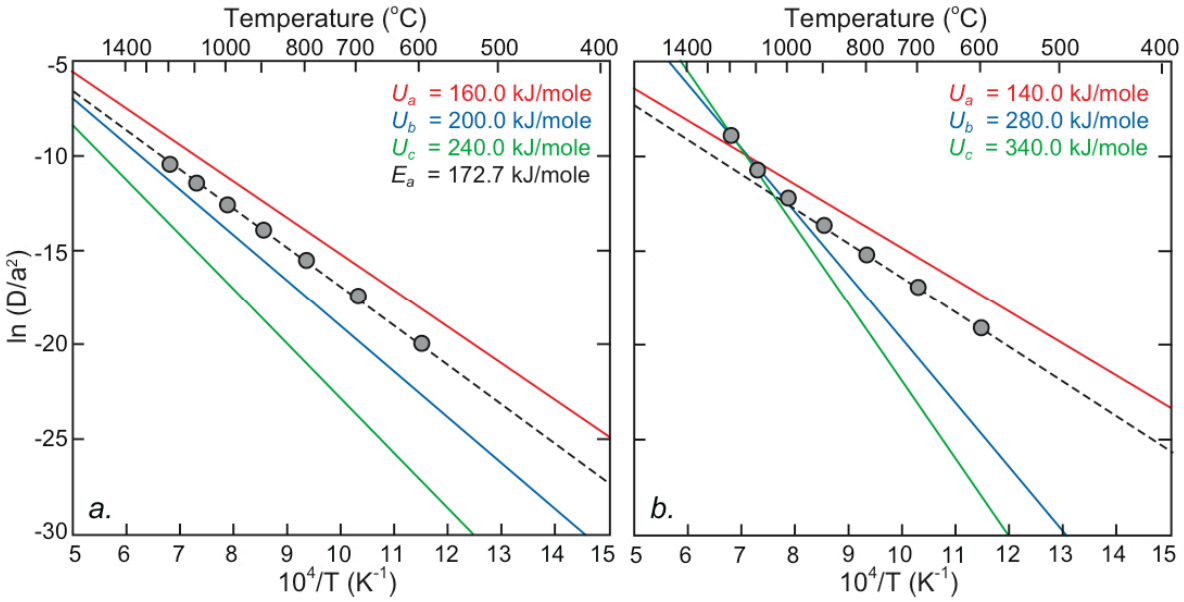

Figure 5.3: Modeled Arrhenius arrays (gray circles) that would result from degassing cubic grains with directionally-dependant diffusive anisotropy. The red, blue, and green Arrhenius relationships describe diffusion in the *a*, *b*, and *c* crystallographic directions, respectively, and the corresponding potential energy barriers to diffusion (*U*) are listed in upper, right corner of each plot. (**a**) Crystals with modestly contrasting potential energy barriers yield linear Arrhenius arrays. The apparent E_a for bulk crystal diffusion (listed in the upper, right corner) is intermediate between the highest and lowest values of the individual crystallographic directions. (**b**) Crystals with strongly contrasting potential energy barriers yield curvilinear Arrhenius arrays. The apparent E_a approximates the pathway of most efficient escape at low-T, and increases at higher-T as contributions from alternative pathways become significant.

E_a approximates the pathway of most efficient escape at low-T, but contributions from alternative pathways may become significant at high-T and Arrhenius arrays may exhibit upward curvature. If the lattice is static over the range of temperatures employed in a

diffusion experiment, then downward curvature on an Arrhenius plot is never predicted by theory, as deviations from linearity only arise due to an increasing proportion of diffusion proceeding along a previously less significant crystallographic direction.

Feldspars, and most minerals for that matter, are not static during incremental heating experiments, and therefore more complex Arrhenius arrays are predicted by molecular dynamics considerations. Thermal expansion and concomitant flexures of the tetrahedral framework of feldspar, as well as changes in the location, coordination, and vibrational modes of cations, produce anisotropic changes in bond lengths and angles upon heating. Repulsive forces between noble gases and lattice atoms (i.e., the potential energy barriers to diffusion) are exceedingly sensitive to subtle changes in bond lengths and angles. For example, the Lennard-Jones potential, which describes the distance-dependence of gas-gas and gas-solid repulsive forces (e.g., Du et al., 2008), is given by

$$U\left(r_{ij}\right) = 4\varepsilon_{ij}\left[\left(\frac{\sigma_{ij}}{r_{ij}}\right)^{12} - \left(\frac{\sigma_{ij}}{r_{ij}}\right)^{6}\right] \qquad \text{Eq. (1)}$$

where i and j are two interacting atoms, r_{ij} is the distance between them, σ_{ij} is the Lennard-Jones size parameter based on van der Waals radii, and ε_{ij} is the Lennard-Jones energy parameter determined empirically or through molecular dynamics simulations (see Du et al. (2008) for various noble gas values). Because of the exponential distance-dependence, small (2-4%) changes in bond lengths that occur due to thermal expansion of feldspars during incremental heating experiments (e.g., Brown et al., 1984) can result in significant (>50%) reductions in potential energy barriers to diffusion (Fig. 5.4). An Arrhenius array obtained

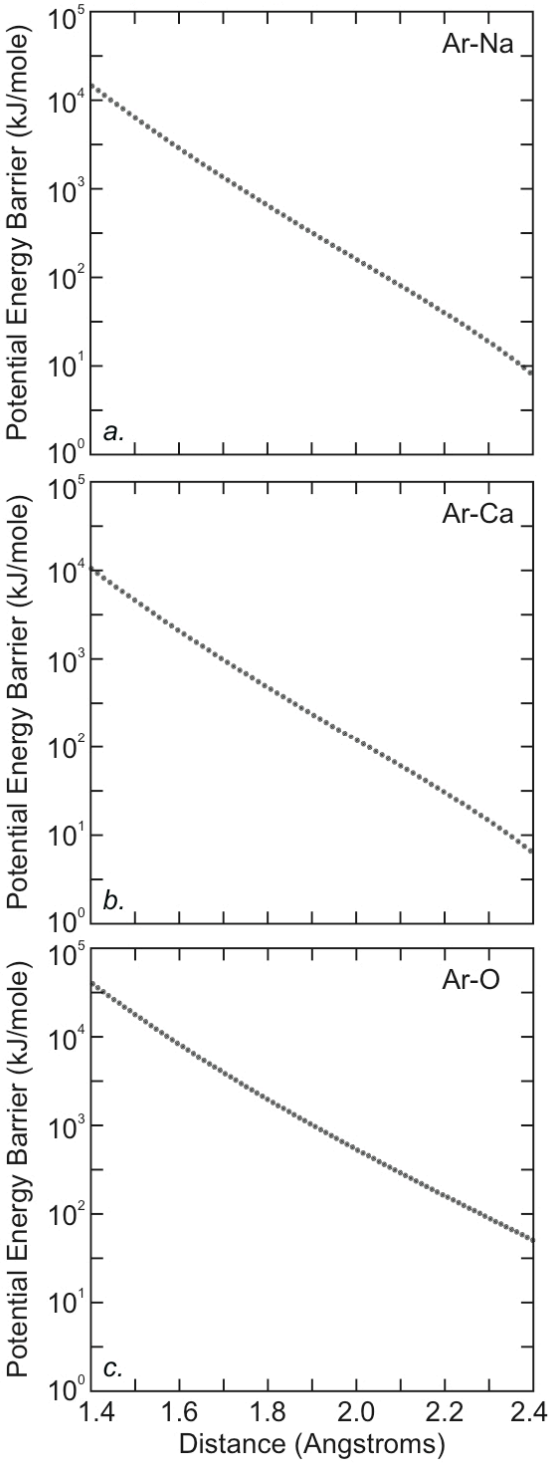

Figure 5.4: Illustration of the distance-dependence of the (**a**) Ar-Na, (**b**) Ar-Ca, and (**c**) Ar-O Lennard-Jones potentials, calculated from Eq. (1) using the Lennard-Jones parameters listed in Table 5.1.

by incrementally degassing a feldspar crystal thus reflects diffusion through a dynamic crystal with temperature-dependent potential energy barriers and vibrational frequencies. For this reason, molecular dynamics simulations of noble gas diffusion that do not incorporate temperature-dependent mineral structures (e.g., Reich et al., 2007; Saaduone et al., 2009) are not expected to yield apparent diffusion parameters consistent with incremental degassing experiments.

Consider a hypothetical primitive isometric crystal with oxygen (O) atoms at its lattice nodes and unit cell dimensions $a = b = c = 3.00$ Å at 0 °C (Fig. 5.5a; Table 5.1). Assume that it undergoes linear, isotropic thermal expansion of 4% between 0 and 1200 °C (approximately equivalent in magnitude to albite thermal expansion; Brown et al., 1984). The potential energy barrier to Ar diffusion at a given temperature can be calculated by solving Eq. (1) for the minimum in Ar-O repulsive interactions using the Lennard-Jones parameters listed in Table 5.1. The associated vibrational frequencies can be approximated by solving an expression (Glicksman, 2000) adapted from transition state theory (Vineyard, 1957), given by

$$\upsilon_o = \frac{1}{\sqrt{2}}\left(\frac{U}{md^2}\right)^{\frac{1}{2}}, \qquad \text{Eq. (2)}$$

where m is the atomic weight of Ar, d is the jump distance between two minima and is equal to the relevant unit cell dimension, and U is the potential energy barrier to diffusion. These vibrational frequencies can be translated into tracer diffusion frequency factors using Einstein's equation (see Reich et al., 2007) according to the following:

$$\nu_o = \frac{1}{2}d^2\upsilon_o. \qquad \text{Eq. (3)}$$

Figure 5.5b depicts the Arrhenius array that would result from incrementally heating such a crystal. By inspection it is clear that the apparent E_a (268.9 kJ/mole) overestimates the 600 °C potential energy barrier to diffusion (203.5 kJ/mole) by 32%, even as the potential energy barrier is reduced with increasing temperature due to thermal expansion. If thermal expansion is negative (Fig. 5.5c), the apparent E_a (198.1 kJ/mole) underestimates the 600 °C potential energy barrier (339.0 kJ/mol) by 42%. In that regard, it would be interesting to determine He diffusion kinetics in proton-irradiated cubic zirconium tungstate, a mineral that undergoes remarkable isotropic negative thermal expansion over laboratory temperatures typical of He diffusion experiments (e.g., 100-500 °C). If thermal expansion proceeds non-linearly as a function of temperature, then upward and downward curvature may be observed on Arrhenius plots, coincident with the onset or cessation of enhanced thermal expansion, respectively (Fig. 5.5d,e). If thermal expansion proceeds linearly with temperature but anisotropically (e.g., more rapidly along the c axis), then downward curvature may be observed on Arrhenius plots (Fig. 5.5f). When viewed in this context, it is not surprising that bulk diffusion coefficients describing noble gas migration through complex triclinic or monoclinic crystals that undergo structural changes when heated do not define strictly linear Arrhenius arrays. In feldspars, thermal expansion rarely proceeds linearly or isotropically as a function of temperature.

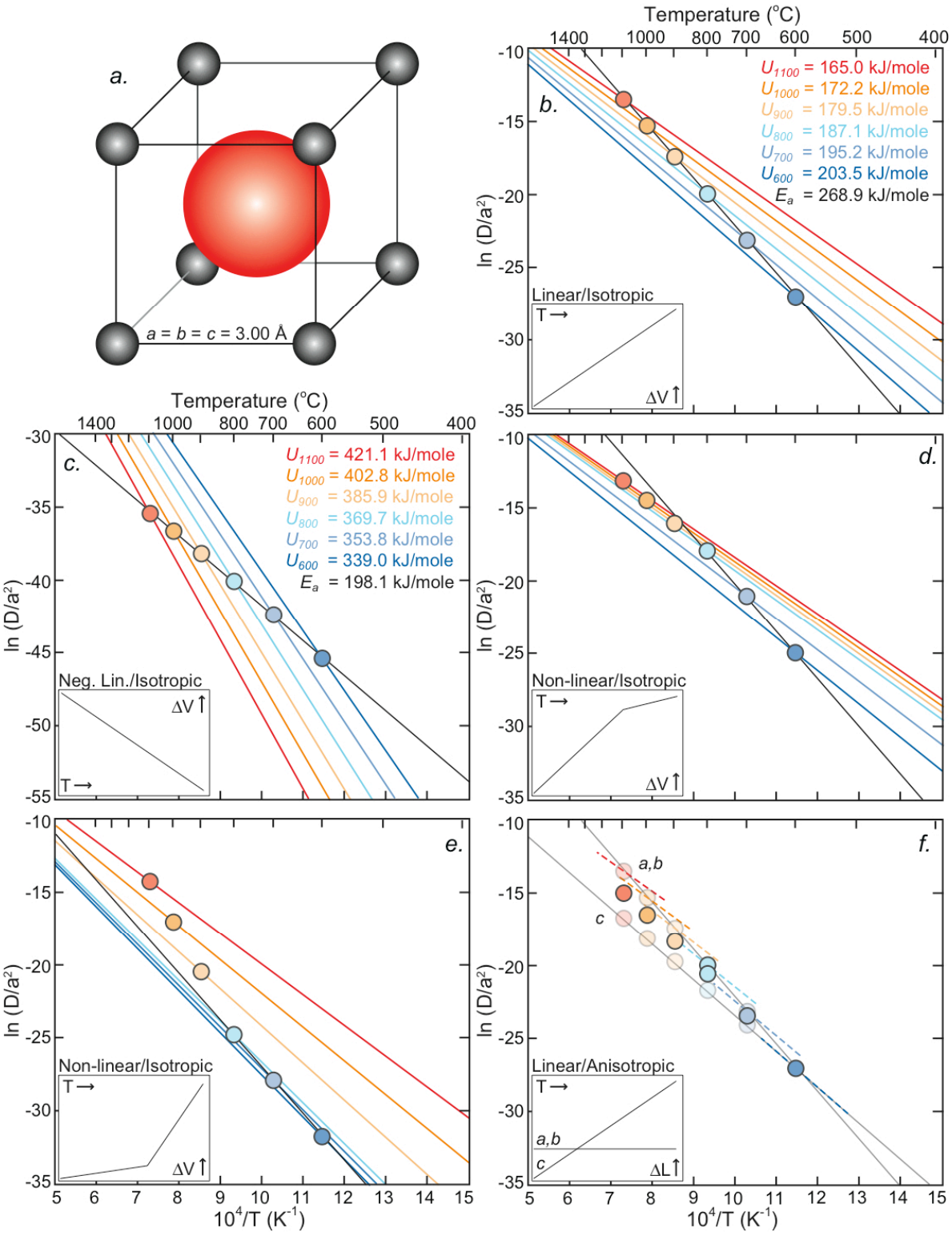
a.
a = b = c = 3.00 Å
Temperature (°C)
1400 1000 800 700 600 500 400
b.
U_{1100} = 165.0 kJ/mole
U_{1000} = 172.2 kJ/mole
U_{900} = 179.5 kJ/mole
U_{800} = 187.1 kJ/mole
U_{700} = 195.2 kJ/mole
U_{600} = 203.5 kJ/mole
E_a = 268.9 kJ/mole
Linear/Isotropic
T →
ΔV ↑
ln (D/a²)
c.
U_{1100} = 421.1 kJ/mole
U_{1000} = 402.8 kJ/mole
U_{900} = 385.9 kJ/mole
U_{800} = 369.7 kJ/mole
U_{700} = 353.8 kJ/mole
U_{600} = 339.0 kJ/mole
E_a = 198.1 kJ/mole
Neg. Lin./Isotropic
d.
Non-linear/Isotropic
e.
Non-linear/Isotropic
f.
a,b
c
Linear/Anisotropic
ΔL ↑
10⁴/T (K⁻¹)

Figure 5.5: (**a**) A hypothetical primitive isometric crystal with oxygen atoms at its lattice nodes (black) and unit cell dimensions $a = b = c = 3.00$ Å at 0 °C. An argon atom (red) is shown at the body center. (**b**) Modeled Arrhenius relationship (black line and colored circles) that would result from incrementally heating the isometric crystal, assuming that it undergoes linear, isotropic thermal expansion of 4% between 0 and 1200 °C (shown schematically in the inset). The potential energy barriers to Ar diffusion (U) at various temperatures, calculated by solving Eq. (1) for the minimum in Ar-O repulsive interactions, are listed in the upper, right corner. The associated vibrational frequencies used to plot the temperature-dependent Arrhenius relationships (colored lines) were calculated by solving Eqs. (2) and (3). The apparent E_a (listed in the upper, right corner) reflects the temperature-dependent changes in unit cell dimensions, and therefore potential energy barriers and vibrational frequencies. (**c**) Modeled Arrhenius relationship calculated assuming that the isometric crystal undergoes linear, isotropic thermal expansion of -4% between 0 and 1200 °C. (**d**) Modeled Arrhenius array calculated assuming that the isometric crystal undergoes non-linear, isotropic thermal expansion of 3.6% between 0 and 900 °C and 0.4% between 900 and 1200 °C. Downward curvature is observed when the rate of thermal expansion decreases at 900 °C. (**e**) Modeled Arrhenius array calculated assuming that the isometric crystal undergoes non-linear, isotropic thermal expansion of 1% between 0 and 800 °C and 3% between 800 and 1200 °C. Upward curvature is observed when the rate of thermal expansion increases at 800 °C. (**f**) Schematic Arrhenius array calculated assuming that the isometric crystal undergoes non-linear, anisotropic thermal expansion of 2% between 600 and 1200 °C along the *c*-axis and 0% between 600 and 1200 °C along the *a*- and *b*-axes. The Arrhenius relationship for diffusion along the *c*-axis is temperature-independent because the *a*-*b* plane does not undergo expansion (i.e., the interstitial lattice configurations traversed in the *c*-direction do not expand). Downward curvature is observed at high-T as diffusion along the *c*-axis becomes increasingly less significant.

With the foregoing in mind, let us turn to a detailed description of the feldspar structure, which is central to our discussion of the relationship between Ar diffusion kinetics and temperature-dependant changes in cell parameters, and therefore potential energy barriers. Oxygen atoms (O) form tetrahedra centered by aluminum and silicon atoms (T-sites), the corners of which are shared, creating four-member rings. These tetrahedral rings join together forming kinked chains, or "crankshafts" (Fig. 5.6a). Linking chains together across mirror planes creates large interstices (M-sites) that are filled by Na, K, and Ca atoms (Fig. 5.6a). Thus the feldspar structure comprises an aluminosilicate framework with alkali and alkali earth cations occupying large structural cavities (Fig. 5.6b). The symmetry of feldspars is controlled by the degree of Al and Si ordering on T-sites, composition, pressure, and temperature. All Na- and Ca-rich feldspars are triclinic (unit cell angles $\alpha \neq \beta \neq \gamma \neq 90°$) at room temperature, as the lattice is distorted about the small Ca and Na atoms (Fig. 5.6c). At high temperatures, disordered Na-rich alkali and plagioclase feldspars (e.g., anorthoclase, high albite, high oligoclase; Fig. 3.3) undergo a displacive transition to monoclinic symmetry (unit cell angles $\alpha \neq \beta = \gamma = 90°$) due to thermal vibrations of the cations and tetrahedral framework (Fig. 5.6d). Sanidine is monoclinic at all temperatures because the disordered framework is held apart by large K atoms (Fig. 5.6d). Ordered Na- and K-rich feldspars (e.g., microcline and low albite) are triclinic at all temperatures. Regardless of T-site ordering and temperature, Ca-rich plagioclase feldspars (e.g., andesine, labradorite, bytownite, anorthite, and Ca-rich

oligoclase; Fig. 3.3) are triclinic. Orthoclase is a metastable alkali feldspar with pseudo-monoclinic symmetry (monoclinic average symmetry), comprising submicroscopic triclinic domains in which Al is ordered on different T_1-sites (Parsons and Lee, 2005). Si and Al diffusion is exceedingly slow at typical laboratory temperatures and timescales (e.g., Carpenter et al., 1985), and thus changes in symmetry due to ordering are not expected to occur during step-heating. In the following sections, we discuss how structural state and changes in bond lengths (both T-O and M-O) and bond angles (O-T-O, T-O-T, M-O-T, O-M-O) that occur during step-heating experiments affect diffusion kinetics.

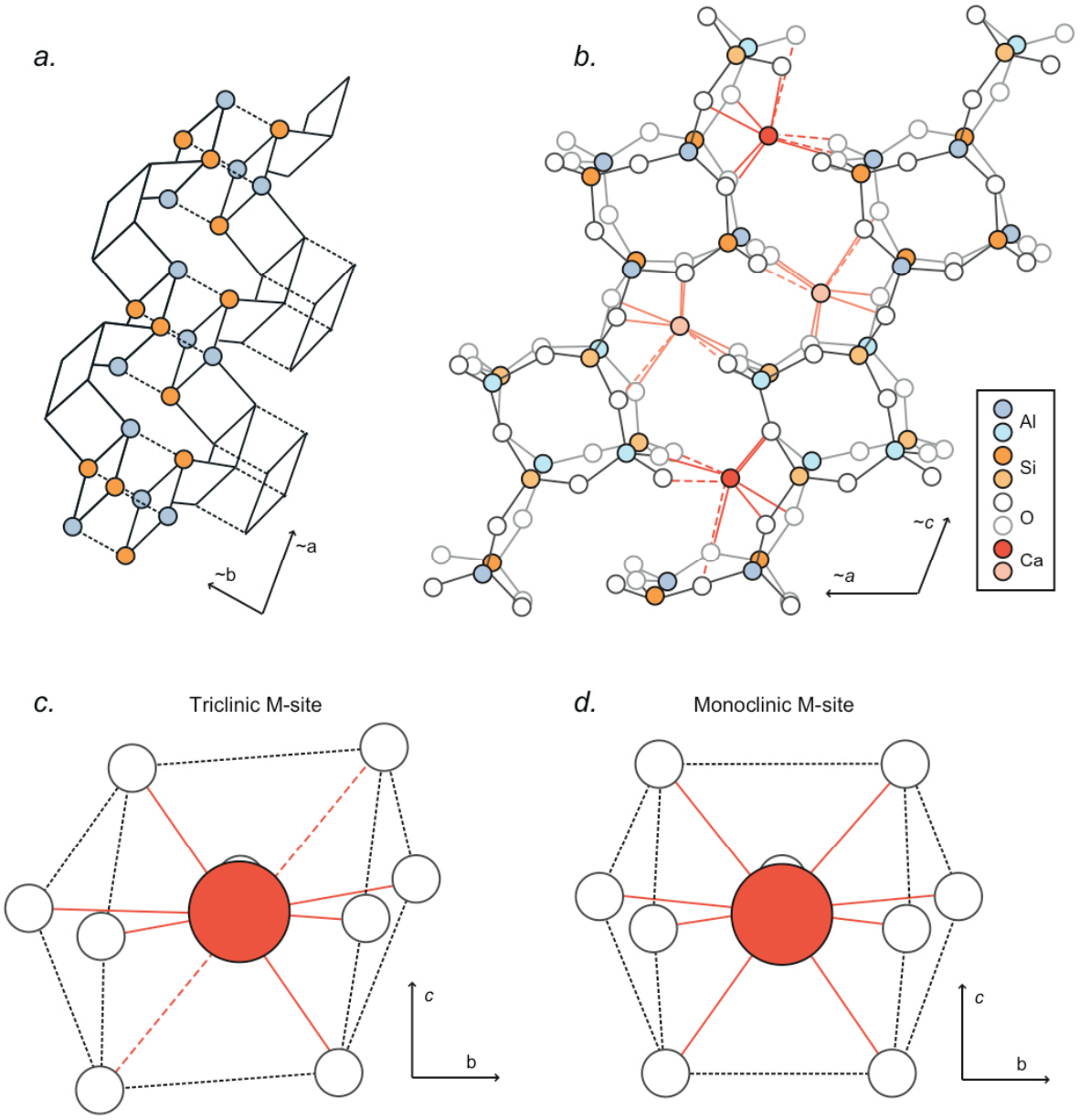

Figure 5.6: Stylized diagrams of various aspects of the feldspar structure. (**a**) Schematic illustration of the "crankshafts" formed by four-member rings of tetrahedra (represented by chains of squares drawn with solid lines) running approximately parallel to the *a*-axis. These crankshafts are links across (010) mirror planes (approximately orthogonal to the *b*-axis; dashed lines) creating large interstices that are filled by Na, K, and Ca atoms (M-sites). Modified after Megaw (1973). (**b**) Projection down [010] of anorthite showing details of the cation coordination environment and tetrahedral framework. Crankshafts of Al and Si tetrahedra running approximately parallel to the *a*-axis are denoted with different shades of blue (Al) and orange (Si). Six- and seven-fold coordinated Ca M-sites are denoted by red and salmon symbols, respectively. Solid and dashed red and salmon lines represent the primary and secondary coordination spheres, respectively. Redrafted from Megaw et al. (1962). (**c,d**) Coordination environment of Na atoms in the triclinic (seven-fold) and monoclinic (nine-fold) albite structures. Solid and dashed lines represent the primary and secondary coordination spheres, respectively. Redrafted from Winter et al. (1979).

5.4. Na-rich feldspars

Disordered albite, anorthoclase, and Na-rich oligoclase provide the most straightforward illustration of the relationship between structural state and Ar diffusion kinetics, as they undergo a displacive transition during step-heating experiments wherein cell parameters (unit cell lengths a, b, and c, and unit cell angles α, β, and γ) change significantly over a narrow temperature interval. At low-T, all Na-rich feldspars are triclinic because the aluminosilicate framework is puckered around small Na cations. The coordination about the M-site is irregular, with 5 to 7 of the nine nearest oxygen atoms having short M-O distances that define the primary coordination environment (Fig. 5.6c) and 2 to 4 having significantly longer M-O distances (Kroll et al., 1980; Harlow, 1982; Brown et al., 1984). Upon heating from room temperature, thermal expansion of Na-rich feldspars proceeds such that *a, b, c,* and the unit cell volume (V) increase approximately linearly as a function of temperature, with only minor changes to α, β, and γ (Fig. 5.7; Prewitt et al., 1976; Winter et al., 1979; McMillan et al., 1980; Brown et al., 1984). As heating proceeds toward a critical temperature (discussed below) the thermal expansion regime changes: at least one component of expansion in the *b-c* plane slows or ceases and α accelerates towards 90° (Fig. 5.7), until monoclinic symmetry is attained at the critical temperature (Winter et al., 1979; Brown et al., 1984). The change in thermal expansion regime corresponds to a shortening of longer M-O bonds (Fig. 5.6d), lengthening of shorter M-O bonds, and rotation (tilting) of the tetrahedral framework (Harlow, 1982). Thus over a narrow temperature range (~200 °C; e.g., Winter et al., 1979), thermal vibrations of the tetrahedral framework and cations cause the lattice to undergo rapid changes in unit cell parameters, bond lengths and angles, and in the coordination environment of the M-site. Above the critical temperature, thermal expansion again proceeds in a regular manner, with *a, b, c,* and V increasing linearly with temperature (Fig. 5.7; Brown et al., 1984). The temperature-dependence of thermal expansion in Na-rich feldspars can thus been divided into two regimes of regular thermal expansion that do not significantly alter the structure (associated with the triclinic and monoclinic symmetry states) separated by the triclinic-

monoclinic transition zone, wherein expansion in the *b*-*c* plane slows or ceases (Fig. 5.7).

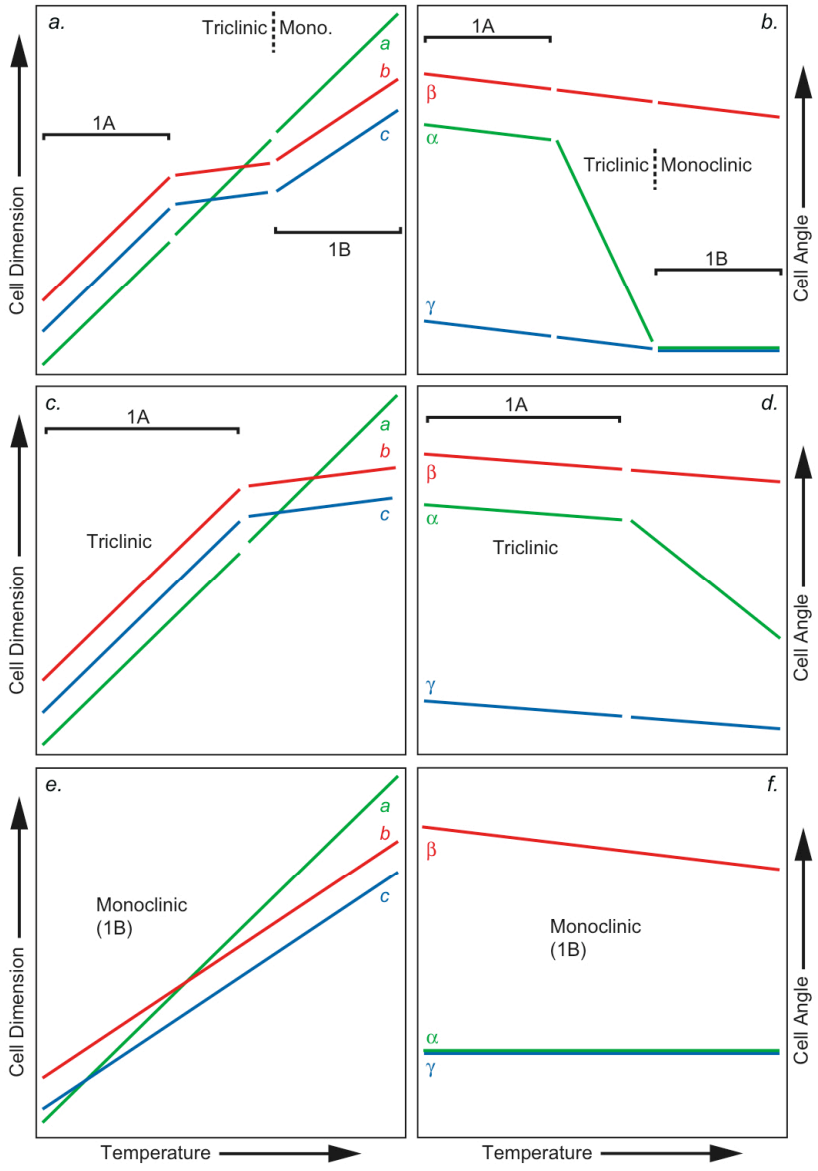

Figure 5.7: Schematic illustration of the affects of thermal expansion on unit cell dimensions and angles in (**a,b**) Na-rich feldspars that undergo a triclinic to monoclinic transition at high-T, (**c,d**) Na-rich plagioclase feldspars that do no undergo the aforementioned transition, and (**e,f**) K-rich feldspars that monoclinic at all temperatures (see text for details). Trends are based on sources given in Section 5.

Likewise, the temperature-dependence of Ar diffusivity in Na-rich feldspars that undergo a triclinic to monoclinic transition when heated can be divided into two dissimilar regimes separated by a transition zone. For example, in Figure 5.8 we show Arrhenius plots obtained from two such feldspars: anorthoclase from Easy Chair Crater (described previously in Chapter 3) and oligoclase ($An_{19.6}Ab_{74.2}Or_{6.2}$) from a ~32 ka rhyolitic ash from Mono Lake, California, USA (Cassata et al., 2010). We have no detailed information regarding the microtexture or degree of Al-Si order in Mono Lake oligoclase. Both samples yield linear Arrhenius arrays at low- and high-T separated by a curvilinear transition zone, wherein the rate at which diffusivity increases with temperature slows (i.e., the Arrhenius arrays exhibit downward curvature; Fig. 5.8). We suggest that curvature observed on Arrhenius plots reflects the change in the thermal expansion regime associated with the triclinic-monoclinic transition. When expansion in the *b*-*c* plane slows or ceases and α accelerates towards 90°, the rate at which diffusivity increases with temperature appears, as predicted by the molecular dynamics considerations described above,

to slow. We propose that linear arrays observed below and above the non-linear portions of the Arrhenius plots correspond to the linear thermal expansion regimes below and above the triclinic-monoclinic transition zone, and therefore describe diffusion in the triclinic and monoclinic forms of the feldspars, respectively. The high-temperature linear array observed on the ECC anorthoclase Arrhenius plot (Fig. 5.8b) commences at the exact temperature at which monoclinic symmetry is expected to be attained in feldspar of its composition (~750 °C; Kroll and Bambauer, 1981). The Arrhenius plot obtained from Mono Lake oligoclase exhibits curvature approximately ~150 °C lower than predicted by Kroll and Bambauer (1981), which presumably reflects its greater degree of disorder (Fig. 5.8a). The critical temperature for the monoclinic-triclinic transition can be lowered by hundreds of degrees in highly disordered feldspars (Barth, 1964; Stewart and von Limbach, 1967).

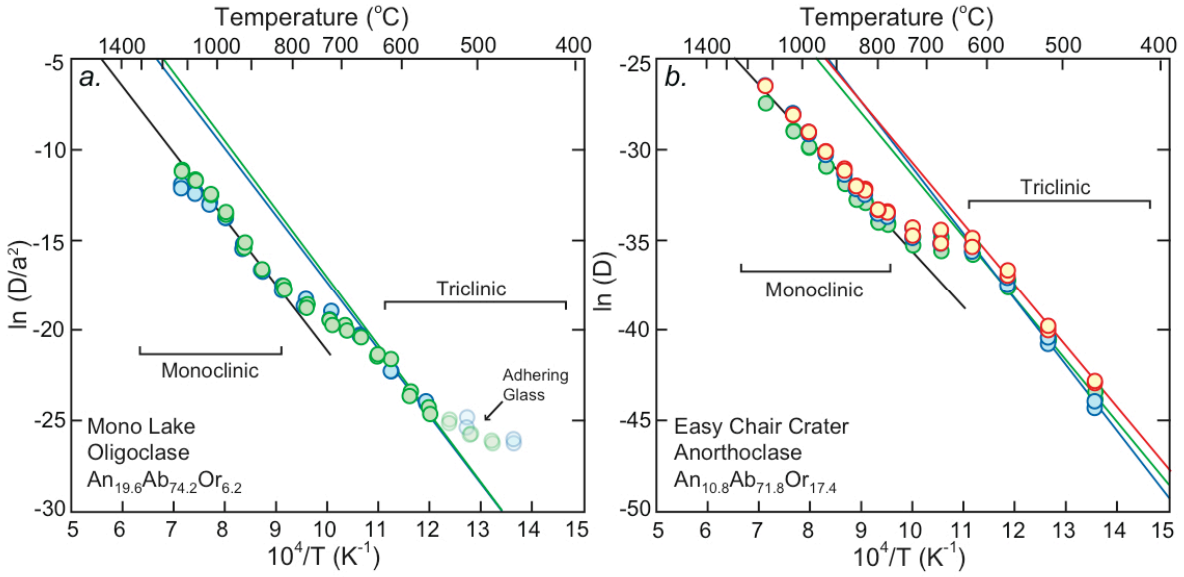

Figure 5.8: Arrhenius plots for prograde heating of (**a**) Mono Lake oligoclase (^{37}Ar) and (**b**) Easy Chair Crater anorthoclase (^{39}Ar) crystals, calculated using equations for spherical and infinite geometries, respectively. Uncertainties in D/a^2 values are generally smaller than the symbols, but are not shown. The temperature-dependence of Ar diffusivity these samples can be divided into two regimes of constant apparent E_a separated by a transition zone. The low- and high-T linear Arrhenius arrays correspond to the triclinic and monoclinic structures of the feldspars, respectively. The intermediary curvature reflects the change in cation coordination and the thermal expansion regime (Fig. 5.7) associated with the triclinic-monoclinic transition. Lighter, low-T data obtained from Mono Lake oligoclase reflect Ar derived from minor adhering glass, and can be distinguished on the basis of their Ca/K ratios.

Ordered Na-rich feldspars and more Ca-rich feldspars of the *C1* symmetry group (e.g., ordered oligoclase, andesine; Fig. 3.3) do not achieve monoclinic structure below their melting temperature, although the rate of change in cell parameters nonetheless accelerates at high temperature (>900 °C; Prewitt et al., 1976; Winter et al., 1979; Brown et al., 1984). Thus the thermal expansion of these feldspars can be divided into two parts (Fig. 5.7c,d): a low

temperature regime characterized by approximately linear changes in *a, b, c,* and *V* with increasing temperature, associated with the triclinic structure, and a transition zone characterized by significant changes in cell angles, associated with the transition toward monoclinic symmetry. In Figure 5.9 we compare Arrhenius plots obtained from four such compositionally homogeneous feldspars: ordered oligoclase ($An_{14.1}Ab_{84.1}Or_{1.8}$; Shearer et al., 2010) from the ungrouped, plutonic achondrite GRA 06128, oligoclase/andesine ($An_{29.8}Ab_{64.7}Or_{4.5}$) from the ~28 Ma Fish Canyon Tuff, a massive rhyolitic ignimbrite in southwestern Colorado, USA, andesine ($An_{41.1}Ab_{54.6}Or_{4.3}$) from a rhyodacite lava of the Paraná-Etendeka large igneous province exposed in Brazil, and labradorite ($An_{52.8}Ab_{44.2}Or_{3.0}$) from a basaltic sill in the eastern Klamath Mountains, USA (sample HMS-2; Renne and Scott, 1988). We have no detailed information regarding the microtexture or degree of Al-Si order in these feldspars. Arrhenius plots obtained from these samples can be divided into two portions: (1) a low-T, linear array, and (2) a high-T, downwardly curved array. We propose that these segments are associated with the triclinic and transitional structures, respectively. Thus the transitional structure of these feldspars, like that of the Na-rich samples discussed above, is associated with downward curvature on Arrhenius plots. Further study of Ar diffusion in feldspars with well defined, low-T monoclinic-triclinic transition temperatures (e.g., Pb-feldspar, Benna et al., 2000; synthetic ternary feldspars, Kroll and Bambauer, 1981) would be productive in better delineating the relationship between symmetry changes and noble gas diffusion.

5.5. K-rich feldspars

Unexsolved K-rich feldspars (e.g., sanidine and orthoclase) are unique amongst ternary feldspars in that they exhibit monoclinic symmetry at room temperature. Because the tetrahedral framework is held apart by large K atoms (i.e., it is not puckered about small Na cations; Fig. 5.6d), a displacive transition does not occur during incremental heating experiments. Rather, unit cell dimensions *a*, *b*, and *c* increase approximately linearly as a function of temperature, with more expansion accommodated along the *a*-axis (Fig. 5.7e,f; Brown et al., 1984; Hovis et al., 1999; Mackert et al., 2000). Arrhenius plots obtained from such K-rich feldspars mirror the simplicity of their thermal expansion. For example, Figure 5.10 depicts the results of diffusion experiments conducted on two disordered, K-rich feldspars: sanidine ($An_{3.7}Ab_{30.5}Or_{65.8}$) from a ~108 ka rhyolitic ash deposited within layered marine sediments in the Gulf of Salerno off the west coast of Italy and sanidine ($\sim An_1Ab_{27}Or_{72}$; Bachmann et al., 2002) from the ~28 Ma Fish Canyon Tuff. The Arrhenius plots are linear at all temperatures below their melting points. Figure 3.2 depicts the results of diffusion experiments conducted on four aliquots of Benson Mines orthoclase (described in Chapter 3). Like the sanidine crystals, Benson Mines orthoclase yields robust, linear Arrhenius arrays (Fig. 3.2), with only modest departures from linearity manifest near the melting point in data acquired from a bulk grain and {010} cleavage flake. Such behavior may be indicative of a slowing or cessation of expansion along the *c*-axis, which could cause downward curvature on Arrhenius plots obtained from grain fragments that include diffusion normal to the *c*-axis (i.e., in the *a* and *b* directions). Unfortunately, we are not aware of

thermal expansion or detailed structural data on orthoclase at these temperatures. To summarize, monoclinic K-rich feldspars (i.e., sanidine and orthoclase), unlike other ternary feldspars, do not undergo structural or thermal expansion regime changes when heated and yield linear Arrhenius arrays at temperatures below ~1000 ºC.

Figure 5.9: Arrhenius plots for (**a**) Klamath Mountains labradorite (^{37}Ar), (**b**) extraterrestrial (from achondrite GRA 06128) albite/oligoclase (^{37}Ar), (**c**) Paraná Traps andesine (^{37}Ar), and (**d**) Fish Canyon Tuff oligoclase (^{37}Ar) crystals, calculated using equations for spherical geometry. Uncertainties in D/a^2 values are generally smaller than the symbols, but are not shown. Leftward curvature observed at high-T is associated with the structural transition from triclinic toward monoclinic symmetry. Because monoclinic symmetry is not achieved below the melting temperature, a high-T linear Arrhenius arrays, as obtained from more Na-rich feldspars (e.g., Fig. 5.8), are not observed.

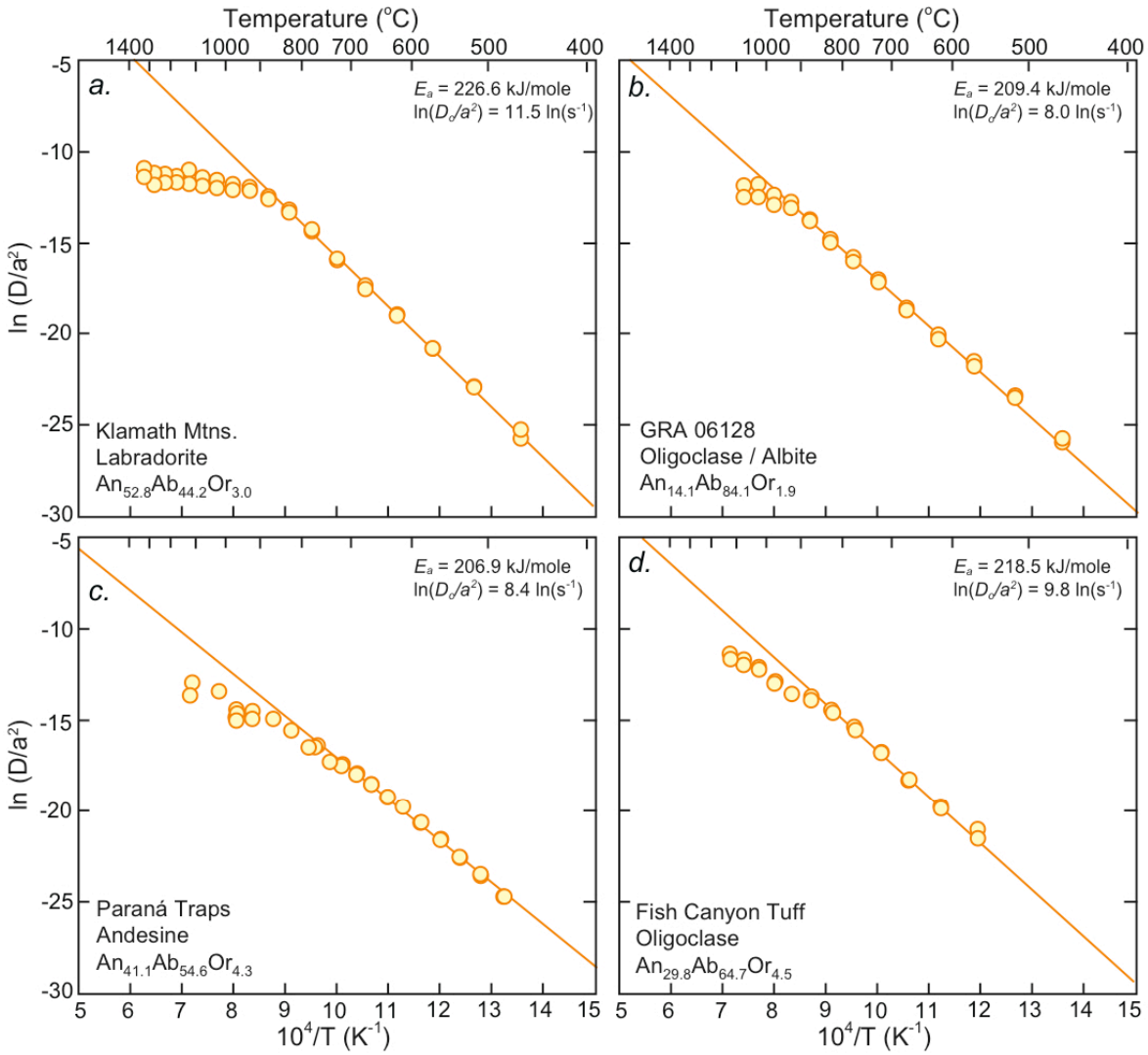

Figure 5.10: Arrhenius plots for (**a**) Fish Canyon Tuff sanidine (^{39}Ar) and (**b**) Gulf of Salerno sanidine (^{39}Ar) crystals, calculated using equations for spherical geometry. Uncertainties in D/a^2 values are generally smaller than the symbols, but are not shown. These Arrhenius arrays, along with those for Benson Mines orthoclase (Fig. 2), are the most linear that we observed in this study. Arrhenius plots obtained from these K-rich feldspars mirror the simplicity of their thermal expansion. Unlike other ternary feldspars, sanidine and orthoclase do not undergo significant changes in unit cell angles and cation coordination when heated.

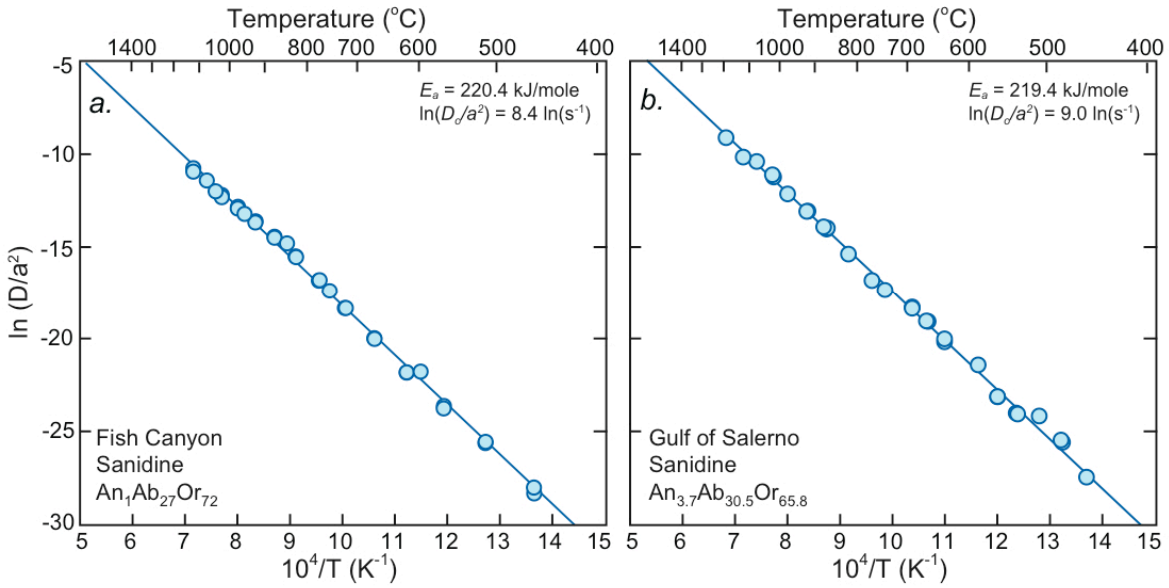

5.6. Ca-rich feldspars

Ca-rich plagioclase specimens ($An_{>45}$) belonging to the *I1*, *T*, *P1*, e_1, and e_2 structural groups (Fig. 3.3) are unique amongst ternary feldspars in that Arrhenius arrays (Figs. 3.5 and 5.2) invariably curve upward at intermediate heating temperatures (600-800 °C), prior to downward curvature at higher temperatures (>900 °C). This behavior occurs in Ca-rich plagioclase specimens of both high (disordered) and low (ordered/exsolved) structural states (discussed below), and is therefore not related to the modulated *e*-plagioclase structures associated with the Huttenlocher and Boggild solvi (Fig. 3.3), wherein nanometer-sized albite-like domains separate anorthite-like domains in antiphase relationship (e.g., Wenk and Nakajima, 1980). As discussed previously, upward curvature also does not reflect a reduction in the grain size with heating (i.e., thermal fracturing) or temperature-dependent anisotropy (i.e., the increasing importance of diffusion along a given crystallographic axis), and therefore presumably reflects a unique aspect of the structural response of Ca-rich feldspars to heating.

Before we expound upon some potential crystallochemical causes of the unique behavior exhibited by Ca-rich feldspars, here we review their crystal structure and changes that occur when heated. We discuss the Ca-rich feldspars in two groups: (1) anorthite ($An_{>95}$) and (2) intermediate plagioclase ($An_{\sim 45\text{-}95}$). At room temperature, the unit cell of anorthite has four

non-equivalent M-site locations due to lattice distortions associated with its high Al concentration (*P1* symmetry; Megaw et al., 1962). The non-equivalent M-sites give rise to c-reflections in x-ray diffraction patterns (Foit and Peacor, 1973), and can be grouped into two dissimilar pairs based on their average M-O distances (i.e., coordination environments; Megaw et al., 1962). At room-T, the lattice distorts about the small, divalent Ca atoms in one of two undifferentiated ways related by *C2* symmetry (i.e., the lattice can distort "left" or "right"). Random nucleation will produce both left and right domains, each of which contain the four non-equivalent M-sites. This process is somewhat analogous to the formation of "left" and "right" domains in orthoclase, wherein Al orders on equivalent T_1-sites related by mirror symmetry, creating a tweed microtexture (Parsons and Lee, 2005). Likewise, at room temperature intermediate plagioclase specimens (e_1, e_2, and *I1*) have non-unique M-site positions that give rise to e-reflections in x-ray diffraction patterns (Wenk et al., 1980; Wenk and Nakajima, 1980), and the lattice can distort in "left" and "right" arrangements related by $^1/_2(a + b + c)$ symmetry (Brown, 1984). At ~300 °C, the mosaic of "left" and "right" domains in *P1*-anorthite become increasingly small until body-center (*I1*) average symmetry is attained at the *P1-T* transition (Fig. 3.3; Smith and Ribbe, 1969; Brown, 1984; van Tendeloo et al., 1989). Again, *T*-anorthite is somewhat analogous to orthoclase in the sense that an average property is inferred (*I1* symmetry) from sub-micron domains having another property (*P1* symmetry). This transition is reversible upon cooling at a sufficiently slow rate, but can be quenched in rapidly cooled samples, giving rise to diffuse (as opposed to sharp) c- or e-reflections at room temperature (Mueller et al., 1972; Wenk et al., 1978). At higher temperatures yet (>800 °C), the framework becomes less puckered about the small Ca cations, only two non-equivalent M-sites exist (Megaw et al., 1962; Brown, 1984), c-reflections disappear in anorthite (Foit and Peacor, 1973; Wenk et al., 1973), e-reflections disappear in intermediate plagioclase (Foit and Peacor, 1967; Bown and Gay, 1969), and true body-center (*I1*) symmetry is attained.

As noted above, Arrhenius arrays obtained from Ca-rich feldspars are considerably more complex than those discussed previously, exhibiting upward curvature on at intermediate temperatures (600-800 ºC; Fig. 5.2). Because this behavior appears only to occur in specimens belonging to the *I1*, *T*, *P1*, e_1, and e_2 structural groups, it may reflect anisotropic changes in cation location or bond lengths and angles associated with the non-equivalent M-site environments unique to these feldspars. Such a discontinuous response of the lattice to heating is not entirely unexpected given the dissimilar bonding environments of the M-site pairs (discussed above). If this behavior is typical of Ca-rich feldspars, then the potential energy barriers to diffusion should change discontinuously with temperature, giving rise to Arrhenius non-linearity.

We are only aware of 4 studies on thermal expansion in Ca-rich feldspars (Stewart et al., 1966; Grundy and Brown, 1974; Tribaudino et al., 2010; Hovis et al., 2010), two of which contain sufficiently detailed data to warrant further discussion. Tribaudino et al. (2010) present expansion data between 25 and 700 °C for plagioclases of compositions An_{100} and An_{60}. Expansion in the An_{100} plagioclase is approximately linear between 350 and 700 °C, a temperature range over which linearity is observed on Arrhenius plots for feldspars of similar composition (Fig. 5.2). A significant change in volume associated with the *P1-T* structural

transition occurs at ~225 °C, which likely precludes extrapolating Arrhenius relationships defined by higher-T data down to geologically relevant conditions (discussed below). The rate of expansion in the An_{60} plagioclase increases at temperatures above 500-600 °C, a temperature range over which upward deviations from linearity commence on Arrhenius plots (Fig. 5.2). Hovis et al. (2010) present expansion data between 22 and 925 °C for several Ca-rich feldspar compositions. The data are significantly less detailed than that of Tribaudino et al. (2010), but generally define approximately linear to curvilinear arrays. For the purposes of comparing thermal expansion and Ar diffusion, in Figure 5.11 we show linear regressions to the expansion data of Hovis et al. (2010) acquired above and below 600 °C, the temperature at which significant deviations from linearity arise on Arrhenius plots. The rate of thermal expansion appears to increase above 600 °C in Ca-rich specimens, while it appears to slow in Na-rich specimens. We are not aware of detailed thermal expansion data at higher-T (>900 °C), but Ca-rich feldspars approach monoclinic symmetry (Phillips et al., 1997). Predicted triclinic-monoclinic transition temperatures are in excess of Ca-rich feldspar melting points, but decrease with increasing K and Na content or the incorporation large cations like Sr, Ba, and Pb (e.g., Benna et al., 2000; Benna and Bruno, 2001). We assume the pronounced downward curvature observed on Arrhenius plots above 800-900 °C reflects a slowing or cessation of expansion, primarily in the *b-c* plane of the crystal, along with a normalization of interstitial M-O bond lengths, as in the approach toward monoclinic symmetry in Na-rich feldspars, resulting in significant changes to the potential energy barriers to diffusion. Interestingly, Foit and Peacor (1967) observed an increasing diffuseness of a- and b-reflections in x-ray diffraction patterns between 600-1000 °C in Ca-rich feldspar, which Smith and Ribbe (1969) suggest reflects a change in the vibrational mode of the framework; Bloss (1964) observed an inflection in a curve of optical extinction angle vs. temperature at 800 °C; Kohler and Weiden (1954) observed an endothermal differential thermal analysis peak at 800 °C.

Thus we can draw an analogy between Ca-rich and Na-rich feldspars. In both feldspars, the structure is distorted about the small cations at low-T regardless of structural state. As Na-rich feldspars are heated, expansion first proceeds linearly, giving rise to approximately linear Arrhenius plots. Subsequently, the normalization of M-O distances and changes in bond angles are manifest as downward curvature on Arrhenius plots. Likewise, as Ca-rich feldspars are heated and expansion proceeds, diffusivity increases approximately linearly on Arrhenius plots, and downward curvature is manifest at high-T. However, in the case of Ca-rich feldspars, changes in the potential energy barriers to diffusion appear to be more complex, giving rise to upward curvature at intermediate temperatures. Given that upward curvature is only manifest on Arrhenius plots obtained from feldspars that yield e- and c-reflections (discussed above), such behavior may reflect variable thermal expansion about the non-equivalent M-sites pairs that have different coordination environments and, presumably, different vibrational responses to heating. Detailed structural measurements of M-O and O-O bond lengths and angles in Ca-rich feldspars at high temperature would be productive in better delineating the relationship between structural changes and upward curvature observed on Arrhenius plots.

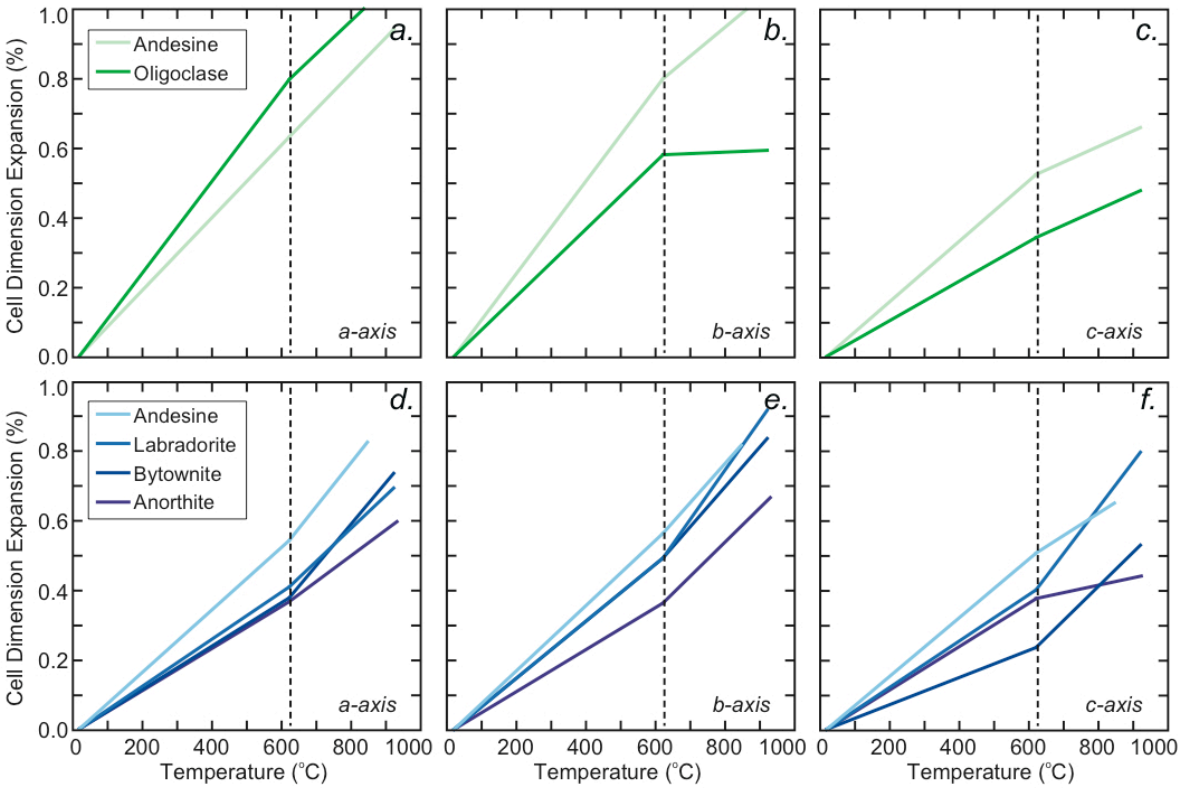

Figure 5.11: Linear regressions to plagioclase thermal expansion data acquired at temperatures above and below 600 °C by Hovis et al. (2010). Above 600 °C, the rate of cell dimension expansion decreases in Na-rich specimens (**a**,**b**,**c**) and increases in Ca-rich specimens (**d**,**e**,**f**).

5.7. Exsolved alkali feldspars

We now return to Arrhenius plots obtained from a "gem-quality", cryptoperthitic alkali feldspar from a pegmatite in Madagascar (discussed above and in Chapters 3 and 4). Recall that this specimen comprises micron-sized orthoclase lamellae with "tweed" microtexture and sub-micron albite lamellae (Parsons and Lee, 2005). Arrhenius plots obtained from this sample exhibit downward curvature at ~800 °C (Fig. 3.2), similar to Na-rich feldspars (Fig. 5.8), although damped in magnitude. Such curvature presumably reflects the triclinic to monoclinic symmetry transition in albite lamellae, as well as resulting changes in lamellar interface strain. Orthoclase specimens with high concentrations of Ca and Na and/or high T-site order exhibit framework distortions similar to Na-rich feldspars at room temperature, with irregular M-sites comprising 7 shorter and 2 longer M-O bond lengths (Brown, 1984). Thus it appears that a minor modal abundances of albite lamellae (e.g., 5%), coupled with high T-site order, cause Madagascar cryptoperthite to diffuse more similarly to Na-rich feldspars like ECC anorthoclase (Fig. 5.8) than monoclinic K-rich feldspars like Fish Canyon sanidine (Fig. 5.10) or Benson Mines orthoclase (Fig. 3.2). We presumably obtained a linear Arrhenius plot for Ne diffusion in Madagascar cryptoperthite (Fig. 5.1) because ^{22}Ne was completely

degassed between 200 and 600 °C, a range over which no significant structural changes occur within albite lamellae.

In the above example we highlighted results from a "gem-quality", exsolved alkali feldspar. Often alkali feldspars analyzed for thermochronometry are more complex, with deuteric alteration or fractures reducing the effective domain size to sub-grain dimensions. Under these circumstances, curvature on Arrhenius plots should result from both a range in sub-grain domain sizes and structural changes that occur in Na-rich lamellae. For example, Figure 3.6 depicts the results of diffusion experiments conducted on fragments of deuterically altered, exsolved alkali feldspar from the Bushveld Complex, South Africa (discussed in Chapter 3). The crystals contain strain-controlled, coherent to semicoherent film perthite crosscut by incoherent (microporous) patch and vein perthite resulting from deuteric alteration. Deviations from linearity manifest on Arrhenius plots are substantially greater than those observed from the more pristine cryptoperthite from Madagascar (Figs. 3.2 and 5.1) or anorthoclase from Easy Chair Crater (Fig. 5.8). It is not clear how much of the observed deviation from linearity is due to a range in sub-grain domain size, and how much is due to structural changes occurring at temperature. When fitting such an Arrhenius plot with a multiple diffusion domain model, a correction must be made to account for the structural change before the apparent diffusion parameters can be extrapolated down in temperature to geologically relevant conditions (discussed below).

5.8. Reversibility

A key prediction of our hypothesis relating "at-temperature" structural changes to deviations from linearity manifest on Arrhenius plots is that such curvature is reversible, insofar as the structural changes are reversible. Simple angular changes of the framework associated with thermal expansion only require a fraction of a second to occur (i.e., the time required for the passage of a thermal wave), but structural transitions associated with changes in M-O coordination have an activation energy related to the breaking and reforming of bonds (Smith and Ribbe, 1969). Thus while simple thermal expansion is reversible, changes in unit cell dimensions and angles associated with structural changes are not purely second order (Brown et al., 1984; Salje et al., 1985). For example, Barth (1965) and Stewart and von Limbach (1967) showed that the triclinic-monoclinic transition in Na-rich feldspars is not immediately reversible upon cooling. Furthermore, disordered Na-rich feldspars attain monoclinic symmetry at much lower temperatures (by ~200 °C) than more ordered feldspars of identical composition (Stewart and von Limbach, 1967; Grundy and Brown, 1969; Kroll et al., 1980; Hovis, 1980; Brown et al., 1984), and the critical temperature changes even if minor T-site ordering is induced by heating (Barth, 1965; Stewart and von Limbach, 1967). Thus changes in the feldspar structure are themselves kinetically controlled, with an associated potential energy barrier to be overcome when heated, and exhibiting hysteresis when cooled.

Arrhenius plots obtained from feldspars subjected to cycled (i.e., prograde and retrograde) heating schedules are consistent with the abovementioned description of structural changes that occur at temperature. Retrograde heating following temperatures at which downward

curvature is manifest on Arrhenius plots obtained from Na-rich feldspars yields ln(D/a^2) values that approach those observed in prior prograde heating cycles at lower-T (i.e., downward curvature is reversible, but with some hysteresis; Fig. 5.12a,b,c). Likewise, retrograde heating following temperatures at which upward curvature is manifest on Arrhenius plots obtained from Ca-rich feldspars yields ln(D/a^2) values that approach those observed in prior prograde heating cycles at lower-T (i.e., upward curvature is reversible, but with some hysteresis; Fig. 5.12d,e,f). In a prograde heating cycle, reducing the number, duration, and temperature spacing of extractions appears to delay departures from linearity associated with the triclinic to monoclinic transition by 50 °C or more (Figs. 2a and 20a), which is consistent with the attendant structural changes having associated potential energy barriers. Conversely, such a heating schedule does not appear to delay upward curvature on Ca-rich feldspar Arrhenius plots (Fig. 5.12f), which is consistent with non-linearity due to simple changes in thermal expansion regime. Prograde and retrograde heating within low-T portions of Arrhenius plots not associated with structural changes yield reproducible values of ln(D/a^2) at any given temperature (Figs. 5.10 and 5.12a,c; Cassata et al., 2009). Thus Ar diffusion experiments are generally consistent simple thermal expansion occurring at low-T and non-second-order phase transitions occurring at higher-T. For comparison, in Figure 5.13 we show Arrhenius plots obtained from plagioclase crystals from the Bushveld Complex, South Africa, that contain quartz and alkali feldspar sub-grains, and thus a range in diffusive lengthscales. By inspection it is clear that retrograde heating does not yield ln(D/a^2) values that reproach those observed in prior prograde arrays, but rather yields sub-parallel linear arrays consistent with MDD theory.

5.9. Summary

Ar diffusion in feldspars proceeds primarily through metal-oxygen and oxygen-oxygen interstitial lattice configurations, as well as through vacancies and extended linear and planar defects. The potential energy barrier associated with a given interstitial lattice configuration is strongly dependent on the distance between an Ar atom and the lattice atoms, and therefore highly sensitive subtle changes in dimension and geometry that occur when feldspars are heated. Segments of linearity observed on Arrhenius plots appear to coincide with temperature intervals over which unit cell angles, dimensions, and volumes change in a linear to curvilinear manner with temperature. Deviations from linearity appear to coincide with structural changes induced by heating (i.e., they reflect discontinuous changes in the diffusive medium). Thus Ar diffusion in feldspars, and more generally noble gas diffusion in silicates, cannot solely be described by simple, temperature-independent potential energy barriers and associated vibrational frequencies. Rather, the potential energy barriers to diffusion and associated vibrational frequencies vary with temperature, in some instances giving rise to linear Arrhenius arrays from which apparent activation energies and frequency factors can be inferred, and in other instances yielding curved or discontinuous Arrhenius arrays. Critical to thermochronometry is an understanding of whether or not diffusivities at geologically relevant temperatures differ significantly from down-temperature extrapolations of linear Arrhenius relationships established during laboratory heating experiments.

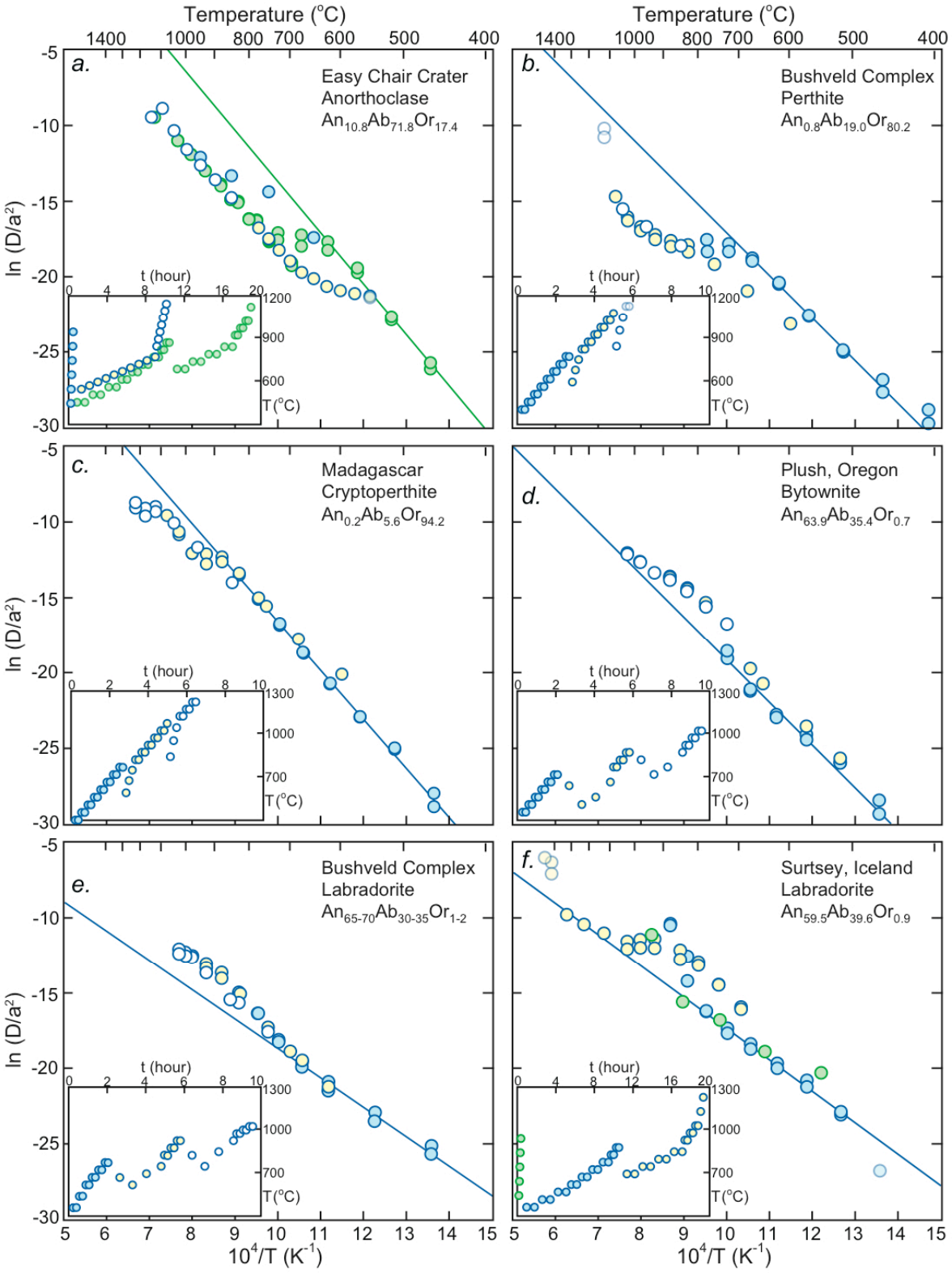
Temperature (°C)
1400 1000 800 700 600 500 400
a.
Easy Chair Crater
Anorthoclase
An10.8Ab71.8Or17.4
b.
Bushveld Complex
Perthite
An0.8Ab19.0Or80.2
c.
Madagascar
Cryptoperthite
An0.2Ab5.6Or94.2
d.
Plush, Oregon
Bytownite
An63.9Ab35.4Or0.7
e.
Bushveld Complex
Labradorite
An65-70Ab30-35Or1-2
f.
Surtsey, Iceland
Labradorite
An59.5Ab39.6Or0.9
ln (D/a²)
10⁴/T (K⁻¹)
t (hour)
T(°C)

Figure 5.12: Arrhenius plots for (**a**) Easy Chair Crater anorthoclase (^{39}Ar), (**b**) Bushveld Complex perthite (^{39}Ar), (**c**) Madagascar cryptoperthite (^{39}Ar), (**d**) Plush bytownite (^{37}Ar), (**e**) Bushveld Complex labradorite (^{37}Ar), and (**f**) Surtsey labradorite (^{37}Ar) crystals subjected to cycled (prograde and retrograde) heating schedules, calculated using equations for (**a**,**f**) infinite sheet and (**b**,**c**,**d**,**e**) spherical geometries. Uncertainties in D/a^2 values are generally smaller than the symbols, but are not shown. The laboratory heating schedules are shown in the insets. Colors correspond to heating schedule cycles. These data illustrate the reversibility of curvature observed on feldspar Arrhenius plots (see text for detailed discussion).

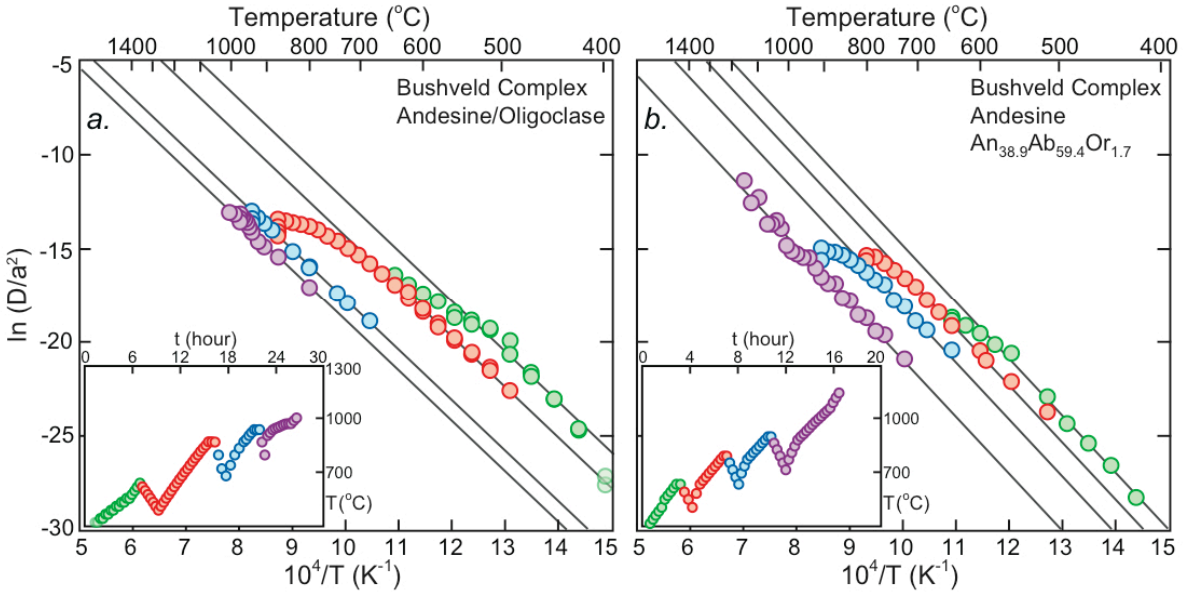

Figure 5.13: Arrhenius plots for (**a**) Bushveld Complex andesine/oligoclase with magnetite inclusions (^{37}Ar) and (**b**) Bushveld Complex andesine (^{37}Ar) crystals subjected to cycled (prograde and retrograde) heating schedules, calculated using equations for spherical geometry. Uncertainties in D/a^2 values are generally smaller than the symbols, but are not shown. The laboratory heating schedules are shown in the insets. Colors correspond to heating schedule cycles. These samples contain quartz and alkali feldspar sub-grains, and illustrate that low-T curvature observed on Arrhenius plots obtained from some *C1* plagioclase feldspars that comprise multiple diffusion domains yield irreversible Arrhenius arrays over specific temperature intervals.

Table 5.1: Definitions of thermal expansion model parameters and their values

Parameter	Notation	Parameter Value	Parameter Unit	Equation
Crystal dimensions at 0 °C	A_0, B_0, C_0	100	μm	
Unit cell dimensions at 0 °C	a_0, b_0, c_0	3.00	Å	
Jump distance at 0 °C (i.e., unit cell width)	d_0	3.00	Å	1
Interstitial distance between Ar and lattice atoms at 0 °C	$r_{Ar\text{-}X}$	2.12	Å	1
Ar-O Lennard-Jones energy parameter[a]	$\varepsilon_{Ar\text{-}O}$	0.9143	kJ/mole	1
Ar-Ca Lennard-Jones energy parameter[a]	$\varepsilon_{Ar\text{-}Ca}$	1.7453	kJ/mole	1
Ar-Na Lennard-Jones energy parameter[a]	$\varepsilon_{Ar\text{-}Na}$	2.4929	kJ/mole	1
Ar-O Lennard-Jones size parameter[b]	$\sigma_{Ar\text{-}O}$	3.0566	Å	1
Ar-Ca Lennard-Jones size parameter[b]	$\sigma_{Ar\text{-}Ca}$	2.5845	Å	1
Ar-Na Lennard-Jones size parameter[b]	$\sigma_{Ar\text{-}Na}$	2.5756	Å	1
Interstitial Ar-O Lennard-Jones potential at 0 °C	$U_{Ar\text{-}O}$	262.2	kJ/mole	1
Vibrational frequency for Ar-O at 0 °C	$\upsilon_{o\ Ar\text{-}O}$	1.91×10^{11}	s^{-1}	2
Tracer diffusion frequency factor for Ar-O at 0 °C	$\nu_{o\ Ar\text{-}O}$	8.59×10^{-9}	m^2/s	3
Thermal expansion coefficient[c]	α	variable	Å/°C	

a: Lennard-Jones energy parameters are from Du et al. (2008).
b: Lennard-Jones size parameters are from Watanabe et al. (1995).
c: Variable thermal expansion coefficients were employed.

Chapter 6.

Geologic relevance of laboratory-derived diffusion parameters

6.1. Introduction

Because crystallochemical changes (e.g., thermal expansion and structural transitions) alter the potential energy barriers to diffusion, care must be taken in extrapolating laboratory-derived diffusion down in temperature to geologically relevant conditions. The problems that arise are twofold. First, if changes in structure or thermal expansion regime occur below the temperatures at which laboratory diffusion experiments are conducted, then laboratory-derived diffusion coefficients are not applicable to lower-T thermal histories. Second, if Arrhenius plots obtained from samples that comprise multiple diffusion domains exhibit curvature due structural transitions, then corrections must be applied to the apparent domain size distribution to account for any such geologically irrelevant non-linearity. It is therefore important to understand the temperatures at which a given composition of feldspar exhibits deviations from linearity on Arrhenius plots due to structural transitions, as well as the magnitude of such deviations. In this section we highlight relevant examples of these problems and explore the extent to which they bias forward modeled thermal histories.

6.2. Ar diffusion in alkali feldspar

Arrhenius arrays obtained from alkali feldspars with highly sodic compositions (e.g., albite and anorthoclase) or lamellae (i.e., perthite) begin to deviate from linearity between 600 and 800 °C due to structural changes associated with the triclinic to monoclinic transition. Likewise, if feldspars comprise a range in sub-grain domain sizes, deviations from linearity typically begin to arise between 400 and 700 °C due the exhaustion of smaller domains. It is generally not possible to completely degas domains with dimensions greater than a few microns at temperature below which structural transitions occur because of the unfeasibly long heating durations required. Thus deviations from linearity associated with both the exhaustion of sub-grain domains and the triclinic to monoclinic structural transition will occur during laboratory heating experiments. As such, extracting meaningful information regarding domain size distributions requires a method for attributing non-linearity to these concurrent processes. Fortunately, no complex structural transitions or thermal expansion regime changes occur in alkali feldspars at low-T (<400 °C), and therefore laboratory-derived diffusion parameters can be extrapolated down in temperature with reasonable confidence, provided that corrections can be made to apparent domain distribution parameters inferred from high-T extractions.

Consider a hypothetical multiple-domain alkali feldspar comprising albite and orthoclase lamellae. Assume it was intruded at 20 km depth 100 Ma ago and was slowly uplifted to the surface. In Figure 6.1a and 6.1b we show a hypothetical age spectrum and Arrhenius plot for this sample, respectively. Deviations from linearity arise on the Arrhenius plot due to both the exhaustion of its sub-grain domains and the monoclinic to triclinic transition in albite lamellae. Corrections must be applied to the apparent domain distribution parameters inferred from the Arrhenius plot to account for the geologically irrelevant non-linearity. In Figures 6.1c and 6.1d we show thermal histories that reproduce the target age spectrum. The thermal histories predicted using the uncorrected domain distribution parameters are erroneously hot (Fig. 6.1d). At a given time, the predicted temperature exceeds the "true" temperature (shown in black) by up 40 °C. Alternatively, the time at which the sample is at a given temperature is erroneously late (young) by up to 15 Ma. These discrepancies increase if more significant deviations from linearity arise due to structural changes (e.g., ECC anorthoclase; Fig. 5.8). Thus considerable inaccuracies may exist in published thermal histories inferred from MDD models fit to Arrhenius arrays obtained from exsolved alkali feldspars.

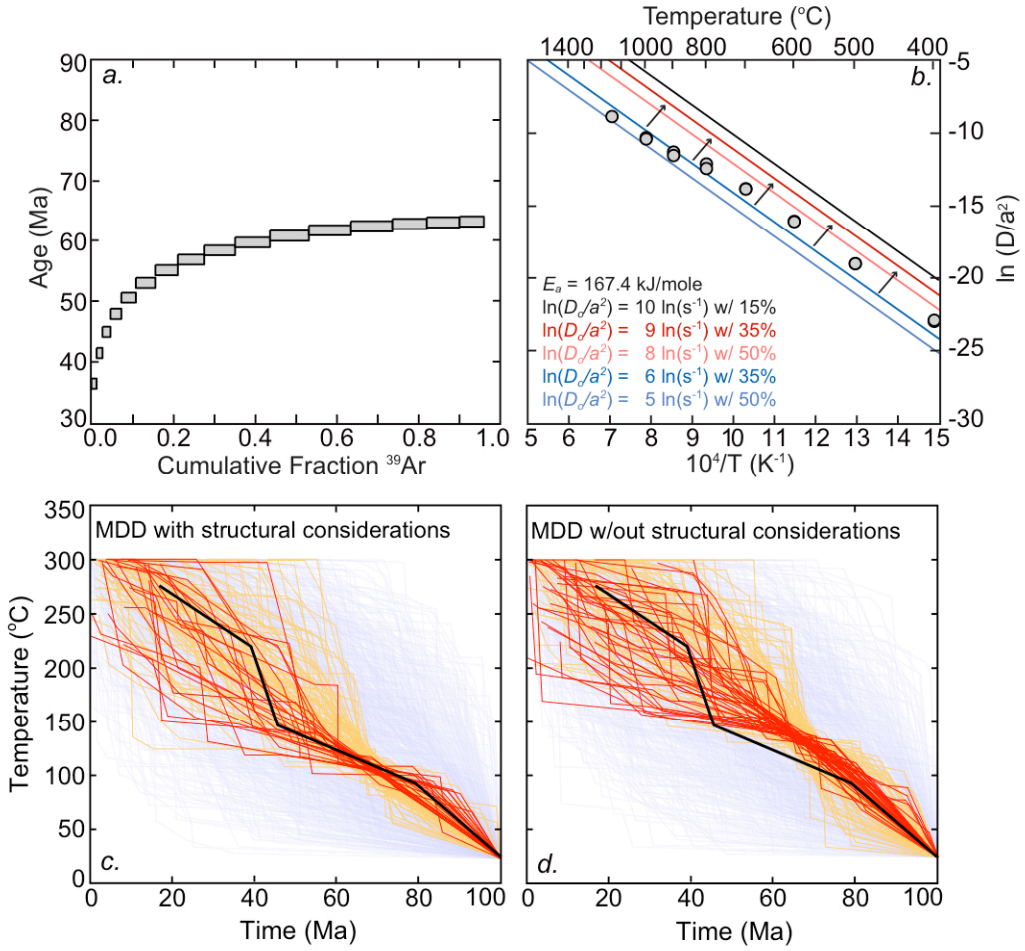

Figure 6.1: (**a**) Hypothetical age spectrum obtained from a multiple-domain alkali feldspar comprising albite and orthoclase lamellae, intruded at 20 km depth 100 Ma ago, and slowly uplifted to the surface. (**b**) Hypothetical Arrhenius array (gray) obtained from this sample shown alongside the inferred domain Arrhenius relationships (black and blue lines; domain distribution parameters listed in the lower, left corner) and true domain Arrhenius relationships (black and red lines; domain distribution parameters listed in the lower, left corner). Differences arise between the true and inferred domain Arrhenius relationships because deviations from linearity arise during incremental heating experiments due to both the exhaustion sub-grain domains and structural transitions that occur "at-temperature". Corrections (denoted schematically by arrows) must be applied to the inferred domain distribution parameters to account for non-linearity associated with structural transitions, which is geologically irrelevant. (**c**) Simulated thermal histories using the true (corrected) domain distribution parameters. Thermal histories that best reproduce the target age spectrum are shown in red (orange = moderate fit; blue = poor fit). The black line (an average of the best fit solutions) represents an accurate thermal history. (**d**) Simulated thermal histories using the inferred (uncorrected) domain distribution parameters. The uncorrected diffusion parameters yield an anomalously hot Ar partial retention zone.

A further concern in assessing the accuracy of MDD models is establishing the temporal relationship between the formation of alteration surfaces, fractures, and other domain-defining features and the thermal history of interest (i.e., constraining the stability of the domain over geologic time). Alkali feldspars extracted from undeformed granites whose alteration and crystallization features are characterized only by comagmatic microtextures (e.g., deuteric turbidity, strain-controlled exsolution, symplectically-crystallized myrmekite, etc.) represent suitable candidates for thermochronometry (e.g., McLaren & Reddy, 2008). The presence of stress-induced fractures, complex grain boundary orientations (e.g., McLaren & Reddy, 2008), clay minerals, and/or dissolution-precipitation features associated with post-magmatic tectonic and hydrothermal activity render a given sample questionably reliable for thermochronometry. Likewise, pervasive low or high temperature excess argon, intermediate age maxima (i.e., double-humped age spectra), and/or a lack of correlation between age and kinetic (i.e., $\ln(r/r_o)$) data render a sample of questionable reliability (Lovera et al., 2002). Petrographic and microanalytical observations are, of course, necessary to determine the suitability of a given sample for thermal modeling (Parsons, 1999).

Beyond understanding the suitability of a given alkali feldspar for thermochronometry and applying corrections to apparent domain distribution parameters to account for structurally-related deviations from linearity, further complications exist in relating laboratory-derived diffusion kinetics to geologically relevant temperatures and timescales. In our experience, approximately one out of every five carefully selected fragments of a pristine and apparently single-domain feldspar sample yielded anomalous results consistent with multiple diffusion domains, presumably due to the presence of microfractures associated with sample preparation and handling that were not identified. Diffusion kinetics inferred from furnace

heating experiments on tens of milligrams of these pristine feldspars would therefore reflect the release of Ar from both geologically relevant domains, as well as laboratory-induced anthropogenic domains. Thus laser or furnace heating of individual crystals or crystal fragments, as employed in this study (and more generally by the U-Th-He community), appears necessary, albeit unfeasible in some instances, to avoid biasing Arrhenius arrays. Additionally, because Ar diffusion in feldspars is dependent on composition (discussed in more detail below), diffusivity may be spatially variable within exsolved feldspars. The effect that exsolution lamellae of different shapes and sizes, spatial distributions, and diffusive and compositional contrasts relative to the host have on apparent diffusion parameters and inferred thermal histories has not been quantitatively assessed, despite the routine analysis of perthitic alkali feldspars for $^{40}Ar/^{39}Ar$ thermochronometry (e.g., Heizler and Harrison; 1998; McLaren *et al*., 2007; Harrison *et al*., 2010; Parsons *et al*., 2010).

6.3. Ar diffusion in plagioclase feldspar

Plagioclase feldspars with compositions of $An_{<95}$ do not undergo structural transitions or thermal expansion regime changes at temperatures associated with the Ar partial retention zone (100-400 °C; Tribaudino et al., 2010). Therefore, laboratory-derived diffusion parameters based on linear Arrhenius arrays can be extrapolated down in temperature with reasonable confidence, provided that the sample of interest can be shown to diffuse at the grain scale. Plagioclase feldspars comprising a range in sub-grain domain sizes pose unique problems for thermal modeling. It is generally not possible to completely degas domains with dimensions greater than tens of microns at temperature below which either (1) upward curvature associated with the intermediate-T (600-700 °C) structural transition occurs in Ca-rich feldspars (Fig. 5.2), or (2) downward curvature associated with the high-T (>800-900 °C) structural transition toward monoclinic symmetry occurs in all plagioclase feldspars. As with alkali feldspars, corrections must be applied to apparent domain distribution parameters extracted from multi-domain Arrhenius arrays to account for deviations from linearity that arise due to these structural changes.

In the case of Ca-rich feldspars, the manifestation on Arrhenius plots of the 600-700 °C structural transition (upward curvature) is opposite that of a range in sub-grain domain sizes (downward curvature). Thus apparent domain size distributions inferred from this interval of Arrhenius plots underestimate true variations in domain size. The Arrhenius plots are further complicated (or initially complicated in the case of Na-rich plagioclase feldspars) by downward curvature at high-T (>800-900 °C) due to the structural transition toward monoclinic symmetry. Because monoclinic symmetry is never achieved, Arrhenius curvature persists through the melting temperature (i.e., linearity is never re-established on Arrhenius plots; Fig. 5.9), rendering it difficult to deconvolve curvature due to a range in sub-grain domain sizes from that due to the structural changes. Knowledge of the temperature at which a pristine, single-domain crystal of a given feldspar exhibits downward curvature, and the magnitude of the deviation from linearity as function of temperature, are required to accurately correct apparent domain distribution parameters inferred from such multiple-domain Arrhenius plots. It seems that extracting geologically relevant domain distribution parameters from plagioclase feldspars comprising a range in sub-grain domain sizes may, in

many instances, be prohibitively difficult. One potential approach to placing constraints on thermal histories using these feldspars is to disregard correcting Arrhenius arrays for deviations from linearity arising due to structural changes. By fitting Arrhenius arrays with apparent, albeit erroneous, domain distribution parameters, one can place upper bounds on temperatures at a given time.

One further complication unique to plagioclase feldspars with compositions of $An_{>95}$ is a significant change in thermal expansion regime and unit cell volume associated with the low-T (~300 °C) *P1-T* symmetry transition (Fig. 3.3). Unfortunately, it is not possible to determine single crystal Ar diffusion kinetics at temperatures <300 °C and therefore quantify the affects of the *P1-T* transition due to the unfeasibly long heating durations required to generate measurable signals. Because cooling below the transition temperature is accompanied by a significant reduction (contraction) in unit cell volume (Tribaudino et al., 2010), one might suspect that diffusivity at low-T is slower than that inferred from a down-temperature extrapolation of a linear, higher-T Arrhenius array. Accordingly, using apparent diffusion parameters inferred from laboratory heating experiments to model thermal histories may yield erroneously cold results, as the true diffusion kinetics may be slower, and therefore higher temperatures may be required to predict a given age spectrum. Measurements of He diffusion in anorthite would be productive in assessing potential deviations from linearity that might arise due to the *P1-T* structural transition.

Chapter 7.

Implications for other thermochronometers

7.1. Ar diffusion in biotite, hornblende, and muscovite

Having established a relationship between structural state, thermal expansion, and Ar diffusion in feldspars, here we explore the potential implications of such a relationship for Ar diffusion in other commonly analyzed minerals like biotite, hornblende, and muscovite. Simple Arrhenius relationships do not describe the *in vacuo* release of Ar from these hydrous minerals, as dehydration reactions that alter the mineral structures, and therefore the kinetics of Ar diffusion, occur at temperatures above 600 °C in biotite (Gaber et al., 1988; Chon et al., 2003) and above 700 °C in muscovite (Mazzucato et al., 1999) and hornblende (Gaber et al., 1988; Wartho et al., 1991). Similar dehydration reactions have been shown to affect the release of Ar from jarosite (Kula & Baldwin, 2011). We are not aware of any significant structural or thermal expansion regime changes in these minerals at geologically relevant temperatures (i.e., within their respective Ar partial retention zones). Thus laboratory-derived diffusion parameters based on linear Arrhenius arrays can be extrapolated down in temperature with reasonable confidence. However, because dehydration reactions that occur during laboratory heating above 600 °C significantly alter unit cell dimensions, thermal expansion, and cation coordination (see e.g., muscovite; Mazzucato et al., 1999), higher-T diffusion parameters associated with non-linear portions of Arrhenius arrays probably cannot be used to infer sub-grain domain size distributions, as recently suggested by Harrison et al. (2009) based on the *in vacuo* release of Ar from muscovite. While a correlation between the kinetic [e.g., $\ln(r/r_o)$] and age data (Harrison et al., 2009) undoubtedly suggests that geologically relevant sub-grain domains exist (e.g., Cosca et al., 2011), the challenge lies in determining how much of an observed deviation from linearity reflects the exhaustion of sub-grain domains, and how much reflects the changing potential energy barriers to diffusion associated with structural transitions. Deconvolving these two processes requires detailed knowledge of the Arrhenius behavior of a single-domain crystal of a given muscovite. Thus corrections probably need to be applied to apparent domain distribution parameters before they can be extrapolated down in temperature to geologically relevant conditions.

7.2. He diffusion in apatite, zircon, and titanite

Here we explore the potential implications of a relationship between structural state, thermal expansion regime, and noble gas diffusion on U-Th-He thermochronometry. We begin with apatite, which undergoes approximately linear thermal expansion with increasing temperature below 200 °C (Hopkins et al., 1971; Brunet et al., 1999; Knyazev et al., 2011). Above 200-

350 °C, structural transitions occur in apatite, resulting in abrupt changes in unit cell dimensions and cation coordination. The temperatures at which these transitions occur depend largely on composition. For example, hydroxyapatite and chlorapatite undergo monoclinic to hexagonal phase transitions between 200 and 350 °C (Hitmi et al., 1984; 1986; 1988; Bauer and Klee, 1993). In hydroxyapatite, elevated temperatures produce changes in the location and orientation of OH anions, tilting of PO_4 tetrahedron, and changes in the location of Ca cations (Yashima et al., 2011). Apatite thermal expansion behavior between 200-1000 °C is variable: enhanced thermal expansion is observed above 500 °C in some hydroxyapatite (Brunet et al., 1999; Jena et al., 2011), linear thermal expansion is observed in some chlorapatite and fluorapatite (Brunet et al., 1999), and diminished thermal expansion is observed above 700 °C in some chlorapatite (Knyazev et al., 2011). Weight loss and structural contraction associated with devolatilization reactions have also been reported above 200 °C in some hydroxyapatite (LeGeros et al., 1978; Monma et al., 1981) and above 900 °C in some fluorapatite (Podsiadlo, 1990). To summarize, changes in structure and thermal expansion regime occur in ternary apatite crystals at temperatures above 200 °C. Non-linearity (e.g., upward and downward curvature) manifest on apatite Arrhenius plots at temperatures above ~250 °C (e.g., Zeitler et al., 1987; Wolf et al., 1996; Farley et al., 2000; Shuster et al., 2006) presumably reflects such crystallochemical changes, as well as radiation damage annealing (Shuster et al., 2006; Shuster and Farley, 2009). Because structural and thermal expansion regime changes do not occur at temperatures between those employed in diffusion experiments and those that are geologically relevant (i.e., the He partial retention zone), down-temperature extrapolations of laboratory-derived diffusion parameters should be made with reasonable confidence.

Titanite, on the other hand, undergoes structural transitions at temperatures relevant to both laboratory and geologic heating. At room-T, titanite is monoclinic (space group $P2_1/a$) with alternating short and long Ti-O bonds along TiO_6 octahedral chains (Malcherek et al., 2001). At ~220 °C (Taylor and Brown, 1976; Kunz et al., 2000) this ordered phase transitions to a more disordered monoclinic phase (space group $A2/a$), which is attended by a move of Ti atoms toward the center of their coordination octahedra (i.e., a normalization of Ti-O distances; Kunz et al., 2000; Malcherek et al., 2001). The thermal expansion rate appears to markedly slow, or even become negative, near the transition temperature (Taylor and Brown, 1976; Malcherek et al., 1999). A second, iso-symmetric phase transition occurs at ~550 °C, associated with small changes in interatomic distances and angles such as tilting of TiO_6 octahedra (Malcherek et al., 2001). This high-T transition is attended by an ~0.15% reduction (contraction) in unit cell volume (Malcherek et al., 1999). Published diffusion experiments on titanite (Reiners and Farley, 1999) were conducted between 300 and 500 °C, and thus reflect diffusion in the low-T, $A2/a$ structure. If the thermal expansion and interatomic distance changes associated with the $P2_1/a$ - $A2/a$ structural transition (an approximately isothermal volume contraction) are sufficient to affect diffusion, then the inferred closure temperature for He in titanite may be too high. Likewise, downward curvature might be expected at ~500 °C given the approximately isothermal volume contraction associated the $A2/a$ iso-symmetric structural transition.

The zircon structure is perhaps the simplest of minerals commonly analyzed for U-Th-He

thermochronometry. At room-T zircon is tetragonal, and upon heating it undergoes curvilinear thermal expansion with increasing temperature that can be described by a second order polynomial (i.e., the rate of expansion accelerates with increasing temperature; Mursic et al., 1992; Chaplot et al., 2002; Bose et al., 2010). At high-T (~825 °C), it undergoes a displacive phase transition that is associated with a discontinuity (slowing) in the rate of thermal expansion (Mursic et al., 1992). Although no structural transitions occur at low-T, the non-linear thermal expansion regime discussed above is expected to result in modestly curvilinear Arrhenius arrays that shallow at low-T. Such behavior has been observed on zircon Arrhenius plots (e.g., Reiners et al., 2002; 2004), but could also reflect temperature-dependent anisotropy. Regardless, further experiments at low-T are required to determine whether laboratory-derived diffusion parameters obtained from higher-T, linear arrays can be extrapolated down in temperature with reasonable confidence.

Chapter 8.

Summary of Ar diffusion in feldspars and an atomistic description

8.1. Introduction

In this section we summarize systematic differences in feldspar diffusion parameters (E_a and D_o) and closure temperatures (T_c) as a function of composition and structural state. We attempt to explain such variations in terms of Lennard-Jones potentials, bond lengths and angles, thermal expansion, and ionic porosity. Finally we discuss the relationship between thermal and barometric expansion/compression and the resulting implications for determining the pressure-dependence of diffusivity.

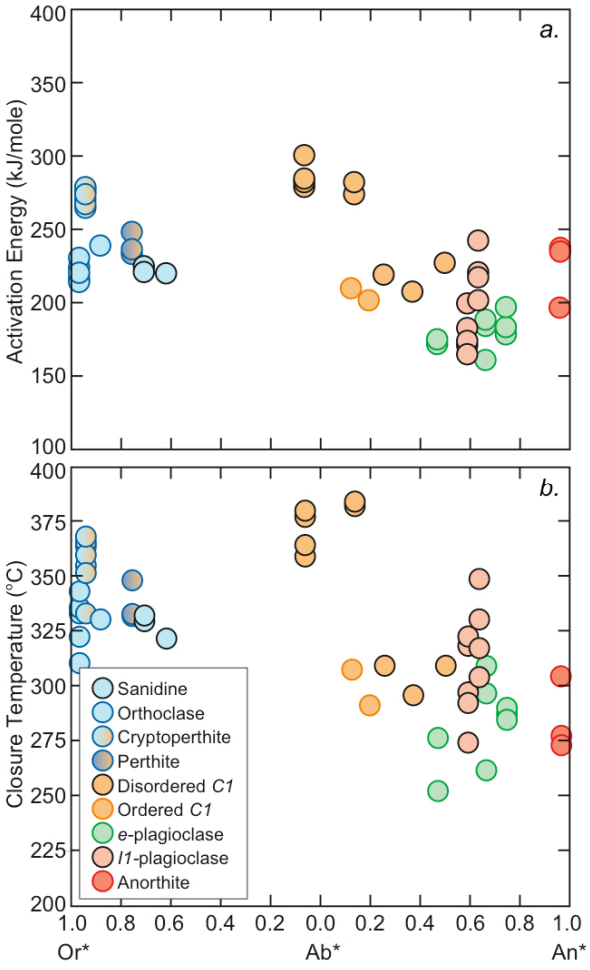

8.2. Systematic differences in diffusion parameters

Apparent activation energies (E_a) and closure temperatures (T_c; Dodson, 1973) as a function of feldspar composition are shown in Figure 8.1. Data included in this figure were acquired by regressing low-T, linear Arrhenius arrays obtained from pristine, unaltered, and presumably single-domain grains. We believe these data can be extrapolated to geologically relevant conditions with reasonable confidence (discussed in Chapter 6). A complete list of apparent diffusion parameters and sample localities, compositions, and structural states is given in Table 8.1. To summarize, Na-, K-, and Ca-rich feldspars yield the highest, intermediate, and lowest activation energies and closure temperatures, respectively, with E_a values between 170 and 285 kJ/mole and T_c values between 200 and 400 °C (calculated assuming a 10 °C/Ma cooling rate). These trends are mirrored by differences in volumetric thermal expansion; Na-, K-, and Ca-rich

Figure 8.1: Summary of (**a**) apparent activation energies and (**b**) closure temperatures as a function of feldspar composition (data given in Table 8.1). Only results from samples inferred to diffuse at or near the grain-scale are shown. Closure temperatures were calculated assuming spherical geometry and a 10 °C/Ma cooling rate. Apparent $\ln(D_o/a^2)$ values obtained from Arrhenius plots that were calculated using equations for infinite sheet geometry (i.e., from cleavage flakes) were corrected by 2.2 natural log units following Huber et al. (2011), such that the inferred closure temperatures are comparable to those obtained from equant grains (see Table 6.1). Ternary compositions (An, Ab, Or; Table 6.1) are represented on this figure as Ab^*, where $Ab^* = An - Or$.

---

feldspars undergo changes in unit cell volume of approximately 0.031, 0.018, and 0.015 %/ºC, respectively (Hovis et al., 1999; Tribaudino et al., 2010). A positive correlation between thermal expansion and apparent activation energy is predicted by molecular dynamics considerations (see Fig. 5.5 and related discussions) if the room temperature potential energy barriers to diffusion are comparable in the phases under consideration (i.e., assuming that one phase does not have an intrinsically different potential energy barrier to diffusion). There also seems to be a tendency for ordered plagioclase feldspars to have lower apparent activation energies than disordered feldspars of equivalent composition. We have not analyzed a sufficient number of ordered alkali feldspars to make such a comparison with disordered alkali feldspars. For experiments in which we were able to obtain comparably precise ^{37}Ar and ^{39}Ar data, we did not observe systematic mass-dependent variations in diffusivity (Fig. 8.2).

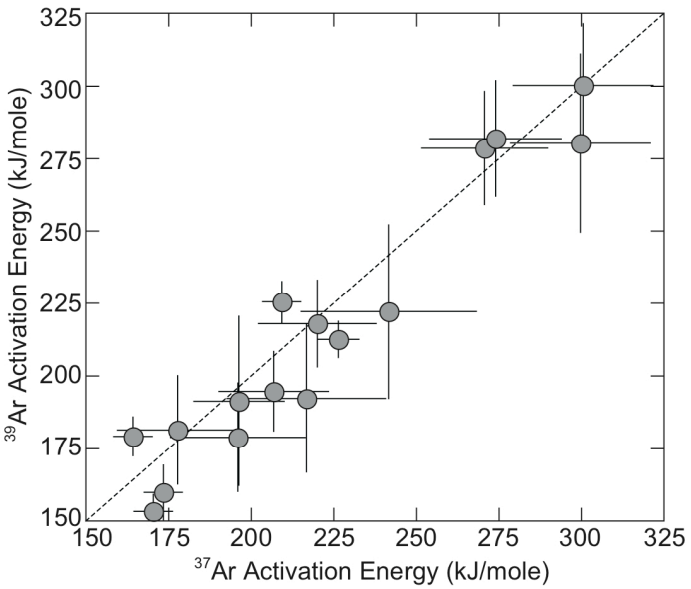

In Figure 8.3 we summarize our diffusion parameters along with the results of two detailed studies on Ar diffusion in alkali feldspars (Lovera et al., 1997; McLaren et al., 2007). We observe an overlapping but more restricted range in alkali feldspar closure temperatures, albeit from a much smaller number of samples. However, it should be noted that the data of Lovera et al. (1997) were obtained from samples comprising a range in sub-grain domains with an inferred size of ~6 μm corresponding to linear segments of Arrhenius arrays – one to two orders of

Figure 8.2: Comparison of apparent activation energies for ^{37}Ar and ^{39}Ar diffusion in samples for which comparably precise data were obtained for both isotopes (ECCa, OREGp, DCp, SURTp, HMS-2p, TROCp, GRAp, PR-92p). The black, dashed line is the 1:1-line. No systematic differences are apparent.

magnitude smaller than the 100 - 1000 μm domain size of the samples analyzed herein. Thus our results are not directly comparable. Because considerable inter-sample variability exists, we suggest that there is no broadly applicable set of diffusion parameters that can be utilized in thermal modeling. It appears that sample specific data are required. Diffusion experiments conducted on oriented cleavage flakes (Figs. 3.2 and 4.1) yielded apparent diffusion parameters (Table 4.1) that span the range in values shown in Figure 8.3. As such, using the diffusion parameters of more than one of these samples whose compositions are similar to that of an unknown represents a reasonable approach to propagating uncertainties on argon diffusivities into thermal models. Argon diffusion parameters in these samples are constrained by the following Arrhenius relationships:

Labradorite ($An_{59.6}Ab_{39.6}Or_{0.8}$): $\ln\left(D\left[\mathrm{m^2/s}\right]\right) = \left(-17.1 \pm 0.5\right) e^{\left(\frac{-\left(174.5 \pm 3.6\right)\mathrm{kJ/mole}}{RT}\right)}$, Eq. (4)

Labradorite ($An_{63.9}Ab_{35.4}Or_{0.7}$): $\ln\left(D\left[\mathrm{m^2/s}\right]\right) = \left(-8.1 \pm 1.9\right) e^{\left(\frac{-\left(224.0 \pm 12.5\right)\mathrm{kJ/mole}}{RT}\right)}$, Eq. (5)

Anorthoclase ($An_{10.8}Ab_{71.8}Or_{17.4}$): $\ln\left(D\left[\mathrm{m^2/s}\right]\right) = \left(0.8 \pm 1.7\right) e^{\left(\frac{-\left(286.0 \pm 11.5\right)\mathrm{kJ/mole}}{RT}\right)}$, Eq. (6)

Orthoclase ($An_{0.0}Ab_{3.0}Or_{97.0}$): $\ln\left(D\left[\mathrm{m^2/s}\right]\right) = \left(-10.0 \pm 0.2\right) e^{\left(\frac{-\left(217.7 \pm 1.9\right)\mathrm{kJ/mole}}{RT}\right)}$, Eq. (7)

Cryptoperthite ($An_{0.2}Ab_{5.6}Or_{94.6}$): $\ln\left(D\left[\mathrm{m^2/s}\right]\right) = \left(-0.8 \pm 0.4\right) e^{\left(\frac{-\left(272.8 \pm 3.4\right)\mathrm{kJ/mole}}{RT}\right)}$. Eq. (8)

8.3. Atomistic description of diffusion

Over the years, several models based on ionic porosity (the fraction of unit cell volume that is not occupied by ions) have been proposed to explain relative differences in elemental diffusivity between various mineral phases (e.g., Dowty, 1980; Fortier and Giletti, 1989; Dahl, 1994; Zhao and Zheng, 2007). In general, these models contend that diffusivity at a given temperature is inversely proportional to total ionic porosity (Z_T) or anionic porosity (Z_A), both of which vary with temperature. If we assume that diffusivity is proportional to total ionic porosity, then Ar should diffuse more slowly in sanidine (Z_T = 55.6)[3] than in anorthite (Z_T = 59.6) or albite (Z_T = 59.7), wherein it should diffuse at an approximately equivalent rate. Such a relationship is not observed, as Na- and Ca-rich feldspars have the highest and lowest closure temperatures, respectively, with K-rich feldspars having

[3] Z_T represents the total ionic porosity and add a few notes here on how it is calculated.

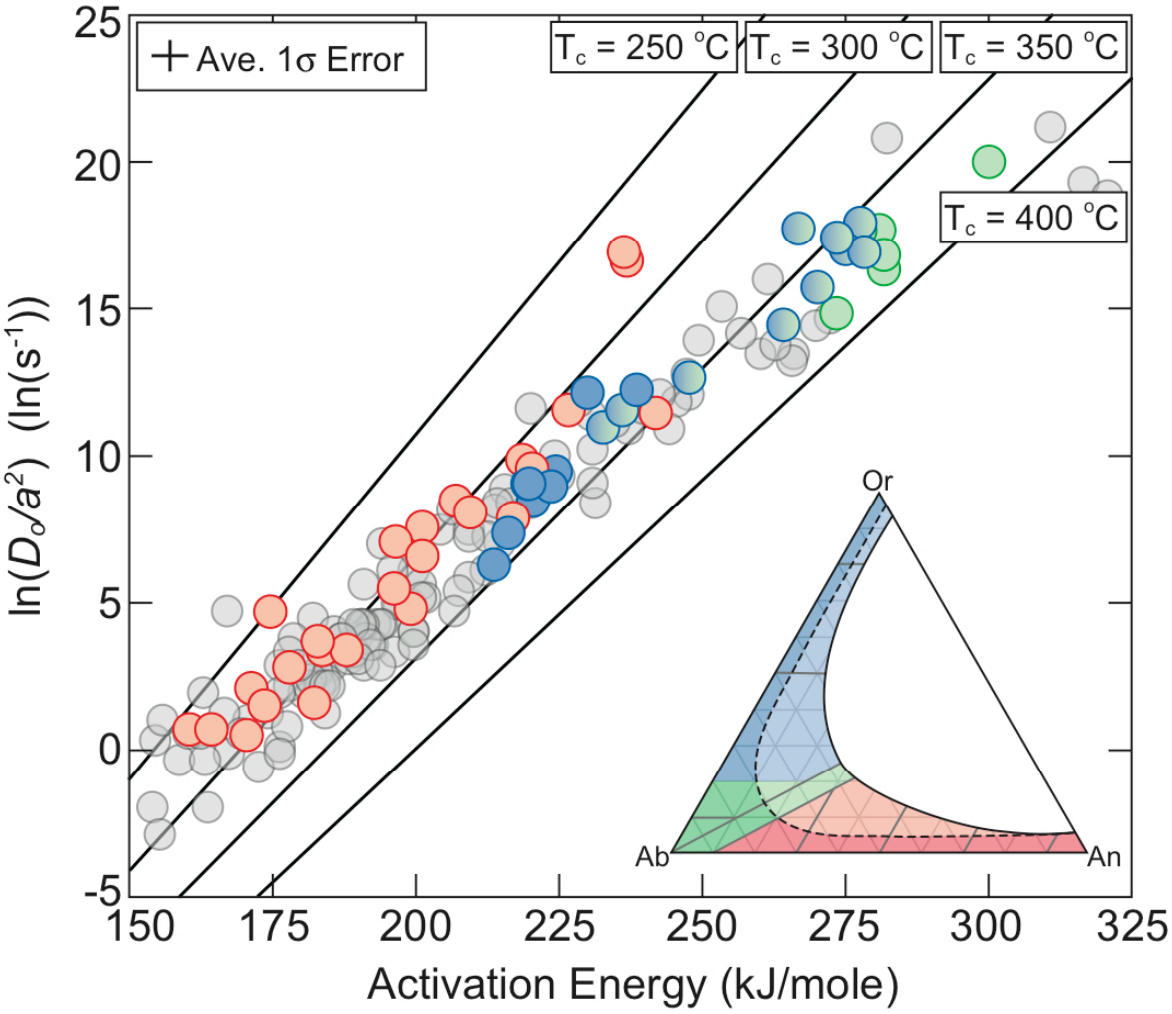

Figure 8.3: Summary of kinetic parameters for Ar diffusion in Ca-rich (red), Na-rich (green), K-rich (blue), and perthitic (blue-green gradient) feldspars. Lines correspond to closure temperatures between 250 and 400 °C, calculated assuming spherical geometry and a 10 °C/Ma cooling rate. Apparent $\ln(D_o/a^2)$ values obtained from Arrhenius plots that were calculated assuming infinite sheet geometry (i.e., from cleavage flakes) were corrected by 2.2 natural log units following Huber et al. (2011), such that the inferred closure temperatures are comparable to those obtained from equant grains (see Table 8.1). The results of Lovera et al. (1997) and Forster and Lister (2010), also corrected according to Huber et al. (2011), are shown in gray.

intermediate closure temperatures (Figs. 8.1 and 8.3). Likewise, Fortier and Giletti (1989) observed slower oxygen diffusion in albite than in K-feldspar than in anorthite at 500 and 700 °C. The total ionic porosity model presumably fails because interatomic potentials and bond dimensions and angles (i.e., crystal structure) are not considered. Ca- and Na-rich feldspars have similar triclinic structures and nearly equivalent ionic porosities, yet they yield different closure temperatures. The Ar-Na Lennard-Jones repulsive forces are significantly greater than Ar-Ca repulsive forces at a given distance (Fig. 5.4), thus explaining the lower mobility of Ar in Na-rich feldspars. Although Ar-K repulsive forces at a given distance are even greater than

Ar-Ca and Ar-Na repulsive forces, the structure (i.e., bond lengths and angles) of K-rich feldspars comprises interstitial lattice configurations that are not comparable to those of Ca- and Na-rich feldspars. These structural differences appear to obscure the importance of cationic interatomic potential variations. To illustrate this point, consider Ar diffusion in the triclinic and monoclinic forms of ECC anorthoclase. The Arrhenius arrays associated with these structural polymorphs are linear, sub-parallel, and offset vertically by approximately 2 natural log units (Fig. 5.8). The significant differences in diffusivity highlight the importance of bond lengths and angles in determining noble gas mobility, as ionic porosity varies little and composition remains unchanged across the structural transition.

8.4. The equivalence of barometric and thermal expansion/compression

Pressure-dependent reductions in Ar diffusivity have been observed in a variety of minerals, including biotite (Harrison et al., 1985), phlogopite (Giletti and Anderson, 1975), and muscovite (Harrison et al., 2009). Such reductions in diffusivity are attributed to the extra work required to migrate through a compressed medium (e.g. Harrison et al., 1985). A modified version of the Arrhenius equation is used to account for the pressure-dependence of diffusivity (e.g., McDougall and Harrison, 1999), given by

$$D = D_o e^{\left(\frac{E_a + PV}{RT}\right)}, \qquad \text{Eq. (9)}$$

where V is the activation volume (in cm^3/mol) and P is pressure. Historically (e.g., Harrison et al., 1985; Carrol and Stolper, 1991), the activation volume has been inferred from isothermal differences in diffusivity at two or more different pressures. The affect of increasing pressure, by implication, is assumed to linearly increase the potential energy barriers to diffusion (Eq. 9).

In the absence of the incorporation of enhanced concentrations of gaseous species at high pressures (which could slow diffusivity due to strong gas-gas Lennard-Jones repulsions; Du et al., 2008), pressure-dependent reductions in diffusivity can, as suggested above, be attributed to compression of the bond dimensions and angles, which in turn increases the potential energy barriers to diffusion. Because such potential energy barriers are exponentially sensitive to interatomic distances (Fig. 5.4), a linear relationship between pressure and apparent activation volume at a given temperature is not predicted by molecular dynamics considerations. Moreover, the relationship between pressure and activation volume should vary with temperature, as thermal expansion alters the unit cell dimensions and angles upon which barometric compression acts. Thus a modified Arrhenius equation describing the pressure- and temperature-dependence of diffusivity could be used, given by the following:

$$D = D_o e^{\left(\frac{U_{ref} + V(P,T)}{RT}\right)}, \qquad \text{Eq. (10)}$$

where U_{ref} is the potential energy barrier to diffusion at a reference temperature and $V(P,T)$

describes the pressure and temperature dependent deviations in diffusivity from the reference Arrhenius relationship due to thermal or barometric expansion/compression (i.e., due to changes in the interstitial configurations of lattice atoms; see Eqs. (1-3), Fig. 5.5, and related discussions).

Table 8.1: Summary of diffusion parameters

				Composition				E_a ± 1σ	$\ln(D_o/a^2)$ ± 1σ	T_c ± 1σ
Sample	**Locality**	**Phase**	**Symmetry**	**An**	**Ab**	**Or**	**Geom.**	**(kJ/mole)**	**($\ln(s^{-1})$)**	**(°C)**
BMk-1	Benson Mines	Orthoclase	*C2m*	0.0	3.0	97.0	IS	223.5 ± 3.3	11.1 ± 0.4	334.0 ± 4.0
BMk-2	Benson Mines	Orthoclase	*C2m*	0.0	3.0	97.0	IS	216.0 ± 3.4	9.5 ± 0.4	335.1 ± 3.9
BMk-3	Benson Mines	Orthoclase	*C2m*	0.0	3.0	97.0	IS	213.5 ± 3.3	8.4 ± 0.4	343.4 ± 3.6
BMk-4	Benson Mines	Orthoclase	*C2m*	0.0	3.0	97.0	IS	229.9 ± 3.0	11.1 ± 0.3	310.6 ± 4.4
BMk-5	Benson Mines	Orthoclase	*C2m*	0.0	3.0	97.0	S	219.7 ± 3.2	9.0 ± 0.4	322.7 ± 3.3
XTALk-1	Ecstall Pluton	Orthoclase	*C2m/C1*	0.1	11.3	88.6	S	238.4 ± 8.3	12.2 ± 1.0	330.6 ± 8.4
MADk-1	Itrongay, Madagascar	Cyptoperthite	*C2m/C1*	0.2	5.6	94.6	IS	270.0 ± 7.9	17.9 ± 1.0	363.9 ± 6.1
MADk-2	Itrongay, Madagascar	Cyptoperthite	*C2m/C1*	0.2	5.6	94.6	IS	264.1 ± 7.5	16.6 ± 1.0	365.7 ± 5.3
MADk-3	Itrongay, Madagascar	Cyptoperthite	*C2m/C1*	0.2	5.6	94.6	IS	277.5 ± 9.1	20.1 ± 1.2	355.1 ± 6.9
MADk-4	Itrongay, Madagascar	Cyptoperthite	*C2m/C1*	0.2	5.6	94.6	IS	275.0 ± 6.2	19.2 ± 0.8	359.9 ± 5.1
MADk-5	Itrongay, Madagascar	Cyptoperthite	*C2m/C1*	0.2	5.6	94.6	IS	278.2 ± 7.9	19.1 ± 1.0	368.4 ± 5.6
MADk-6	Itrongay, Madagascar	Cyptoperthite	*C2m/C1*	0.2	5.6	94.6	IS	266.7 ± 7.9	17.7 ± 1.0	333.3 ± 6.7
MADk-7	Itrongay, Madagascar	Cyptoperthite	*C2m/C1*	0.2	5.6	94.6	S	273.4 ± 7.9	17.4 ± 1.0	351.7 ± 6.3
BV-8k-1	Bushveld Complex	Perthite	*C2m/C1*	0.8	22.6	76.6	S	232.6 ± 12.0	10.9 ± 1.7	332.1 ± 8.9
BV-8k-2	Bushveld Complex	Perthite	*C2m/C1*	0.8	22.6	76.6	S	247.6 ± 12.9	12.6 ± 1.8	348.4 ± 8.6
BV-8k-3	Bushveld Complex	Perthite	*C2m/C1*	0.8	22.6	76.6	S	236.0 ± 16.2	11.5 ± 2.2	333.1 ± 12.9
FCs-1	Fish Canyon Tuff	Sanidine	*C2m*	1.0	27.0	72.0	S	224.3 ± 4.1	9.4 ± 0.5	329.7 ± 4.3
FCs-2	Fish Canyon Tuff	Sanidine	*C2m*	1.0	27.0	72.0	S	220.4 ± 4.6	8.4 ± 0.5	332.3 ± 5.7
GSs-1	Gulf of Salerno	Sanidine	*C2m*	3.7	30.5	65.8	S	219.4 ± 2.5	9.0 ± 0.3	321.8 ± 3.2
ECCa-1	Easy Chair Crater	Anorthoclase	*C1*	10.8	71.8	17.4	IS	278.3 ± 19.5	19.9 ± 2.8	359.3 ± 10.7
ECCa-2	Easy Chair Crater	Anorthoclase	*C1*	10.8	71.8	17.4	IS	281.7 ± 20.0	19.0 ± 2.9	377.4 ± 9.6
ECCa-3	Easy Chair Crater	Anorthoclase	*C1*	10.8	71.8	17.4	IS	300.0 ± 21.2	22.2 ± 3.1	380.1 ± 9.9
ECCa-4	Easy Chair Crater	Anorthoclase	*C1*	10.8	71.8	17.4	S	280.0 ± 30.8	17.6 ± 4.4	364.1 ± 15.9
GRAp-1	ET (GRA 06128)	Albite/Olig.	*C1*	14.1	84.1	1.9	S	209.4 ± 5.8	8.0 ± 0.6	307.7 ± 8.3
ML-15p-1	Mono Lake	Oligoclase	*C1*	19.6	74.2	6.2	S	273.3 ± 12.9	14.8 ± 1.3	382.7 ± 13.3
ML-15p-2	Mono Lake	Oligoclase	*C1*	19.6	74.2	6.2	S	281.7 ± 13.1	16.3 ± 1.2	383.4 ± 14.6
XTALp-1	Ecstall Pluton	Oligoclase	*C1*	20.8	77.7	1.5	S	201.1 ± 4.1	7.5 ± 0.4	291.4 ± 6.6
FCp-1	Fish Canyon Tuff	Olig./Andesine	*C1*	29.8	61.7	4.5	S	218.5 ± 21.2	9.8 ± 2.7	309.4 ± 20.6
PR-92p-1	Paraná-Etendeka LIP	Andesine	*C1*	41.1	54.6	4.3	S	206.9 ± 16.6	8.4 ± 2.5	296.0 ± 13.0
NCp-1	Nain Complex	Labradorite	e_1/e_2	49.4	47.9	2.7	S	171.2 ± 12.0	2.0 ± 1.8	276.6 ± 11.4
NCp-2	Nain Complex	Labradorite	e_1/e_2	49.4	47.9	2.7	S	174.5 ± 7.9	4.6 ± 1.2	252.3 ± 7.7
HMS-2p-1	Klamath Mtns.	Labradorite	*C1*	52.8	44.2	3.0	S	226.6 ± 6.2	11.5 ± 0.8	309.4 ± 5.6
SURTp-1	Surtsey, Iceland	Labradorite	*I1*	59.6	39.6	0.8	IS	182.2 ± 7.1	3.7 ± 0.9	318.6 ± 8.4
SURTp-2	Surtsey, Iceland	Labradorite	*I1*	59.6	39.6	0.8	IS	170.4 ± 5.8	2.6 ± 0.8	297.3 ± 6.7
SURTp-3	Surtsey, Iceland	Labradorite	*I1*	59.6	39.6	0.8	IS	173.5 ± 5.8	3.6 ± 0.8	292.4 ± 6.6
SURTp-4	Surtsey, Iceland	Labradorite	*I1*	59.6	39.6	0.8	IS	199.0 ± 6.7	6.9 ± 0.9	322.8 ± 6.2
SURTp-5	Surtsey, Iceland	Labradorite	*I1*	59.6	39.6	0.8	IS	164.3 ± 5.8	2.8 ± 0.8	274.4 ± 7.6
OREGp-1	Plush, Oregon	Labradorite	*I1*	63.9	35.4	0.7	IS	220.2 ± 17.9	11.7 ± 2.6	317.5 ± 13.5
OREGp-2	Plush, Oregon	Labradorite	*I1*	63.9	35.4	0.7	IS	241.8 ± 26.6	13.6 ± 4.0	349.0 ± 15.0
OREGp-3	Plush, Oregon	Labradorite	*I1*	63.9	35.4	0.7	IS	216.9 ± 24.1	10.0 ± 3.6	330.6 ± 16.4
OREGp-4	Plush, Oregon	Labradorite	*I1*	63.9	35.4	0.7	IS	201.1 ± 10.0	6.5 ± 1.4	304.3 ± 9.7
BV-8p-1	Bushveld Complex	Labradorite	$e_1/P1$	67.4	31.3	1.3	S	183.6 ± 9.5	3.3 ± 1.4	296.8 ± 35.2
BV-8p-2	Bushveld Complex	Labradorite	$e_1/P1$	67.4	31.3	1.3	S	187.8 ± 18.7	3.3 ± 2.5	309.4 ± 19.6
BV-8p-3	Bushveld Complex	Labradorite	$e_1/P1$	67.4	31.3	1.3	S	160.4 ± 8.3	0.6 ± 1.2	261.7 ± 10.3
DCp-1	Duluth Complex	Bytownite	$e_1/P1$	74.7	24.9	0.4	S	177.8 ± 18.3	2.7 ± 2.6	287.5 ± 18.5
DCp-2	Duluth Complex	Bytownite	$e_1/P1$	74.7	24.9	0.4	S	182.8 ± 11.3	3.6 ± 2.7	290.1 ± 3.1
DCp-3	Duluth Complex	Bytownite	$e_1/P1$	74.7	24.9	0.4	S	196.4 ± 13.7	7.0 ± 2.0	284.8 ± 12.2
JAPp-1	Miyake, Japan	Anorthite	*T*	96.2	3.7	0.1	S	236.8 ± 5.8	16.6 ± 0.7	277.5 ± 5.5
JAPp-2	Miyake, Japan	Anorthite	*T*	96.2	3.7	0.1	S	236.2 ± 7.5	16.9 ± 0.9	273.2 ± 7.8
TROCp-1	Lunar (76535)	Anorthite	*P1*	96.2	3.5	0.3	S	196.1 ± 20.4	5.4 ± 2.9	304.6 ± 18.4

Symmetry groups and phase names based on Figure 3.

IS is infinite sheet geometry (used for cleavage flakes) and S is spherical geometry (used for equant grains).

T_c calculated assuming spherical geometry and a 10 °C/Ma cooling rate.

Cleavage flake $\ln(D_o/a^2)$ values were corrected by 2.2 natural log units (Huber et al., 2011) for T_c calculations such that IS and S results are comparable.

T_c's would be approximately 5 °C lower if calculated using equations for IS geometry.

Sanidine, cryptoperthite, perthite, orthoclase, and anorthoclase results based on ^{39}Ar data.

Albite, oligoclase, andesine, labradorite, bytownite, and anorthite results based on ^{37}Ar data.

In some crystal structures (e.g., albite; Brown et al., 1984), pressure and temperature are analogous variables (i.e., increasing/decreasing pressure and decreasing/increasing temperature have equivalent affects on the crystal lattice). Thus a given unit cell configuration can be achieved at different temperatures by varying the pressure in accordance with the equation of state. By implication the true, bulk crystal potential energy barrier to diffusion associated with a given unit cell configuration (U_{ref}) can be inferred from a variable-pressure Arrhenius plot. It follows that the true potential energy barriers to diffusion in a given mineral at geologically relevant temperatures, which are generally not accessible by laboratory diffusion experiments, can be gleaned from data obtained from higher temperature and pressure extractions (i.e., one can exploit the enhanced diffusivity that occurs at high-T by increasing pressure). Such an approach could be useful in constraining the importance of geologically relevant polymorphic structural transitions on apparent diffusion parameters. For example, one could study the diffusion consequences of the *P1-T* structural transition in anorthite at typical laboratory temperatures (>400 ºC) if high pressures were employed, in effect countering the thermal expansion.

Chapter 9.

Conclusions

9.1. Concluding remarks

We conducted diffusion experiments on feldspars with diverse compositions, structural states, and microstructural characteristics to constrain the physical significance of the diffusion domain, the isotropy of diffusion, and the importance of composition and structural state in determining diffusivity. We found that unaltered, uncleaved feldspar crystals diffuse at the grain scale, whereas feldspars containing hydrothermal alteration and/or incoherent sub-grain intergrowths comprise multiple diffusion domains. Coherent lamellar intergrowths (e.g., film perthite and *e*-plagioclase) represent complex interfaces within diffusion domains, but do not appear to provide fast pathways for noble gas diffusion. Diffusive anisotropy was not resolvable within the precision limits of our methodology (approximately of factor of 2) at temperatures below ~900 °C. It follows that the appropriate geometry for diffusion modeling is one that most closely resembles the physical grain dimensions, or the shape of sub-grain domains. Apparent diffusion parameters appear intimately related to composition and structural state. As such, there is no broadly applicable set of diffusion parameters that can be utilized in thermal modeling. Sample-specific data are required. In general, Na-, K-, and Ca-rich feldspars yield the highest, intermediate, and lowest activation energies and closure temperatures, respectively. Apparent closure temperatures for 0.1-1 millimeter grains are between ~200 and 400 °C, assuming spherical geometry and 10 °C/Ma cooling rate, and activation energies vary between 170 and 285 kJ/mole.

Noble gas diffusion in feldspars appears to proceed primarily through metal-oxygen and oxygen-oxygen interstitial lattice configurations, vacancies, and extended linear and planar defects. Potential energy barriers to diffusion associated with interstitial configurations of lattice atoms are exponentially sensitive to the distances between diffusing noble gas atoms and the metal-oxygen interstitial constituents, and therefore exhibit significant variability throughout an incremental degassing experiment due to changes in unit cell dimensions and angles that occur when feldspars are heated. Temperature intervals over which linearity is observed on Arrhenius plots appear to coincide with intervals over which a given feldspar structure is stable. Deviations from linearity, when not attributable to multiple diffusion domains, appear to coincide with structural transitions brought about by heating, such as changes in unit cell angles and cation coordination.

Knowledge of the stability of the diffusion domain, both over geologic time and during laboratory heating experiments, and an understanding of whether or not diffusivities at geologically relevant temperatures differ significantly from down-temperature extrapolations

of laboratory-derived diffusion parameters are critical to obtaining accurate thermal histories. When structural or thermal expansion regime changes occur below the temperatures at which laboratory diffusion experiments are conducted (e.g., *P1*-anorthite), corrections must be applied to extrapolated, low-T diffusion coefficients. Likewise, corrections must be made to apparent domain distribution parameters inferred from Arrhenius plots obtained by heating samples that comprise multiple diffusion domains and undergo structural transitions (e.g., perthite), both of which contribute to non-linearity. Routine examination of samples using a petrographic microscope, electron microprobe, or SEM is generally sufficient to assess the nature of the diffusion domain and the suitability of a given sample for thermal modeling (i.e., to establish the temporal relationship between the formation of alteration surfaces, fractures, and other domain-defining features and the thermal history of interest).

It is to be hoped that this work will stimulate further collaboration between mineralogists and thermochronologists. Detailed "at-temperature" measurements of M-O and O-O bond lengths and angles, coupled with noble gas diffusion experiments, would shed new light on the relationship between structural changes and Arrhenius non-linearity. Moreover, the simultaneous analysis of multiple noble gas species released from individual grain fragments would provide invaluable insights into the importance of thermal expansion (i.e., changing interstitial bond lengths and angles) in determining apparent diffusion parameters. Such experiments may hold the key to a better atomistic understanding of noble gas diffusion in rocks and minerals.

References

Arnaud, N.O., Kelley, S.P., 1997. Argon behaviour in gem-quality orthoclase from Madagascar: Experiments and some consequences for $^{40}Ar/^{39}Ar$ geochronology. *Geochimica et Cosmochimica Acta* 61, 3227-3255.

Bachmann, O., Dungan, M.A., Lipman, P.W., 2002. The Fish Canyon magma body, San Juan volcanic field, Colorado: rejuvenation and eruption of an upper-crustal batholith. *Journal of Petrology* 43, 1469-1503.

Barth, T.F.W., 1965. On the constitution of the alkali feldspars. *Mineralogy and Petrology* 10, 14-33.

Bauer, M., Klee, W.E., 1993. Induced ferrielectricity in chlorapatite. *Zeitschrift fur Kristallographie* 206, 15-24.

Baxter, E.F., 2010. Diffusion of noble gases in minerals. *Reviews in Mineralogy and Geochemistry* 72, 509-557.

Benna, P., Bruno, E., 2001. Single-crystal *in-situ* high-temperature structural investigation on strontium feldspar. *American Mineralogist* 86, 690-696.

Benna, P., Tribaudino, M., Bruno, E., 2000. I1-I2/c ferroelastic phase transition in the $Ca_{0.2}Pb_{0.8}Al_2Si_2O_8$ feldspar as a function of temperature. *Mineralogical Magazine* 64, 285-290.

Berger, G.W., York, D., 1981. Geothermometry from dating experiments. *Geochimica et Cosmochimica Acta* 45, 795-811.

Bose, P.P., Mittal, R., Chaplot, S.L., Patwe, S.J., Achary, S.N., Tyagi, A.K., 2010. Thermal expansion in zircon and scheelite phases of ThGeO by x-ray diffraction and lattice dynamics. *AIP Conference Proceedings* 1313, 361-363.

Boven, A., Pasteels, P., Kelley, S.P., Punzalan, L., Bingen, B., Demaiffe, D., 2001. $^{40}Ar/^{39}Ar$ study of plagioclases from the Rogaland anorthosite complex (SW Norway); an attempt to understand argon ages in plutonic plagioclase. *Chemical Geology* 176, 105-135.

Bown, M.G., Gay, P., 1969. The effect of heat treatment on the diffraction patterns of intermediate plagioclases. *Zeitschrift fur Kristallographie* 129, 451-457.

Braun, J., 2005. Quantitative constraints on the rate of landform evolution derived from low-temperature thermochronology. *Reviews in Mineralogy and Geochemistry* 58, 351-374.

Brown, W.L., 1984. Feldspars and feldspathoids: Structures, properties, and occurences. Springer.

Brown, W.L., Openshaw, R.E., McMillan, P.F., Henderson, M.B., 1984. A review of the expansion behavior of alkali feldspars: coupled variations in cell parameters and possible phase transitions. *American Mineralogist* 69, 1058-1071.

Brownlee, S.J., Renne, P.R., 2010. Thermal history of the Ecstall pluton from $^{40}Ar/^{39}Ar$ geochronology and thermal modeling. *Geochimica et Cosmochimica Acta* 74, 4375-4391.

Brunet, F., Allan, D.R., Redfern, S.A.T., Angel, R.J., Miletich, R., Reichmann, H.J., Sergent, J., Hanfland, M., 1999. Compressibility and thermal expansivity of synthetic apatites, $Ca_5(PO_4)_3X$ with X = OH, F and Cl. *European Journal of Mineralogy* 11, 1023-1035.

Carpenter, M.A., McConnell, J.D.C., Navrotsky, A., 1985. Enthalpies of ordering in the plagioclase feldspar solid solution. *Geochimica et Cosmochimica Acta* 49, 947-966.

Carroll, M.R., Stolper, E.M., 1991. Argon solubility and diffusion in silica glass: Implications for the solution behavior of molecular gases. *Geochimica et Cosmochimica Acta* 55, 211-225.

Cashman, K.V., 1993. Relationship between plagioclase crystallization and cooling rate in basaltic melts. *Contributions to Mineralogy and Petrology* 113, 126-142.

Cassata, W.S., 2011. An isochron approach to ^{21}Ne cosmic ray exposure dating by activation with deuteron-deuteron fusion neutrons. *Chemical Geology* 284, 21-25.

Cassata, W.S., Renne, P.R., Shuster, D.L., 2009. Argon diffusion in plagioclase and implications for thermochronometry: A case study from the Bushveld Complex, South Africa. *Geochimica et Cosmochimica Acta* 73, 6600-6612.

Cassata, W.S., Shuster, D.L., Renne, P.R., Weiss, B.P., 2010. Evidence for shock heating and constraints on Martian surface temperatures revealed by $^{40}Ar/^{39}Ar$ thermochronometry of Martian meteorites. *Geochimica et Cosmochimica Acta* 74, 6900-6920.

Cassata, W., Singer, B., Liddicoat, J., Coe, R., 2010. Reconciling discrepant chronologies for the geomagnetic excursion in the Mono Basin, California: Insights from new $^{40}Ar/^{39}Ar$ dating experiments and a revised relative paleointensity correlation. *Quaternary Geochronology* 5, 533-543.

Chaplot, S.L., Mittal, R., Busetto, E., Lausi, A., 2002. Thermal expansion in zircon and almandine: Synchrotron x-ray diffraction and lattice dynamical study. *Physical Review B* 66, 064302.

Cherniak, D.J., 2010. Cation diffusion in feldspars. *Reviews in Mineralogy and Geochemistry* 72, 691-733.

Chon, C.M., Kim, S., Moon, H.S., 2003. Crystal structures of biotite at high temperatures and of heat-treated biotite using neutron powder diffraction. *Clays and Clay Minerals* 51, 519-

528.

Coombs, D.S., 1954. Ferriferous orthoclase from Madagascar. *Mineralogical Magazine* 30, 409-427.

Cosca, M., Stunitz, H., Bourgeix, A.L., Lee, J.P., 2011. $^{40}Ar^*$ loss in experimentally deformed muscovite and biotite with implications for $^{40}Ar/^{39}Ar$ geochronology of naturally deformed rocks. *Geochimica et Cosmochimica Acta* 75, 7759–7778.

Crank, J., 1975. The mathematics of diffusion. 2nd. *Ed., Clarendon Press, Oxford*.

Croarkin, M.C., Guthrie, W.F., Burns, G.W., Kaeser, M., Strouse, G.F., 1993. Temperature-electromotive force reference functions and tables for the letter-designated thermocouple types based on the ITS-90. *National Institute of Standards and Technology Monograph* 175, 630 pp.

Dahl, P.S., 1994. "Ionic porosity" as a predictor of diffusion parameters in thermochronometric minerals: evidence and tectonic implications. *Mineralogical Magazine* 58, 205-206.

Dodson, M.H., 1973. Closure temperature in cooling, geochronological, and petrological systems. *Contributions to Mineralogy and Petrology* 40, 259-274.

Dove, M.T., 2001. Computer simulations of solid solutions. *Solid Solutions in Silicate and Oxide Systems of Geological Importance. EMU Notes in Mineralogy* 3, 225-249.

Dowty, E., 1980. Crystal-chemical factors affecting the mobility of ions in minerals. *American Mineralogist* 65, 174-182.

Du, Z., Allan, N.L., Blundy, J.D., Purton, J.A., Brooker, R.A., 2008. Atomistic simulation of the mechanisms of noble gas incorporation in minerals. *Geochimica et Cosmochimica Acta* 72, 554-573.

Ehlers, T.A., 2005. Crustal thermal processes and the interpretation of thermochronometer data. *Reviews in Mineralogy and Geochemistry* 58, 315-350.

Ehlers, T.A., Chaudhri, T., Kumar, S., Fuller, C.W., Willett, S.D., Ketcham, R.A., Brandon, M.T., Belton, D.X., Kohn, B.P., Gleadow, A.J.W., 2005. Computational tools for low-temperature thermochronometer interpretation. *Reviews in Mineralogy and Geochemistry* 58, 589-622.

Farley, K.A., 2000. Helium diffusion from apatite: General behavior as illustrated by Durango fluorapatite. *Journal of Geophysical Research* 105, 2903-2914.

Fechtig, H., Kalbitzer, S., 1966. The diffusion of argon in potassium-bearing solids, in:

Fechtig, H., Kalbitzer, S., Schaeffer, O., Zahringer, J. (Eds.), Potassium-argon dating. Springer Verlag, pp. 68-106.

Foit, F.F., Peacor, D.R., 1967. High temperature diffraction data on selected reflections of an andesine and anorthite. *Zeitschrift fur Kristallographie* 125, 147-156.

Foit, F.F., Peacor, D.R., 1973. The anorthite crystal structure at 410 and 830 °C. *American Mineralogist* 58, 665-675.

Foland, K.A., 1974. Ar^{40} diffusion in homogenous orthoclase and an interpretation of Ar diffusion in K-feldspars. *Geochimica et Cosmochimica Acta* 38, 151-166.

Forster, M.A., Lister, G.S., 2010. Argon enters the retentive zone: reassessment of diffusion parameters for K-feldspar in the South Cyclades Shear Zone, Ios, Greece. *Geological Society, London, Special Publications* 332, 17-34.

Fortier, S.M., Giletti, B.J., 1989. An empirical model for predicting diffusion coefficients in silicate minerals. *Science* 245, 1481-1484.

Gaber, L.J., Foland, K.A., Corbato, C.E., 1988. On the significance of argon release from biotite and amphibole during $^{40}Ar/^{39}Ar$ vacuum heating. *Geochimica et Cosmochimica Acta* 52, 2457-2465.

Garrick-Bethell, I., Weiss, B.P., Shuster, D.L., Buz, J., 2009. Early lunar magnetism. *Science* 323, 356-359.

Giletti, B.J., Anderson, T.F., 1975. Studies in diffusion, II. Oxygen in phlogopite mica. *Earth and Planetary Science Letters* 28, 225-233.

Glicksman, M.E., 2000. Diffusion in solids: field theory, solid-state principles, and applications. Wiley New York.

Grundy, H.D., Brown, W.L., 1974. A high-temperature X-ray study of low and high plagioclase feldspars, in: MacKenzie, W.S., Brown, W.L. (Eds.), The Feldspars. Manchester University Press, Manchester, UK, pp. 162-173.

Harlow, G.E., 1982. The anorthoclase structures: the effects of temperature and composition. *American Mineralogist* 67, 975-996.

Harrison, T.M., Celerier, J., Aikman, A.B., Hermann, J., Heizler, M.T., 2009. Diffusion of ^{40}Ar in muscovite. *Geochimica et Cosmochimica Acta* 73, 1039-1051.

Harrison, T.M., Duncan, I., McDougall, I., 1985. Diffusion of ^{40}Ar in biotite: temperature, pressure and compositional effects. *Geochimica et Cosmochimica Acta* 49, 2461-2468.

Harrison, T.M., Heizler, M.T., McKeegan, K.D., Schmitt, A.K., 2010. *In-situ* ^{40}K-^{40}Ca 'double-plus' SIMS dating resolves Klokken feldspar ^{40}K-^{40}Ar paradox. *Earth and Planetary Science Letters* 299, 426-433.

Harrison, T.M., Lovera, O.M., Matthew, T.H., 1991. ^{40}Ar/^{39}Ar results for alkali feldspars containing diffusion domains with differing activation energy. *Geochimica et Cosmochimica Acta* 55, 1435-1448.

Harrison, T.M., McDougall, I., 1981. Excess ^{40}Ar in metamorphic rocks from Broken Hill, New South Wales: implications for ^{40}Ar/^{39}Ar age spectra and the thermal history of the region. *Earth and Planetary Science Letters* 55, 123-149.

Harrison, T.M., Zeitler, P.K., 2005. Fundamentals of noble gas thermochronometry. *Reviews in Mineralogy and Geochemistry* 58, 123-149.

Heizler, M.T., Harrison, T.M., 1998. The thermal history of the New York basement determined from ^{40}Ar/^{39}Ar K-feldspar studies. *Journal of Geophysical Research* 103, 29795-29814.

Heizler, M.T., Parsons, I., Sanders, R.E., Heizler, L.L., 2008. K-feldspar microtexture and argon transport, Joint Meeting of The Geological Society of America, Soil Science Society of America, American Society of Agronomy, Crop Science Society of America, Gulf Coast Association of Geological Societies with the Gulf Coast Chapter of SEPM.

Heizler, M.T., Parsons, I., Sanders, R.E., Heizler, L.L., Karlstrom, K.E., 2007. K-Feldspar ^{40}Ar/^{39}Ar thermochronology of western USA precambrian lithosphere: Improved understandings of systematics towards more accurate geological models, GSA Annual Meeting.

Hitmi, N., Lacabanne, C., Young, R.A., 1984. TSC study of electric dipole relaxations in chlorapatite. *Journal of Physics and Chemistry of Solids* 45, 701-708.

Hitmi, N., LaCabanne, C., Young, R.A., 1986. OH- dipole reorientability in hydroxyapatites: Effect of tunnel size. *Journal of Physics and Chemistry of Solids* 47, 533-546.

Hitmi, N., LaCabanne, C., Young, R.A., 1988. OH- reorientability in hydroxyapatites: Effect of F and Cl. *Journal of Physics and Chemistry of Solids* 49, 541-550.

Hopkins, R.H., Damon, D.H., Piotrowski, P., Walker, M.S., Uphoff, J.H., 1971. Thermal properties of synthetic fluorapatite crystals. *Journal of Applied Physics* 42, 272-275.

Hovis, G.L., 1980. Angular relations of alkali feldspar series and the triclinic-monoclinic displacive transformation. *American Mineralogist* 65, 770-778.

Hovis, G.L., Brennan, S., Keohane, M., Crelling, J., 1999. High-temperature X-ray

investigation of sandine - analbite crystalline solutions: Thermal expansion, phase transitions, and volumes of mixing. *The Canadian Mineralogist* 37, 701-709.

Hovis, G.L., Medford, A., Conlon, M., Tether, A., Romanoski, A., 2010. Principles of thermal expansion in the feldspar system. *American Mineralogist* 95, 1060-1068.

Huber, C., Cassata, W.S., Renne, P.R., 2011. A lattice Boltzmann model for noble gas diffusion in solids: The importance of domain shape and diffusive anisotropy and implications for thermochronometry. *Geochimica et Cosmochimica Acta* 75, 2170–2186.

Jena, H., Asuvathraman, R., Govindan Kutty, K.V., 2011. Thermal expansion and phase stability investigations on Cs-substituted nanocrystalline calcium hydroxyapatites. *Journal of Materials Engineering and Performance* 20, 108-113.

Karlstrom, K.E., Heizler, M., Quigley, M.C., 2010. Structure and $^{40}Ar/^{39}Ar$ K-feldspar thermal history of the Gold Butte block: Reevaluation of the tilted crustal section model. *Geological Society of America Special Papers* 463, 331-352.

Knyazev, A.V., Chernorukov, N.G., Bulanov, E.N., 2011. Phase diagram of apatite system $Ca_{10}(PO_4)_6Cl_2$ - $Pb_{10}(PO_4)_6Cl_2$. *Thermochimica Acta* 526, 72-77.

Kohler, A., Weiden, P., 1954. Vorlaufige versuche in der feldspat-gruppe mittels der DTA. *Neues Jahrbuch fur Mineralogie - Monatshefte*, 249-252.

Kroll, H., Bambauer, H.U., 1981. Diffusive and displacive transformation in plagioclase and ternary feldspar series. *American Mineralogist* 66, 763-769.

Kroll, H., Mueller, W.F., 1980. X-ray and electron-optical investigation of synthetic high-temperature plagioclases. *Physics and Chemistry of Minerals* 5, 255-277.

Kula, J., Baldwin, S.L., 2011. Jarosite, argon diffusion, and dating aqueous mineralization on Earth and Mars. *Earth and Planetary Science Letters* 310, 314-318.

Kunz, M., Arlt, T., Stolz, J., 2000. *In-situ* powder diffraction study of titanite ($CaTiOSiO_4$) at high pressure and high temperature. *American Mineralogist* 85, 1465-1473.

Lee, J.K.W., 1995. Multipath diffusion in geochronology. *Contributions to Mineralogy and Petrology* 120, 60-82.

LeGeros, R.Z., Bonel, G., Legros, R., 1978. Types of H_2O in human enamel and in precipitated apatites. *Calcified Tissue International* 26, 111-118.

Lovera, O.M., Grove, M., Harrison, T.M., 2002. Systematic analysis of K-feldspar $^{40}Ar/^{39}Ar$ step heating results II: Relevance of laboratory argon diffusion properties to nature. *Geochimica et Cosmochimica Acta* 66, 1237-1255.

Lovera, O.M., Grove, M., Mark Harrison, T., Mahon, K.I., 1997. Systematic analysis of K-feldspar $^{40}Ar/^{39}Ar$ step heating results: I. Significance of activation energy determinations. *Geochimica et Cosmochimica Acta* 61, 3171-3192.

Lovera, O.M., Heizler, M.T., Harrison, T.M., 1993. Argon diffusion domains in K-feldspar II: Kinetic properties of MH-10. *Contributions to Mineralogy and Petrology* 113, 381-393.

Lovera, O.M., Richter, F.M., Harrison, T.M., 1989. The $^{40}Ar/^{39}Ar$ thermochronometry for slowly cooled samples having a distribution of diffusion domain sizes. *Journal of Geophysical Research* 94, 17917-17935.

Lovera, O.M., Richter, F.M., Harrison, T.M., 1991. Diffusion domains determined by ^{39}Ar released during step heating. *Journal of Geophysical Research* 96, 2057-2069.

Mackert, J.R., Twiggs, S.W., Williams, A.L., 2000. High-temperature x-ray diffraction measurement of sanidine thermal expansion. *Journal of Dental Research* 79, 1590-1595.

Malcherek, T., Domeneghetti, C.M., Tazzoli, V., Salje, E.K.H., Bismayer, U., 1999. A high temperature diffraction study of synthetic titanite $CaTiOSiO_4$. *Phase Transitions: A Multinational Journal* 69, 119-131.

Malcherek, T., Paulmann, C., Domeneghetti, M.C., Bismayer, U., 2001. Diffuse scattering anisotropy and the P21/a-A2/a phase transition in titanite, $CaTiOSiO_4$. *Journal of Applied Crystallography* 34, 108-113.

Mazzucato, E., Artioli, G., Gualtieri, A., 1999. High temperature dehydroxylation of muscovite-$2M_1$: a kinetic study by *in-situ* XRPD. *Physics and Chemistry of Minerals* 26, 375-381.

McDougall, I., Harrison, T.M., 1999. Geochronology and Thermochronology by the $^{40}Ar/^{39}Ar$ Method, 2nd Edition. Oxford University Press.

McLaren, A.C., 1974. Transmission electron microscopy of the feldspars, in: MacKenzie, W.S., Brown, W.L. (Eds.), The Feldspars. Manchester University Press, UK, pp. 378-423.

McLaren, A.C., Marshall, D.B., 1974. Transmission electron microscope study of the domain structures associated with the b-, c-, d-, e- and f-reflections in plagioclase feldspars. *Contributions to Mineralogy and Petrology* 44, 237-249.

McLaren, S., Dunlap, W.J., 2006. Use of $^{40}Ar/^{39}Ar$ K-feldspar thermochronology in basin thermal history reconstruction: an example from the Big Lake Suite granites, Warburton Basin, South Australia. *Basin Research* 18, 189-203.

McLaren, S., Dunlap, W.J., Powell, R., 2007. Understanding K-feldspar $^{40}Ar/^{39}Ar$ data:

reconciling models, methods and microtextures. *Journal of the Geological Society* 164, 941-944.

McLaren, S., Reddy, S.M., 2008. Automated mapping of K-feldspar by electron backscatter diffraction and application to $^{40}Ar/^{39}Ar$ dating. *Journal of Structural Geology* 30, 1229-1241.

McMillan, P.F., Brown, W.L., 1980. The unit-cell parameters of an ordered K-Rb alkali feldspar series. *American Mineralogist* 65, 458-464.

Megaw, H.D., 1973, Crystal structures: A working approach. W.B. Saunders Company, London.

Megaw, H.D., Kempster, C.J.E., Radoslovich, E.W., 1962. The structure of anorthite, $CaAl_2Si_2O_8$. II. Description and discussion. *Acta Crystallographica* 15, 1017-1035.

Monma, H., Ueno, S., Kanazawa, T., 1981. Properties of hydroxyapatite prepared by the hydrolysis of tricalcium phosphate. *Journal of Chemical Technology and Biotechnology* 31, 15-24.

Mueller, W.F., Wenk, H.R., Thomas, G., 1972. Structural variations in anorthites. *Contributions to Mineralogy and Petrology* 34, 304-314.

Mursic, Z., Vogt, T., Frey, F., 1992. High-temperature neutron powder diffraction study of $ZrSiO_4$ up to 1900 K. *Acta Crystallographica Chapter B: Structural Science* 48, 584-590.

Nord, G.L., Heuer, A.H., Lally, J.S., 1974. Transmission electron microscopy of substructures in Stillwater bytownites, in: MacKenzie, W.S., Zussman, J. (Eds.), The Feldspars. Manchester University Press, Manchester, pp. 522-535

Parsons, I., 2010. Feldspars defined and described: a pair of posters published by the Mineralogical Society. Sources and supporting information. *Mineralogical Magazine* 74, 529-551.

Parsons, I., Brown, W.L., Smith, J.V., 1999. $^{40}Ar/^{39}Ar$ thermochronology using alkali feldspars: real thermal history or mathematical mirage of microtexture? *Contributions to Mineralogy and Petrology* 136, 92-110.

Parsons, I., Fitz Gerald, J.D., Lee, J.K.W., Ivanic, T., Golla-Schindler, U., 2010. Time-temperature evolution of microtextures and contained fluids in a plutonic alkali feldspar during heating. *Contributions to Mineralogy and Petrology* 160, 155-180.

Parsons, I., Lee, M.R., 2005. Minerals are not just chemical compounds. *The Canadian Mineralogist* 43, 1959-1992.

Phillips, B.L., McGuinn, M.D., Redfern, S.A.T., 1997. Si-AI order and the II-12/c structural

phase transition in synthetic $CaAl_2Si_2O_8$-$SrAl_2Si_2O_8$ feldspar: A ^{29}Si MAS-NMR spectroscopic study. *American Mineralogist* 82, 1-7.

Podsiadlo, H., 1990. Polymorphic transitions in the binary system lead fluorapatite [$Pb_{10}(PO_4)_6F_2$] - calcium fluorapatite [$Ca_{10}(PO_4)_6F_2$]. *Journal of Thermal Analysis and Calorimetry* 36, 569-575.

Prewitt, C.T., Sueno, S., Papike, J.J., 1976. The crystal structures of high albite and monalbite at high temperatures. *American Mineralogist* 61, 1213-1225.

Quidelleur, X., Grove, M., Lovera, O.M., Harrison, T.M., Yin, A., Ryerson, F.J., 1997. Thermal evolution and slip history of the Renbu Zedong Thrust, southeastern Tibet. *Journal of Geophysical Research* 102, 2659-2679.

Rainey, C.S., Wenk, H.-R., 1978. Intensity differences of subsidiary reflections in calcic plagioclase. *American Mineralogist* 63, 124-131.

Reich, M., Ewing, R.C., Ehlers, T.A., Becker, U., 2007. Low-temperature anisotropic diffusion of helium in zircon: Implications for zircon (U-Th)/He thermochronometry. *Geochimica et Cosmochimica Acta* 71, 3119-3130.

Reiners, P.W., Ehlers, T.A., Zeitler, P.K., 2005. Past, present, and future of thermochronology. *Reviews in Mineralogy and Geochemistry* 58, 1-18.

Reiners, P.W., Farley, K.A., 1999. Helium diffusion and (U-Th)/He thermochronometry of titanite. *Geochimica et Cosmochimica Acta* 63, 3845-3859.

Reiners, P.W., Farley, K.A., Hickes, H.J., 2002. He diffusion and (U-Th)/He thermochronometry of zircon: initial results from Fish Canyon Tuff and Gold Butte. *Tectonophysics* 349, 297-308.

Reiners, P.W., Shuster, D.L., 2009. Thermochronology and landscape evolution. *Physics Today* 62, 31-36.

Reiners, P.W., Spell, T.L., Nicolescu, S., Zanetti, K.A., 2004. Zircon (U-Th)/He thermochronometry: He diffusion and comparisons with $^{40}Ar/^{39}Ar$ dating. *Geochimica et Cosmochimica Acta* 68, 1857-1887.

Renne, P.R., Deckart, K., Ernesto, M., Fe'raud, G., Piccirillo, E.M., 1996. Age of the Ponta Grossa dike swarm (Brazil), and implications to Parana flood volcanism. *Earth and Planetary Science Letters* 144, 199-211.

Renne, P.R., Knight, K.B., Nomade, S., Leung, K.N., Lou, T.P., 2005. Application of deuteron-deuteron (DD) fusion neutrons to $^{40}Ar/^{39}Ar$ geochronology. *Applied Radiation and Isotopes* 62, 25-32.

Renne, P.R., Norman, E.B., 2001. Determination of the half-life of ^{37}Ar by mass spectrometry. *Physical Review C* 63, 47302.

Renne, P.R., Onstott, T.C., D'Agrella-Filho, M.S., Pacca, I.G., Teixeira, W., 1990. $^{40}Ar/^{39}Ar$ dating of 1.0-1.1 Ga magnetizations from the Sao Francisco and Kalahari cratons: Tectonic implications for Pan-African and Brasiliano mobile belts. *Earth and Planetary Science Letters* 101, 349-366.

Renne, P.R., Scott, G.R., 1988. Structural chronology, oroclinal deformation, and tectonic evolution of the southeastern Klamath Mountains, California. *Tectonics* 7, 1223-1242.

Renne, P.R., Swisher, C.C., Deino, A.L., Karner, D.B., Owens, T.L., DePaolo, D.J., 1998. Intercalibration of standards, absolute ages and uncertainties in $^{40}Ar/^{39}Ar$ dating. *Chemical Geology* 145, 117-152.

Richter, F.M., Lovera, O.M., Mark Harrison, T., Copeland, P., 1991. Tibetan tectonics from $^{40}Ar/^{39}Ar$ analysis of a single K-feldspar sample. *Earth and Planetary Science Letters* 105, 266-278.

Righter, K., Carmichael, I., 1993. Mega-xenocrysts in alkali olivine basalts: Fragments of disrupted mantle assemblages. *American Mineralogist* 78, 1230-1245.

Saadoune, I., Purton, J.A., de Leeuw, N.H., 2009. He incorporation and diffusion pathways in pure and defective zircon $ZrSiO_4$: A density functional theory study. *Chemical Geology* 258, 182-196.

Salje, E., Kuscholke, B., Wruck, B., Kroll, H., 1985. Thermodynamics of sodium feldspar II: experimental results and numerical calculations. *Physics and Chemistry of Minerals* 12, 99-107.

Sanders, R.E., Heizler, M.T., Goodwin, L.B., 2006. $^{40}Ar/^{39}Ar$ thermochronology constraints on the timing of Proterozoic basement exhumation and fault ancestry, southern Sangre de Cristo Range, New Mexico. *Geological Society of America Bulletin* 118, 1489-1506.

Shearer, C.K., Burger, P.V., Neal, C., Sharp, Z., Spivak-Birndorf, L., Borg, L., Fernandes, V.A., Papike, J.J., Karner, J., Wadhwa, M., 2010. Non-basaltic asteroidal magmatism during the earliest stages of solar system evolution: A view from Antarctic achondrites Graves Nunatak 06128 and 06129. *Geochimica et Cosmochimica Acta* 74, 1172-1199.

Short, C., Heizler, M.T., Heizler, L.L., Parsons, I., 2010. Advancing the $^{40}Ar/^{39}Ar$ MDD method through micoanalysis of microtexturally characterized K-feldspar crystal fragments, GSA Annual Meeting.

Shuster, D.L., Balco, G., Cassata, W.S., Fernandes, V.A., Garrick-Bethell, I., Weiss, B.P.,

2010. A record of impacts preserved in the lunar regolith. *Earth and Planetary Science Letters* 290, 155-165.

Shuster, D.L., Farley, K.A., 2005. $^{4}He/^{3}He$ thermochronometry: theory, practice, and potential complications. *Reviews in Mineralogy and Geochemistry* 58, 181-203.

Shuster, D.L., Farley, K.A., 2009. The influence of artificial radiation damage and thermal annealing on helium diffusion kinetics in apatite. *Geochimica et Cosmochimica Acta* 73, 183-196.

Shuster, D.L., Farley, K.A., Sisterson, J.M., Burnett, D.S., 2004. Quantifying the diffusion kinetics and spatial distributions of radiogenic ^{4}He in minerals containing proton-induced ^{3}He. *Earth and Planetary Science Letters* 217, 19-32.

Shuster, D.L., Flowers, R.M., Farley, K.A., 2006. The influence of natural radiation damage on helium diffusion kinetics in apatite. *Earth and Planetary Science Letters* 249, 148-161.

Simoes, M., Avouac, J.P., Beyssac, O., Goffe, B., Farley, K.A., Chen, Y.G., 2007. Mountain building in Taiwan: A thermokinematic model. *Journal of Geophysical Research* 112, B11405.

Smith, J.V., Ribbe, P.H., 1969. Atomic movements in plagioclase feldspars: kinetic interpretation. *Contributions to Mineralogy and Petrology* 21, 157-202.

Stewart, D.B., Von Limbach, D., 1967. Thermal expansion of low and high albite. *American Mineralogist* 52, 389-413.

Stewart, D.B., Walker, G.W., Wright, T.L., Fahey, J.J., 1966. Physical properties of calcific labradorite from Lake County, Oregon. *American Mineralogist* 51, 177-197.

Taylor, M., Brown, G.E., 1976. High-temperature structural study of the $P2_1/a$-A2/a phase transition in synthetic titanite, $CaTiSiO_5$. *American Mineralogist* 61, 435-447.

Tribaudino, M., Angel, R.J., Camara, F., Nestola, F., Pasqual, D., Margiolaki, I., 2010. Thermal expansion of plagioclase feldspars. *Contributions to Mineralogy and Petrology* 160, 899-908.

Van Tendeloo, G., Ghose, S., Amelinckx, S., 1989. A Dynamical Model for the PI-II Phase Transition in Anorthite, CaAl2Si208. *Physics and Chemistry of Minerals* 16, 311-319.

Villa, I.M., 2006. From nanometer to megameter: Isotopes, atomic-scale processes, and continent-scale tectonic models. *Lithos* 87, 155-173.

Villa, I.M., 2010. Disequilibrium textures versus equilibrium modelling: geochronology at the crossroads. *Geological Society, London, Special Publications* 332, 1-15.

Vineyard, G.H., 1957. Frequency factors and isotope effects in solid state rate processes. *Journal of Physics and Chemistry of Solids* 3, 121-127.

Voltaggio, M., 1985. Estimation of diffusion constants by observations of isokinetic effects: A test for radiogenic argon and strontium. *Geochimica et Cosmochimica Acta* 49, 2117-2122.

Wartho, J.-A., Dodson, M.H., Rex, D.C., Guise, P.G., 1991. Mechanisms of Ar release from Himalayan metamorphic hornblende. *American Mineralogist* 76, 1446-1448.

Wartho, J.-A., Kelley, S.P., Brooker, R.A., Carroll, M.R., Villa, I.M., Lee, M.R., 1999. Direct measurement of Ar diffusion profiles in a gem-quality Madagascar K-feldspar using the ultra-violet laser ablation microprobe (UVLAMP). *Earth and Planetary Science Letters* 170, 141-153.

Watanabe, K., Austin, N., Stapleton, M.R., 1995. Investigation of the air separation properties of zeolite types A, X, and Y by Monte Carlo simulations. *Molecular Simulation* 15, 197-221.

Wenk, H.-R., Nakajima, Y., 1980. Structure, formation, and decomposition of APB's in calcic plagioclase. *Physics and Chemistry of Minerals* 6, 169-186.

Wenk, H.-R., 1978. Ordering of the intermediate plagioclase structure during heating. *American Mineralogist* 63, 132-135.

Wenk, H.-R., 1979. Superstructure variation in metamorphic intermediate plagioclase. *American Mineralogist* 64, 71-76.

Wenk, H.-R., Joswig, W., Tagai, T., Korekawa, M., Smith, B.K., 1980. The average structure of An_{62-66} labradorite. *American Mineralogist* 65, 8I-95.

Wenk, H.-R., Mueller, W.F., Thomas, G., 1973. Antiphase domains in lunar plagioclase. *Proceedings of the Lunar Science Conference* 4, 909-923.

Winter, J.K., Okamura, F.P., Ghose, S., 1979. A high-temperature structural study of high albite, monalbite, and the analbite - monalbite phase transition. *American Mineralogist* 64, 409-423.

Wolf, R.A., Farley, K.A., Silver, L.T., 1996. Helium diffusion and low-temperature thermochronometry of apatite. *Geochimica et Cosmochimica Acta* 60, 4231-4240.

Yashima, M., Yonehara, Y., Fujimori, H., 2011. Experimental visualization of chemical bonding and structural disorder in hydroxyapatite through charge and nuclear-density analysis. *The Journal of Physical Chemistry C* 115, 25077–25087.

Zeitler, P.K., Herczeg, A.L., McDougall, I., Honda, M., 1987. U-Th-He dating of apatite: A

potential thermochronometer. *Geochimica et Cosmochimica Acta* 51, 2865-2868.

Zhao, Z.-F., Zheng, Y.-F., 2007. Diffusion compensation for argon, hydrogen, lead, and strontium in minerals: Empirical relationships to crystal chemistry. *American Mineralogist* 92, 289-308.

Appendix: Analytical Details

BMk-1

#	E_a	Temp (°C)	Time (s)	^{39}Ar ± 1σ (nA)	^{37}Ar ± 1σ (nA)
1	X	463 °C	2996	0.00252	0.00007
2	X	463 °C	2997	0.00139	0.00005
3	X	516 °C	2997	0.00760	0.00009
4	X	516 °C	2997	0.00461	0.00007
5	X	570 °C	2996	0.02246	0.00015
6	X	570 °C	2996	0.01464	0.00012
7	X	622 °C	1996	0.04282	0.00018
8	X	674 °C	1997	0.10222	0.00035
9	X	674 °C	1996	0.07122	0.00028
10	X	726 °C	1996	0.20187	0.00053
11	X	726 °C	1996	0.15073	0.00039
12	X	777 °C	997	0.20669	0.00059
13	X	778 °C	997	0.16362	0.00046
14	X	830 °C	996	0.39034	0.00080
15	X	829 °C	497	0.15092	0.00040
16	X	879 °C	497	0.35541	0.00100
17	X	880 °C	497	0.29998	0.00086
18	X	931 °C	496	0.63199	0.00100
19	X	930 °C	297	0.30060	0.00079
20	X	930 °C	296	0.27361	0.00080
21	X	980 °C	297	0.58221	0.00100
22	X	980 °C	296	0.49241	0.00120
23		1030 °C	297	0.93208	0.00150
24		1029 °C	296	0.76655	0.00120
25		1056 °C	297	0.95943	0.00151
26		1067 °C	297	0.95264	0.00130
27		1066 °C	296	0.83306	0.00131
28		1081 °C	296	0.92389	0.00161
29		1079 °C	297	0.81602	0.00131
30		1096 °C	296	0.89563	0.00141
31		1111 °C	297	0.96784	0.00151
32		1131 °C	296	1.07273	0.00161
33		1150 °C	297	1.12620	0.00161
34		1181 °C	296	1.11274	0.00180
35		1229 °C	296	2.99007	0.00440
36		1229 °C	296	0.86207	0.00151
37		1210 °C	297	0.05889	0.00033
38		1219 °C	296	0.02133	0.00033
39		1230 °C	297	0.01078	0.00026
40		1227 °C	296	0.00463	0.00022
41		1230 °C	297	0.00076	0.00019
42		1240 °C	296	0.00062	0.00017
43		1240 °C	297	---	---

#	E_a	Temp (°C)	Time (s)	^{39}Ar ± 1σ (nA)	^{37}Ar ± 1σ (nA)
44		1249 °C	296	0.00020	0.00017
45		1250 °C	296	0.00003	0.00013
46		1258 °C	297	---	---
47		1140 °C	294	---	---
48		1269 °C	297	---	---
49		1269 °C	296	0.00038	0.00012
50		1279 °C	296	0.00007	0.00010
51		1278 °C	296	---	---
52		1302 °C	297	0.00011	0.00009
53		1326 °C	296	0.00009	0.00011
54		1326 °C	297	0.00022	0.00009
55		1351 °C	296	0.00055	0.00011
56		1352 °C	296	0.00058	0.00012
57		1371 °C	297	0.00039	0.00009
58		1371 °C	297	0.00107	0.00010

BMk-2

1	X	463 °C	2997	0.00394	0.00008
2	X	463 °C	2997	0.00215	0.00006
3	X	516 °C	2997	0.01180	0.00011
4	X	516 °C	2996	0.00672	0.00009
5	X	570 °C	2996	0.03469	0.00023
6	X	569 °C	2996	0.02173	0.00016
7	X	622 °C	1996	0.06243	0.00023
8	X	674 °C	1996	0.14306	0.00036
9	X	674 °C	1997	0.09689	0.00045
10	X	727 °C	1997	0.26447	0.00088
11	X	727 °C	1997	0.18807	0.00042
12	X	777 °C	996	0.25189	0.00073
13	X	778 °C	997	0.20027	0.00052
14	X	830 °C	996	0.47573	0.00100
15	X	829 °C	497	0.18301	0.00049
16	X	880 °C	496	0.44762	0.00099
17	X	880 °C	497	0.35638	0.00100
18	X	931 °C	497	0.78822	0.00130
19	X	928 °C	297	0.35723	0.00087
20	X	930 °C	296	0.32388	0.00091
21	X	981 °C	297	0.71511	0.00140
22	X	979 °C	296	0.60999	0.00130
23		1030 °C	297	1.15627	0.00150
24		1031 °C	297	0.92884	0.00160
25		1056 °C	295	1.14921	0.00141
26		1066 °C	297	1.11219	0.00150
27		1066 °C	297	0.94349	0.00151
28		1081 °C	296	1.03751	0.00171
29		1080 °C	297	0.91121	0.00161
30		1095 °C	296	1.00179	0.00141

#	E_a	Temp (°C)	Time (s)	^{39}Ar ± 1σ (nA)	^{37}Ar ± 1σ (nA)
31		1109 °C	296	1.10086 0.00151	
32		1131 °C	297	1.28625 0.00181	
33		1150 °C	296	1.43233 0.00181	
34		1181 °C	297	1.58104 0.00240	
35		1230 °C	297	6.24278 0.00671	
36		1230 °C	297	5.73129 0.00601	
37		1207 °C	297	2.31400 0.00311	
38		1220 °C	297	1.39115 0.00231	
39		1229 °C	296	0.81709 0.00131	
40		1230 °C	297	0.44771 0.00101	
41		1230 °C	296	0.22414 0.00077	
42		1239 °C	297	0.12299 0.00038	
43		1240 °C	296	0.06124 0.00029	
44		1249 °C	296	0.03464 0.00022	
45		1249 °C	296	0.01890 0.00019	
46		1259 °C	297	0.01144 0.00016	
47		1258 °C	297	0.00689 0.00016	
48		1268 °C	296	0.00796 0.00014	
49		1269 °C	296	0.00758 0.00012	
50		1279 °C	297	0.00734 0.00012	
51		1278 °C	297	0.00623 0.00014	
52		1301 °C	296	0.07634 0.00031	
53		1326 °C	297	0.02777 0.00024	
54		1328 °C	296	0.00775 0.00012	
55		1349 °C	296	0.00568 0.00013	
56		1347 °C	297	0.00388 0.00012	
57		1374 °C	297	0.01373 0.00014	
58		1372 °C	297	0.00092 0.00010	

BMk-3

1	X	463 °C	2996	0.01061 0.00012	
2	X	463 °C	2997	0.00381 0.00007	
3	X	516 °C	2996	0.02413 0.00016	
4	X	516 °C	2997	0.01390 0.00012	
5	X	570 °C	2997	0.06411 0.00027	
6	X	569 °C	2996	0.04368 0.00019	
7	X	622 °C	1997	0.11856 0.00037	
8	X	622 °C	1997	0.08485 0.00026	
9	X	675 °C	1997	0.27222 0.00069	
10	X	674 °C	1996	0.18624 0.00050	
11	X	726 °C	1997	0.51360 0.00110	
12	X	726 °C	1996	0.35128 0.00094	
13	X	777 °C	996	0.47299 0.00120	
14	X	778 °C	996	0.37284 0.00092	
15	X	829 °C	997	0.92641 0.00150	
16	X	829 °C	497	0.33235 0.00086	
17	X	880 °C	497	0.81925 0.00130	

#	E_a	Temp (°C)	Time (s)	^{39}Ar ± 1σ (nA)	^{37}Ar ± 1σ (nA)
18	X	880 °C	497	0.63030	0.00120
19	X	930 °C	296	1.00993	0.00150
20	X	929 °C	297	0.68119	0.00140
21	X	980 °C	296	1.93187	0.00250
22	X	980 °C	297	1.24060	0.00170
23		1030 °C	297	2.14947	0.00270
24		1031 °C	296	1.63084	0.00230
25		1055 °C	297	1.87174	0.00220
26		1066 °C	296	1.70736	0.00230
27		1066 °C	297	1.41602	0.00211
28		1081 °C	297	1.49897	0.00211
29		1081 °C	297	1.28062	0.00201
30		1096 °C	296	1.38507	0.00181
31		1111 °C	297	1.48183	0.00221
32		1131 °C	297	1.71911	0.00231
33		1151 °C	296	1.91755	0.00241
34		1181 °C	296	2.47605	0.00370
35		1201 °C	296	5.10941	0.00641
36		1221 °C	297	20.77150	0.02902
37		1209 °C	297	15.08010	0.01901
38		1219 °C	296	9.30147	0.01201
39		1230 °C	297	6.37757	0.00821
40		1230 °C	297	4.56694	0.00651
41		1230 °C	296	3.00268	0.00400
42		1240 °C	297	2.31917	0.00330
43		1241 °C	296	1.62432	0.00201
44		1251 °C	297	1.20342	0.00151
45		1250 °C	297	0.73229	0.00130
46		1259 °C	297	0.45011	0.00101
47		1260 °C	297	0.29321	0.00085
48		1269 °C	296	0.22228	0.00077
49		1270 °C	297	0.17067	0.00044
50		1280 °C	297	0.14119	0.00047
51		1275 °C	297	0.11772	0.00032
52		1300 °C	296	0.09928	0.00037
53		1328 °C	296	0.27484	0.00069
54		1323 °C	297	0.18026	0.00044
55		1349 °C	296	3.08946	0.00390
56		1348 °C	297	1.33320	0.00160
57		1373 °C	297	0.10796	0.00035
58		1370 °C	296	1.58710	0.00200
59		1379 °C	295	0.00081	0.00089
60		1356 °C	294	0.00033	0.00130
BMk-4					
1	X	502 °C	591	0.00106	0.00006
2	X	499 °C	596	0.00041	0.00007

#	E_a	Temp (°C)	Time (s)	^{39}Ar ± 1σ (nA)	^{37}Ar ± 1σ (nA)
3	X	549 °C	582	0.00192 0.00011	
4	X	600 °C	585	0.00357 0.00009	
5	X	599 °C	597	0.00249 0.00007	
6	X	651 °C	591	0.01316 0.00062	
7	X	649 °C	597	0.00685 0.00014	
8	X	699 °C	596	0.01976 0.00023	
9	X	700 °C	591	0.01427 0.00016	
10	X	750 °C	596	0.03664 0.00018	
11	X	750 °C	591	0.02681 0.00020	
12	X	799 °C	597	0.06264 0.00030	
13	X	799 °C	596	0.04580 0.00027	
14	X	848 °C	596	0.10142 0.00040	
15	X	849 °C	597	0.08153 0.00030	
16	X	899 °C	596	0.17132 0.00052	
17	X	899 °C	597	0.12798 0.00038	
18	X	948 °C	597	0.24658 0.00076	
19	X	949 °C	591	0.17925 0.00048	
20	X	999 °C	596	0.28639 0.00084	
21	X	999 °C	597	0.22924 0.00070	
22	X	1047 °C	596	0.39068 0.00098	
23	X	1049 °C	597	0.52764 0.00120	
24		1099 °C	597	2.07701 0.00270	
25		1099 °C	597	0.09703 0.00040	
26		1146 °C	597	0.00115 0.00010	
27		1149 °C	597	0.00070 0.00009	
28		1197 °C	597	0.00160 0.00010	
29		1197 °C	597	0.00702 0.00018	
30		1246 °C	591	0.02303 0.00033	
31		1240 °C	596	0.02605 0.00027	
32		1169 °C	597	0.00222 0.00011	
33		1169 °C	597	0.00234 0.00011	
34		1214 °C	596	0.00688 0.00015	
35		1214 °C	596	0.01295 0.00022	

BMk-5

1	X	460 °C	596	0.00046 0.00007	
2	X	460 °C	597	0.00029 0.00007	
3	X	514 °C	596	0.00311 0.00010	
4	X	514 °C	596	0.00122 0.00008	
5	X	567 °C	597	0.00536 0.00011	
6	X	567 °C	596	0.00323 0.00010	
7	X	620 °C	597	0.01377 0.00015	
8	X	619 °C	596	0.00946 0.00011	
9	X	673 °C	596	0.03415 0.00025	
10	X	672 °C	597	0.02245 0.00019	
11	X	724 °C	596	0.06858 0.00026	
12	X	724 °C	596	0.04700 0.00022	

#	E_a	Temp (°C)	Time (s)	^{39}Ar ± 1σ (nA)	^{37}Ar ± 1σ (nA)
13	X	777 °C	596	0.12127	0.00044
14	X	777 °C	596	0.08730	0.00035
15		598 °C	596	0.00066	0.00006
16		683 °C	597	0.00619	0.00010
17		757 °C	597	0.04201	0.00023
18		828 °C	596	0.19941	0.00066
19		829 °C	596	0.13366	0.00050
20		880 °C	596	0.32108	0.00110
21		880 °C	596	0.20968	0.00074
22		932 °C	596	0.41634	0.00094
23		931 °C	596	0.29465	0.00097
24		982 °C	596	0.53331	0.00140
25		982 °C	597	0.37494	0.00094
26		1032 °C	597	0.61475	0.00160
27		1032 °C	596	0.41893	0.00120
28		1083 °C	597	0.62827	0.00140
29		850 °C	596	0.00831	0.00016
30		962 °C	596	0.06794	0.00031
31		1053 °C	596	0.25658	0.00083
32		1133 °C	596	0.57092	0.00110
33		1133 °C	596	0.35133	0.00111
34		1182 °C	596	0.42540	0.00100
35		1183 °C	596	0.24728	0.00091
36		1232 °C	596	1.29185	0.00190
37		1232 °C	596	0.78871	0.00170
38		1281 °C	597	0.67200	0.00140
39		1281 °C	596	0.09653	0.00042
40		1330 °C	597	0.00858	0.00013
41		1427 °C	597	0.00244	0.00009

XTALk-1

1		464 °C	596	0.00024	0.00004
2		464 °C	597	0.00025	0.00004
3		518 °C	596	0.00272	0.00004
4		518 °C	596	0.00220	0.00004
5	X	570 °C	597	0.01182	0.00011
6	X	571 °C	597	0.00741	0.00008
7	X	624 °C	597	0.02975	0.00014
8	X	623 °C	596	0.01970	0.00013
9	X	676 °C	596	0.07030	0.00025
10	X	675 °C	596	0.04842	0.00022
11	X	728 °C	596	0.14883	0.00042
12	X	728 °C	596	0.10262	0.00032
13	X	780 °C	596	0.27564	0.00062
14	X	780 °C	597	0.18919	0.00039
15	X	832 °C	597	0.43278	0.00089
16	X	831 °C	597	0.26313	0.00070

#	E_a	Temp (°C)	Time (s)	^{39}Ar ± 1σ (nA)	^{37}Ar ± 1σ (nA)
17		984 °C	597	2.04273 0.00230	
18		984 °C	596	0.80362 0.00110	
19		1034 °C	596	0.87652 0.00120	
20		1034 °C	597	0.44067 0.00093	
21		CO_2		2.52159 0.00340	
22		CO_2		1.48516 0.00190	
23		CO_2		1.30673 0.00190	
24		CO_2		0.98072 0.00130	
25		CO_2		0.14357 0.00035	
26		CO_2		0.01669 0.00018	
27		CO_2		0.00191 0.00009	
28		CO_2		0.00293 0.00008	
29		CO_2		0.00101 0.00007	
30		CO_2		0.00067 0.00007	
31		CO_2		0.01259 0.00018	
32		CO_2		0.02468 0.00020	
33		CO_2		0.00055 0.00007	
34		CO_2		-0.00006 0.00004	
35		CO_2		-0.00005 0.00006	
36		CO_2		0.00140 0.00004	

MADk-1

1	X	463 °C	2996	0.02056 0.00012	
2	X	463 °C	2997	0.01059 0.00010	
3	X	517 °C	2997	0.07458 0.00024	
4	X	517 °C	2997	0.04519 0.00023	
5	X	570 °C	2994	0.25375 0.00069	
6	X	570 °C	2997	0.17370 0.00037	
7	X	622 °C	1997	0.57518 0.00110	
8	X	622 °C	1997	0.42680 0.00089	
9	X	674 °C	1996	1.74723 0.00170	
10	X	674 °C	1997	1.19320 0.00150	
11	X	726 °C	1996	3.94009 0.00530	
12	X	726 °C	1997	2.72220 0.00390	
13	X	778 °C	997	3.70011 0.00380	
14	X	778 °C	997	2.60882 0.00340	
15		829 °C	996	5.32446 0.00480	
16		829 °C	496	1.52760 0.00190	
17		879 °C	497	3.38814 0.00400	
18		879 °C	497	2.37142 0.00290	
19		930 °C	297	2.99211 0.00380	
20		929 °C	297	2.58662 0.00340	
21		981 °C	297	6.35612 0.00630	
22		981 °C	296	5.78614 0.00520	
23		1030 °C	297	12.71679 0.01201	
24		1031 °C	297	10.95910 0.01201	
25		1055 °C	296	13.80553 0.01501	

#	E_a	Temp (°C)	Time (s)	^{39}Ar ± 1σ (nA)	^{37}Ar ± 1σ (nA)
26		1067 °C	297	13.42688	0.01401
27		1066 °C	297	11.62915	0.01001
28		1081 °C	297	12.03718	0.01001
29		1082 °C	296	10.05081	0.00901
30		1096 °C	297	9.94383	0.01101
31		1111 °C	296	9.33623	0.00911
32		1130 °C	297	8.64089	0.00851
33		1151 °C	296	7.22450	0.00671
34		1180 °C	297	6.24731	0.00591
35		1210 °C	297	5.38850	0.00561
36		1220 °C	294	4.63919	0.00511
37		1230 °C	296	2.58293	0.00371
38		1230 °C	297	1.31843	0.00170
39		1230 °C	296	1.23541	0.00171
40		1240 °C	296	1.20861	0.00171
41		1239 °C	297	0.99422	0.00161
42		1250 °C	297	0.88983	0.00131
43		1249 °C	296	0.65344	0.00111
44		1259 °C	296	0.45547	0.00077
45		1255 °C	297	0.31107	0.00084
46		1269 °C	296	0.22937	0.00077
47		1271 °C	296	0.16508	0.00043
48		1276 °C	296	0.14874	0.00038
49		1275 °C	297	2.02706	0.00250
50		1295 °C	296	0.06723	0.00028
51		1320 °C	296	0.07263	0.00031
52		1320 °C	295	0.10052	0.00031
53		1346 °C	296	0.05992	0.00026
54		1344 °C	296	0.65472	0.00110
55		1370 °C	297	0.18498	0.00040
56		1369 °C	296	0.07100	0.00029
57		1374 °C	294	0.11051	0.00030
58		1314 °C	293	0.01866	0.00019

MADk-2

1	X	463 °C	2996	0.00867	0.00009
2	X	463 °C	2997	0.00464	0.00008
3	X	517 °C	2997	0.02881	0.00013
4	X	517 °C	2996	0.01689	0.00012
5	X	570 °C	2997	0.09504	0.00034
6	X	570 °C	2997	0.06334	0.00026
7	X	622 °C	1996	0.20526	0.00060
8	X	622 °C	1996	0.15467	0.00045
9	X	674 °C	1996	0.61610	0.00110
10	X	675 °C	1996	0.43027	0.00087
11	X	726 °C	1997	1.35556	0.00160
12	X	727 °C	1996	0.93726	0.00130

#	E_a	Temp (°C)	Time (s)	^{39}Ar ± 1σ (nA)	^{37}Ar ± 1σ (nA)
13	X	778 °C	996	1.31613 0.00160	
14	X	777 °C	996	0.93998 0.00150	
15		827 °C	496	1.10113 0.00150	
16		829 °C	497	0.78162 0.00150	
17		880 °C	497	1.62231 0.00220	
18		880 °C	497	1.10289 0.00170	
19		929 °C	296	1.41756 0.00170	
20		930 °C	297	1.26381 0.00190	
21		981 °C	297	3.12137 0.00440	
22		980 °C	297	2.80137 0.00340	
23		1006 °C	297	3.98014 0.00400	
24		1042 °C	296	6.98730 0.00691	
25		1056 °C	297	7.34802 0.00771	
26		1066 °C	297	7.33163 0.00831	
27		1066 °C	296	6.24318 0.00691	
28		1081 °C	296	6.27572 0.00631	
29		1081 °C	296	5.07695 0.00631	
30		1096 °C	296	4.79928 0.00541	
31		1111 °C	296	4.94276 0.00651	
32		1130 °C	297	3.73474 0.00441	
33		1151 °C	297	3.67500 0.00471	
34		1181 °C	294	2.65428 0.00351	
35		1210 °C	297	1.99774 0.00212	
36		1221 °C	295	3.27596 0.00411	
37		1230 °C	296	2.87335 0.00451	
38		1231 °C	297	2.00400 0.00220	
39		1226 °C	296	0.62665 0.00101	
40		1240 °C	297	0.35975 0.00092	
41		1240 °C	297	0.20380 0.00059	
42		1249 °C	297	0.12595 0.00042	
43		1250 °C	296	0.07670 0.00032	
44		1258 °C	296	0.04868 0.00026	
45		1260 °C	297	0.03094 0.00025	
46		1270 °C	297	0.02643 0.00021	
47		1267 °C	297	0.21001 0.00056	
48		1279 °C	296	0.02770 0.00016	
49		1277 °C	296	0.14730 0.00047	
50		1304 °C	296	0.01296 0.00015	
51		1328 °C	297	0.02198 0.00026	
52		1325 °C	296	0.00659 0.00014	
53		1347 °C	296	0.22712 0.00073	
54		1348 °C	297	0.00493 0.00012	
55		1376 °C	295	0.00155 0.00009	
56		1373 °C	296	0.00243 0.00009	

MADk-3

1		???	580	0.00100 0.00080	

#	E_a	Temp (°C)	Time (s)	^{39}Ar ± 1σ (nA)	^{37}Ar ± 1σ (nA)
2	X	475 °C	580	0.00246	0.00007
3	X	500 °C	580	0.00384	0.00008
4	X	525 °C	580	0.00652	0.00008
5	X	550 °C	580	0.01173	0.00011
6	X	575 °C	580	0.02210	0.00014
7	X	600 °C	580	0.04243	0.00022
8	X	625 °C	580	0.07620	0.00026
9	X	700 °C	180	0.19110	0.00037
10	X	800 °C	180	1.40190	0.00180
11	X	900 °C	180	3.74805	0.00421
12		CO_2		21.46841	0.03149
MADk-4					
1	X	475 °C	580	0.00215	0.00006
2	X	500 °C	580	0.00350	0.00008
3	X	525 °C	580	0.00554	0.00009
4	X	550 °C	580	0.00976	0.00010
5	X	575 °C	580	0.01747	0.00013
6	X	600 °C	580	0.03134	0.00016
7	X	625 °C	580	0.05531	0.00020
8	X	700 °C	180	0.13215	0.00033
9	X	800 °C	181	0.93482	0.00170
10	X	900 °C	180	2.97988	0.00330
11		CO_2		20.57885	0.03038
MADk-5					
1	X	463 °C	2997	0.00789	0.00010
2	X	463 °C	2997	0.00398	0.00008
3	X	516 °C	2997	0.02684	0.00018
4	X	517 °C	2996	0.01621	0.00012
5	X	569 °C	2997	0.10172	0.00028
6	X	569 °C	2997	0.07129	0.00021
7	X	622 °C	1997	0.24302	0.00065
8	X	622 °C	1996	0.18446	0.00048
9	X	674 °C	1996	0.76144	0.00110
10	X	674 °C	1997	0.53447	0.00110
11	X	726 °C	1996	1.71120	0.00190
12	X	727 °C	1997	1.18807	0.00160
13	X	777 °C	997	1.65028	0.00170
14	X	778 °C	997	1.19222	0.00170
15		828 °C	497	1.27712	0.00180
16		829 °C	497	0.88333	0.00100
17		879 °C	497	1.64376	0.00160
18		880 °C	494	0.97954	0.00140
19		929 °C	296	1.13945	0.00130
20		928 °C	296	0.93123	0.00140

#	E_a	Temp (°C)	Time (s)	$^{39}Ar \pm 1\sigma$ (nA)	$^{37}Ar \pm 1\sigma$ (nA)
21		980 °C	297	2.32299 0.00310	
22		980 °C	296	2.12645 0.00280	
23		1005 °C	297	3.26199 0.00370	
24		1041 °C	296	5.45643 0.00580	
25		1057 °C	296	5.59793 0.00560	
26		1066 °C	296	5.34890 0.00540	
27		1065 °C	296	4.52136 0.00531	
28		1080 °C	296	4.52419 0.00501	
29		1081 °C	297	3.66131 0.00460	
30		1096 °C	296	3.54248 0.00471	
31		1111 °C	296	3.22485 0.00471	
32		1131 °C	297	2.90007 0.00391	
33		1151 °C	296	2.42432 0.00331	
34		1181 °C	296	2.03352 0.00261	
35		1211 °C	297	1.64914 0.00202	
36		1221 °C	296	0.76170 0.00113	
37		1230 °C	296	0.90023 0.00151	
38		1230 °C	296	1.18429 0.00190	
39		1227 °C	297	1.24364 0.00201	
40		1238 °C	297	1.23152 0.00151	
41		1239 °C	296	1.09753 0.00151	
42		1250 °C	296	0.99427 0.00141	
43		1250 °C	297	0.82462 0.00130	
44		1258 °C	297	0.67733 0.00100	
45		1258 °C	296	0.51620 0.00099	
46		1269 °C	297	0.35027 0.00073	
47		1269 °C	297	0.21966 0.00074	
48		1279 °C	297	0.12340 0.00038	
49		1278 °C	296	0.05930 0.00024	
50		1303 °C	297	0.02933 0.00016	
51		1326 °C	297	0.01248 0.00020	
52		1328 °C	296	0.01297 0.00016	
53		1352 °C	297	0.00234 0.00010	
54		1352 °C	297	0.00285 0.00011	
55		1376 °C	296	0.01432 0.00016	
56		1372 °C	296	0.01937 0.00017	
57		1384 °C	294	0.00082 0.00008	
58		1373 °C	295	0.00516 0.00011	

MADk-6

1	X	460 °C	597	0.00051 0.00008	
2	X	460 °C	597	0.00043 0.00007	
3	X	513 °C	597	0.00252 0.00008	
4	X	513 °C	597	0.00144 0.00007	
5	X	567 °C	597	0.00584 0.00014	
6	X	567 °C	597	0.00374 0.00009	
7	X	620 °C	596	0.01741 0.00018	

#	E_a	Temp (°C)	Time (s)	^{39}Ar ± 1σ (nA)	^{37}Ar ± 1σ (nA)
8	X	619 °C	596	0.01125	0.00017
9	X	672 °C	596	0.04619	0.00026
10	X	673 °C	596	0.03120	0.00022
11	X	725 °C	597	0.11229	0.00035
12	X	725 °C	596	0.08072	0.00034
13	X	777 °C	596	0.24918	0.00076
14	X	776 °C	597	0.18423	0.00055
15		598 °C	597	0.00103	0.00008
16		683 °C	596	0.01049	0.00015
17		757 °C	596	0.08596	0.00041
18		829 °C	596	0.46013	0.00120
19		829 °C	596	0.36367	0.00110
20		880 °C	597	0.73072	0.00150
21		880 °C	597	0.39548	0.00098
22		931 °C	597	0.53483	0.00120
23		932 °C	597	0.23680	0.00069
24		982 °C	597	0.41768	0.00110
25		982 °C	596	0.36201	0.00098
26		1033 °C	597	0.97607	0.00150
27		1033 °C	597	0.86847	0.00160
28		1083 °C	596	1.60919	0.00220
29		850 °C	597	0.01440	0.00017
30		962 °C	596	0.14210	0.00045
31		1053 °C	596	0.58206	0.00120
32		1133 °C	597	1.02861	0.00170
33		1133 °C	596	0.38098	0.00097
34		1182 °C	596	0.26171	0.00080
35		1182 °C	597	0.08926	0.00033
36		1232 °C	597	0.08885	0.00048
37		1232 °C	597	0.05640	0.00030
38		1281 °C	597	0.02871	0.00022
39		1281 °C	597	0.00434	0.00016
40		1330 °C	594	0.00048	0.00007
41		1426 °C	597	0.00017	0.00008

MADk-7

1	X	460 °C	597	0.00041	0.00007
2	X	460 °C	597	0.00036	0.00007
3	X	513 °C	597	0.00245	0.00008
4	X	513 °C	596	0.00141	0.00008
5	X	567 °C	596	0.00731	0.00017
6	X	567 °C	597	0.00393	0.00013
7	X	619 °C	597	0.01897	0.00017
8	X	620 °C	596	0.01305	0.00015
9	X	672 °C	596	0.05335	0.00030
10	X	672 °C	597	0.03595	0.00024
11	X	724 °C	596	0.12300	0.00044

#	E_a	Temp (°C)	Time (s)	^{39}Ar ± 1σ (nA)	^{37}Ar ± 1σ (nA)
12	X	725 °C	597	0.09210	0.00033
13	X	777 °C	596	0.26590	0.00091
14	X	777 °C	597	0.19475	0.00054
15		599 °C	596	0.00129	0.00008
16		683 °C	597	0.01255	0.00016
17		757 °C	597	0.09251	0.00034
18		828 °C	596	0.42792	0.00120
19		829 °C	597	0.28322	0.00079
20		880 °C	597	0.45497	0.00091
21		880 °C	596	0.22146	0.00065
22		931 °C	597	0.29519	0.00084
23		931 °C	597	0.16135	0.00044
24		983 °C	594	0.33087	0.00100
25		982 °C	597	0.24134	0.00086
26		1033 °C	597	0.48307	0.00120
27		1032 °C	597	0.31685	0.00088
28		1083 °C	596	0.42424	0.00110
29		849 °C	596	0.00302	0.00012
30		962 °C	596	0.03073	0.00021
31		1052 °C	596	0.12066	0.00035
32		1133 °C	597	0.28042	0.00100
33		1133 °C	597	0.08122	0.00034
34		1183 °C	597	0.11289	0.00046
35		1183 °C	597	0.21145	0.00065
36		1232 °C	597	0.53696	0.00120
37		1231 °C	596	0.48445	0.00120
38		1281 °C	596	0.13145	0.00042
39		1281 °C	597	0.04131	0.00026
40		1330 °C	596	0.07830	0.00036
41		1427 °C	597	0.02244	0.00018

BV-8k-1

1		407 °C	597	0.00010	0.00007
2	X	460 °C	596	0.00021	0.00007
3	X	460 °C	597	0.00041	0.00006
4	X	513 °C	597	0.00231	0.00012
5	X	514 °C	596	0.00160	0.00008
6	X	567 °C	596	0.00804	0.00012
7	X	567 °C	597	0.00517	0.00010
8	X	620 °C	597	0.02254	0.00019
9	X	619 °C	597	0.01515	0.00015
10	X	672 °C	596	0.04680	0.00025
11	X	672 °C	596	0.02677	0.00018
12		724 °C	597	0.06055	0.00032
13		724 °C	596	0.02861	0.00021
14		778 °C	594	0.05222	0.00028
15		777 °C	597	0.02104	0.00023

#	E_a	Temp (°C)	Time (s)	^{39}Ar ± 1σ (nA)	^{37}Ar ± 1σ (nA)
16		599 °C	597	0.00017	0.00007
17		683 °C	596	0.00149	0.00009
18		755 °C	597	0.00795	0.00012
19		829 °C	596	0.02865	0.00023
20		828 °C	596	0.01691	0.00020
21		880 °C	596	0.03286	0.00025
22		880 °C	596	0.02107	0.00021
23		931 °C	597	0.04151	0.00027
24		932 °C	596	0.02856	0.00020
25		982 °C	597	0.05965	0.00033
26		982 °C	597	0.04223	0.00027
27		1033 °C	597	0.09155	0.00037
28		1033 °C	596	0.06407	0.00033
29		1083 °C	596	0.25441	0.00086
30		850 °C	596	0.00880	0.00019
31		962 °C	596	0.02993	0.00018
32		1053 °C	597	0.09080	0.00035
33		1133 °C	597	2.81072	0.00831
34		1133 °C	597	2.40416	0.00531
35		1183 °C	596	4.02924	0.01501
36		1183 °C	597	1.03744	0.00211
37		1232 °C	597	0.40943	0.00120
38		1232 °C	596	0.12963	0.00047
39		1281 °C	597	0.18431	0.00050
40		1281 °C	596	0.14887	0.00044
41		1330 °C	597	0.00236	0.00009
42		1427 °C	597	0.01714	0.00016

BV-8k-2

1	X	460 °C	596	0.00009	0.00007
2	X	460 °C	596	0.00025	0.00006
3	X	514 °C	596	0.00176	0.00009
4	X	513 °C	596	0.00114	0.00007
5	X	567 °C	596	0.00573	0.00010
6	X	567 °C	596	0.00348	0.00011
7	X	620 °C	597	0.01609	0.00014
8	X	620 °C	597	0.00943	0.00017
9	X	673 °C	596	0.02813	0.00022
10	X	672 °C	596	0.01497	0.00014
11		724 °C	596	0.02987	0.00018
12		725 °C	597	0.01252	0.00018
13		777 °C	597	0.02583	0.00018
14		777 °C	597	0.01282	0.00017
15		598 °C	596	0.00029	0.00008
16		682 °C	596	0.00104	0.00007
17		757 °C	597	0.00430	0.00010
18		829 °C	597	0.01766	0.00017

#	E_a	Temp (°C)	Time (s)	^{39}Ar ± 1σ (nA)	^{37}Ar ± 1σ (nA)
19		829 °C	596	0.01094 0.00017	
20		880 °C	596	0.02293 0.00023	
21		880 °C	597	0.01468 0.00015	
22		931 °C	597	0.03065 0.00024	
23		931 °C	597	0.02109 0.00018	
24		982 °C	597	0.04374 0.00029	
25		982 °C	597	0.03015 0.00024	
26		1033 °C	597	0.06108 0.00032	
27		1033 °C	596	0.04170 0.00026	
28		1083 °C	597	0.24897 0.00073	
29		850 °C	596	0.01051 0.00017	
30		962 °C	596	0.03881 0.00025	
31		1053 °C	597	0.11156 0.00040	
32		1133 °C	597	4.09570 0.00851	
33		1133 °C	597	1.83501 0.00561	
34		1183 °C	597	0.76923 0.00150	
35		1182 °C	597	0.39696 0.00121	
36		1232 °C	597	0.68536 0.00150	
37		1232 °C	596	0.21641 0.00087	
38		1280 °C	596	0.07058 0.00035	
39		1281 °C	597	0.03836 0.00027	
40		1330 °C	596	0.01659 0.00016	
41		1426 °C	597	0.00067 0.00008	

BV-8k-3

1		460 °C	597	0.00032 0.00008	
2		460 °C	597	0.00005 0.00008	
3	X	513 °C	596	0.00094 0.00005	
4	X	513 °C	597	0.00082 0.00013	
5	X	567 °C	597	0.00276 0.00012	
6	X	567 °C	597	0.00213 0.00008	
7	X	620 °C	596	0.00778 0.00015	
8	X	620 °C	596	0.00493 0.00009	
9	X	673 °C	596	0.01778 0.00028	
10	X	672 °C	596	0.00980 0.00014	
11		725 °C	596	0.02717 0.00021	
12		726 °C	597	0.01578 0.00015	
13		777 °C	596	0.03868 0.00024	
14		776 °C	597	0.02082 0.00026	
15		599 °C	594	0.00046 0.00006	
16		682 °C	597	0.00140 0.00007	
17		757 °C	596	0.00852 0.00012	
18		829 °C	596	0.04141 0.00027	
19		829 °C	597	0.02730 0.00028	
20		881 °C	596	0.05850 0.00033	
21		880 °C	596	0.03846 0.00027	
22		931 °C	596	0.06874 0.00033	

#	E_a	Temp (°C)	Time (s)	$^{39}Ar \pm 1\sigma$ (nA)	$^{37}Ar \pm 1\sigma$ (nA)
23		931 °C	597	0.04343 0.00027	
24		982 °C	596	0.07807 0.00036	
25		982 °C	597	0.04803 0.00032	
26		1033 °C	597	0.10519 0.00047	
27		1033 °C	596	0.06956 0.00038	
28		1083 °C	597	0.19659 0.00093	
29		850 °C	596	0.00477 0.00012	
30		962 °C	596	0.01587 0.00015	
31		1053 °C	596	0.05576 0.00029	
32		1133 °C	596	0.48486 0.00130	
33		1133 °C	596	0.33909 0.00074	
34		1182 °C	596	1.06803 0.00220	
35		1183 °C	597	0.49195 0.00170	
36		1231 °C	596	0.21324 0.00077	
37		1232 °C	596	0.07310 0.00037	
38		1281 °C	597	0.08072 0.00040	
39		1281 °C	597	0.06423 0.00036	
40		1330 °C	597	0.02352 0.00022	

BV-8k-4

1		410 °C	597	0.00009 0.00010	
2		410 °C	597	0.00028 0.00010	
3	X	464 °C	596	0.00024 0.00010	
4	X	464 °C	597	0.00023 0.00010	
5	X	517 °C	596	0.00123 0.00011	
6	X	517 °C	594	0.00086 0.00011	
7	X	571 °C	596	0.00315 0.00009	
8	X	570 °C	597	0.00162 0.00010	
9	X	624 °C	596	0.00661 0.00011	
10	X	623 °C	596	0.00379 0.00010	
11		676 °C	596	0.01279 0.00012	
12		676 °C	596	0.00494 0.00009	
13		728 °C	596	0.01415 0.00012	
14		728 °C	597	0.00802 0.00010	
15		780 °C	596	0.02247 0.00016	
16		780 °C	596	0.01131 0.00012	
17		831 °C	597	0.02223 0.00015	
18		831 °C	596	0.01089 0.00012	
19		984 °C	597	0.05675 0.00024	
20		984 °C	597	0.02309 0.00014	
21		1034 °C	597	0.04691 0.00019	
22		1034 °C	596	0.03038 0.00017	
23		CO_2		1.33568 0.00180	
24		CO_2		0.68514 0.00150	
25		CO_2		0.84392 0.00120	
26		CO_2		0.02307 0.00019	
27		CO_2		0.00296 0.00018	

#	E_a	Temp (°C)	Time (s)	^{39}Ar ± 1σ (nA)	^{37}Ar ± 1σ (nA)
28		CO_2		0.00147 0.00016	
29		CO_2		0.00060 0.00014	
30		CO_2		0.00011 0.00014	
31		CO_2		-0.00011 0.00011	
32		CO_2		-0.00006 0.00013	
33		CO_2		-0.00020 0.00015	
34		CO_2		0.00004 0.00012	
35		CO_2		0.00113 0.00009	
36		CO_2		-0.00006 0.00007	
37		CO_2		-0.00013 0.00008	

FCs-1

1	X	464 °C	597	0.00033 0.00003	
2	X	464 °C	596	0.00033 0.00003	
3	X	517 °C	596	0.00157 0.00005	
4	X	518 °C	597	0.00084 0.00005	
5	X	571 °C	597	0.00414 0.00007	
6	X	570 °C	596	0.00176 0.00007	
7	X	623 °C	596	0.00787 0.00009	
8	X	623 °C	597	0.00463 0.00009	
9	X	676 °C	597	0.01895 0.00020	
10	X	676 °C	596	0.01316 0.00014	
11	X	728 °C	597	0.04390 0.00028	
12	X	728 °C	596	0.02902 0.00021	
13	X	780 °C	596	0.08856 0.00037	
14	X	780 °C	597	0.06293 0.00043	
15	X	831 °C	596	0.15735 0.00046	
16	X	831 °C	596	0.10882 0.00047	
17	X	983 °C	596	0.82648 0.00140	
18	X	984 °C	596	0.37881 0.00091	
19	X	1034 °C	597	0.50228 0.00100	
20	X	1034 °C	596	0.31744 0.00084	
21		CO_2		0.56957 0.00120	
22		CO_2		0.86971 0.00150	
23		CO_2		0.21591 0.00049	
24		CO_2		0.33824 0.00083	
25		CO_2		0.66310 0.00150	
26		CO_2		0.28461 0.00085	
27		CO_2		0.34675 0.00082	
28		CO_2		0.12643 0.00036	
29		CO_2		0.09316 0.00044	
30		CO_2		0.05391 0.00032	
31		CO_2		0.00375 0.00007	
32		CO_2		0.00037 0.00004	
33		CO_2		0.00011 0.00004	
34		CO_2		0.00000 0.00005	
35		CO_2		-0.00003 0.00004	

#	E_a	Temp (°C)	Time (s)	$^{39}Ar \pm 1\sigma$ (nA)	$^{37}Ar \pm 1\sigma$ (nA)
FCs-2					
1		406 °C	597	0.00010	0.00007
2		407 °C	597	0.00018	0.00007
3	X	460 °C	597	0.00122	0.00007
4	X	460 °C	597	0.00078	0.00008
5	X	514 °C	594	0.00384	0.00011
6	X	514 °C	596	0.00236	0.00009
7	X	567 °C	596	0.00900	0.00014
8	X	567 °C	596	0.00512	0.00011
9	X	620 °C	596	0.02112	0.00021
10	X	620 °C	597	0.01407	0.00019
11	X	672 °C	597	0.05271	0.00028
12	X	672 °C	597	0.03365	0.00029
13	X	725 °C	597	0.11203	0.00050
14	X	724 °C	597	0.07664	0.00042
15	X	777 °C	596	0.22775	0.00072
16	X	776 °C	597	0.16388	0.00051
17	X	599 °C	597	0.00102	0.00007
18	X	755 °C	596	0.07561	0.00047
19	X	829 °C	597	0.37837	0.00100
20	X	828 °C	596	0.27260	0.00093
21	X	880 °C	596	0.61047	0.00140
22	X	880 °C	596	0.41709	0.00088
23		931 °C	597	0.77657	0.00330
24		931 °C	597	0.57141	0.00130
25		982 °C	597	1.04902	0.00160
26		982 °C	596	0.75994	0.00150
27		1032 °C	597	1.25359	0.00230
28		1033 °C	596	0.90329	0.00180
29		1083 °C	596	1.75279	0.00230
30		849 °C	596	0.05204	0.00033
31		962 °C	597	0.24626	0.00087
32		1053 °C	597	0.76694	0.00160
33		1133 °C	597	2.12135	0.00230
34		1132 °C	597	1.35806	0.00190
35		1183 °C	597	4.96353	0.00390
36		1183 °C	597	1.78743	0.00270
37		1232 °C	597	0.71829	0.00180
38		1232 °C	596	0.16800	0.00067
39		1280 °C	596	0.36355	0.00130
40		1281 °C	597	0.18221	0.00064
41		1330 °C	596	1.03266	0.00340
GSs-1					
1	X	457 °C	591	0.00189	0.00007

#	E_a	Temp (°C)	Time (s)	^{39}Ar ± 1σ (nA)		^{37}Ar ± 1σ (nA)	
2	X	482 °C	593	0.00327	0.00007		
3	X	484 °C	591	0.00209	0.00007		
4	X	508 °C	594	0.00247	0.00007		
5	X	536 °C	594	0.00464	0.00008		
6	X	534 °C	591	0.00328	0.00007		
7	X	560 °C	591	0.00636	0.00007		
8	X	560 °C	593	0.00508	0.00007		
9	X	587 °C	591	0.00907	0.00008		
10		???	589	0.01718	0.00010		
11	X	637 °C	591	0.03452	0.00013		
12	X	637 °C	588	0.02820	0.00011		
13	X	664 °C	588	0.05197	0.00013		
14	X	667 °C	590	0.04058	0.00015		
15	X	691 °C	590	0.06716	0.00020		
16	X	691 °C	592	0.05053	0.00016		
17		646 °C	592	0.00796	0.00008		
18		569 °C	2979	0.00227	0.00007		
19		621 °C	2995	0.01208	0.00008		
20	X	694 °C	584	0.02021	0.00010		
21	X	769 °C	595	0.15682	0.00026		
22	X	820 °C	580	0.39378	0.00047		
23	X	743 °C	595	0.04460	0.00013		
24	X	873 °C	595	0.82093	0.00120		
25	X	871 °C	590	0.52445	0.00120		
26	X	921 °C	591	0.93415	0.00130		
27	X	925 °C	595	0.69357	0.00130		
28	X	880 °C	587	0.25734	0.00048		
29	X	980 °C	589	1.21655	0.00120		
30	X	1023 °C	578	2.01898	0.00170		
31	X	1027 °C	590	1.62815	0.00130		
32	X	1080 °C	589	2.30529	0.00250		
33	X	1021 °C	588	0.69503	0.00120		
34		1128 °C	580	1.74574	0.00170		
35		1223 °C	595	1.52144	0.00110		
36		1224 °C	592	0.84885	0.00140		
37		1321 °C	589	2.77622	0.00330		
38		1196 °C	590	0.36374	0.00074		
39		1351 °C	590	0.38760	0.00069		
40		1351 °C	590	0.38760	0.00069		

ECCa-1

1	X	463 °C	2996	0.00099	0.00005	0.00038	0.00003
2	X	463 °C	2997	0.00058	0.00005	0.00018	0.00003
3	X	517 °C	2996	0.00367	0.00008	0.00119	0.00004
4	X	517 °C	2997	0.00240	0.00006	0.00080	0.00003
5	X	570 °C	2997	0.01745	0.00012	0.00541	0.00006
6	X	569 °C	2997	0.01245	0.00011	0.00388	0.00006

#	E_a	Temp (°C)	Time (s)	^{39}Ar ± 1σ (nA)		^{37}Ar ± 1σ (nA)	
7	X	622 °C	1997	0.02811	0.00017	0.00921	0.00008
8	X	622 °C	1996	0.01172	0.00012	0.00400	0.00005
9		674 °C	1996	0.02519	0.00018	0.00811	0.00009
10		674 °C	1997	0.01009	0.00011	0.00325	0.00005
11		726 °C	1997	0.02120	0.00017	0.00679	0.00008
12		727 °C	1996	0.01171	0.00010	0.00380	0.00006
13		779 °C	1997	0.03738	0.00023	0.01221	0.00010
14		779 °C	1997	0.02906	0.00017	0.00956	0.00008
15		829 °C	996	0.04442	0.00025	0.01472	0.00012
16		830 °C	997	0.03449	0.00023	0.01142	0.00010
17		881 °C	997	0.09508	0.00041	0.03104	0.00036
18		881 °C	997	0.06761	0.00028	0.02237	0.00018
19		696 °C	2996	0.00122	0.00005	0.00043	0.00004
20		696 °C	2996	0.00100	0.00006	0.00033	0.00004
21		748 °C	2997	0.00477	0.00007	0.00154	0.00005
22		748 °C	2997	0.00520	0.00008	0.00166	0.00005
23		799 °C	2996	0.02075	0.00013	0.00675	0.00006
24		799 °C	2996	0.01931	0.00013	0.00664	0.00008
25		851 °C	2996	0.06668	0.00024	0.02270	0.00012
26		851 °C	2996	0.05759	0.00025	0.01973	0.00013
27		932 °C	997	0.11334	0.00046	0.03878	0.00041
28		932 °C	997	0.09623	0.00041	0.03270	0.00025
29		983 °C	996	0.23610	0.00071	0.07943	0.00065
30		982 °C	996	0.18940	0.00072	0.06501	0.00077
31		1033 °C	996	0.38264	0.00097	0.13208	0.00095
32		1033 °C	997	0.30852	0.00078	0.10714	0.00075
33		1133 °C	997	1.03041	0.00190	0.37457	0.00275
34		1232 °C	997	2.59468	0.00450	0.91539	0.00699
35		1330 °C	997	1.32476	0.00240	0.46736	0.00306
36		1426 °C	996	0.03646	0.00034	0.01292	0.00012
37		1425 °C	997	0.00734	0.00011	0.00258	0.00007
38		1455 °C	996	0.00128	0.00006	0.00022	0.00005

ECCa-2

1	X	463 °C	2997	0.00068	0.00004	0.00022	0.00002
2	X	463 °C	2997	0.00040	0.00005	0.00016	0.00002
3	X	516 °C	2996	0.00258	0.00006	0.00069	0.00003
4	X	517 °C	2996	0.00146	0.00005	0.00054	0.00003
5	X	570 °C	2996	0.01073	0.00010	0.00312	0.00004
6	X	570 °C	2994	0.00847	0.00010	0.00262	0.00005
7	X	622 °C	1997	0.02120	0.00015	0.00634	0.00006
8	X	622 °C	1996	0.00926	0.00011	0.00303	0.00005
9		674 °C	1997	0.01867	0.00012	0.00579	0.00006
10		674 °C	1996	0.00729	0.00009	0.00218	0.00006
11		727 °C	1996	0.01426	0.00013	0.00458	0.00007
12		727 °C	1997	0.00781	0.00010	0.00253	0.00005
13		778 °C	1996	0.02298	0.00015	0.00742	0.00008

#	E_a	Temp (°C)	Time (s)	^{39}Ar ± 1σ (nA)		^{37}Ar ± 1σ (nA)	
14		778 °C	1997	0.01781	0.00012	0.00572	0.00007
15		829 °C	996	0.02715	0.00015	0.00901	0.00008
16		830 °C	997	0.02194	0.00015	0.00729	0.00007
17		881 °C	997	0.05716	0.00035	0.01904	0.00013
18		881 °C	996	0.04183	0.00023	0.01408	0.00011
19		695 °C	2997	0.00090	0.00004	0.00035	0.00004
20		696 °C	2996	0.00071	0.00004	0.00031	0.00003
21		748 °C	2997	0.00341	0.00007	0.00121	0.00004
22		747 °C	2997	0.00353	0.00007	0.00116	0.00004
23		799 °C	2997	0.01374	0.00014	0.00437	0.00007
24		799 °C	2997	0.01267	0.00014	0.00439	0.00007
25		851 °C	2997	0.04221	0.00021	0.01462	0.00010
26		851 °C	2996	0.03674	0.00023	0.01296	0.00010
27		932 °C	996	0.06742	0.00035	0.02267	0.00017
28		932 °C	997	0.05855	0.00034	0.01936	0.00013
29		983 °C	996	0.13745	0.00047	0.04741	0.00038
30		983 °C	997	0.11934	0.00058	0.04011	0.00033
31		1033 °C	997	0.23533	0.00060	0.08180	0.00083
32		1033 °C	997	0.18218	0.00056	0.06238	0.00084
33		1133 °C	996	0.62358	0.00180	0.22540	0.00157
34		1232 °C	996	2.61459	0.00480	0.93934	0.00669
35		1330 °C	997	3.46775	0.00420	1.21403	0.00765
36		1427 °C	997	1.19398	0.00240	0.42303	0.00197
37		1427 °C	997	0.04444	0.00040	0.01555	0.00014
38		1474 °C	997	0.00340	0.00008	0.00101	0.00006

ECCa-3

1	X	463 °C	2997	0.00057	0.00004	0.00014	0.00003
2	X	463 °C	2996	0.00032	0.00004	0.00014	0.00002
3	X	516 °C	2997	0.00252	0.00007	0.00072	0.00003
4	X	516 °C	2996	0.00179	0.00005	0.00051	0.00003
5	X	570 °C	2996	0.01249	0.00011	0.00363	0.00006
6	X	570 °C	2997	0.00953	0.00013	0.00270	0.00005
7	X	622 °C	1997	0.02218	0.00020	0.00685	0.00008
8	X	622 °C	1997	0.01101	0.00012	0.00338	0.00005
9		674 °C	1997	0.02560	0.00018	0.00820	0.00009
10		675 °C	1997	0.01028	0.00010	0.00332	0.00005
11		726 °C	1996	0.02073	0.00018	0.00674	0.00008
12		727 °C	1996	0.01048	0.00011	0.00355	0.00005
13		779 °C	1997	0.03221	0.00019	0.01079	0.00009
14		779 °C	1997	0.02402	0.00016	0.00810	0.00009
15		830 °C	996	0.03788	0.00024	0.01245	0.00008
16		830 °C	997	0.02918	0.00019	0.00971	0.00008
17		881 °C	997	0.07717	0.00044	0.02674	0.00028
18		881 °C	996	0.05803	0.00030	0.01953	0.00013
19		696 °C	2996	0.00103	0.00005	0.00035	0.00003
20		696 °C	2997	0.00090	0.00004	0.00025	0.00003

#	E_a	Temp (°C)	Time (s)	^{39}Ar ± 1σ (nA)		^{37}Ar ± 1σ (nA)	
21		747 °C	2996	0.00452	0.00007	0.00149	0.00005
22		748 °C	2996	0.00453	0.00007	0.00146	0.00005
23		799 °C	2996	0.01864	0.00013	0.00609	0.00008
24		799 °C	2996	0.01727	0.00015	0.00584	0.00007
25		851 °C	2997	0.06286	0.00030	0.02134	0.00014
26		851 °C	2997	0.05448	0.00030	0.01855	0.00012
27		932 °C	996	0.10573	0.00048	0.03510	0.00038
28		932 °C	997	0.08807	0.00043	0.02984	0.00038
29		982 °C	996	0.22493	0.00075	0.07510	0.00059
30		983 °C	996	0.20184	0.00061	0.06728	0.00056
31		1033 °C	996	0.43637	0.00100	0.15436	0.00083
32		1033 °C	997	0.33726	0.00100	0.11550	0.00099
33		1133 °C	997	1.12218	0.00230	0.40794	0.00218
34		1232 °C	996	2.50526	0.00510	0.91041	0.00882
35		1330 °C	996	1.53275	0.00220	0.53273	0.00367
36		1426 °C	997	0.14997	0.00059	0.05801	0.00062
37		1426 °C	997	0.00349	0.00010	0.00119	0.00006
38		1475 °C	996	0.00061	0.00005	0.00009	0.00005
ECCa-4							
1	X	512 °C	595	0.00111	0.00004	0.00042	0.00006
2	X	511 °C	595	0.00062	0.00003	0.00023	0.00005
3	X	565 °C	596	0.00306	0.00005	0.00091	0.00009
4	X	564 °C	592	0.00227	0.00004	0.00081	0.00006
5	X	617 °C	595	0.01046	0.00006	0.00359	0.00007
6	X	616 °C	595	0.00533	0.00005	0.00165	0.00007
7		669 °C	596	0.01229	0.00009	0.00423	0.00008
8		668 °C	595	0.00534	0.00006	0.00194	0.00005
9		720 °C	596	0.01068	0.00006	0.00367	0.00006
10		720 °C	596	0.00444	0.00005	0.00174	0.00006
11		773 °C	595	0.01033	0.00006	0.00367	0.00010
12		771 °C	595	0.00647	0.00006	0.00226	0.00007
13		828 °C	592	0.01926	0.00009	0.00663	0.00008
14		822 °C	595	0.01226	0.00011	0.00429	0.00007
15		873 °C	596	0.03484	0.00009	0.01248	0.00010
16		878 °C	595	0.02365	0.00010	0.00777	0.00019
17		925 °C	595	0.05094	0.00046	0.01719	0.00015
18		925 °C	595	0.04055	0.00011	0.01390	0.00016
19		977 °C	595	0.08127	0.00021	0.02972	0.00037
20		978 °C	595	0.06366	0.00015	0.02300	0.00019
21		1027 °C	595	0.13797	0.00037	0.04785	0.00044
22		1029 °C	596	0.10274	0.00031	0.03566	0.00047
23		1079 °C	595	0.17460	0.00041	0.05994	0.00051
24		1073 °C	593	0.12551	0.00035	0.04418	0.00048
25		1128 °C	595	0.21809	0.00098	0.07836	0.00060
26		1127 °C	596	0.17706	0.00041	0.06226	0.00061
27		1324 °C	595	3.34711	0.00410	1.15296	0.00944

#	E_a	Temp (°C)	Time (s)	^{39}Ar ± 1σ (nA)		^{37}Ar ± 1σ (nA)	
28		1323 °C	595	0.00843	0.00014	0.00294	0.00021
29		1324 °C	595	0.00085	0.00009	0.00001	0.00020
ECCa-5							
1		450 °C	176	0.00099	0.00010	0.00170	0.00038
2		550 °C	180	0.00279	0.00008	0.00177	0.00038
3		650 °C	180	0.02148	0.00015	0.00751	0.00041
4		750 °C	180	0.08919	0.00027	0.02807	0.00050
5		850 °C	180	0.10682	0.00026	0.03567	0.00060
6		950 °C	180	0.19046	0.00034	0.06332	0.00080
7		550 °C	2980	0.00024	0.00004	0.00008	0.00035
8		575 °C	2980	0.00031	0.00004	---	---
9		600 °C	2980	0.00038	0.00004	0.00002	0.00036
10		625 °C	2980	0.00051	0.00004	---	---
11		650 °C	2980	0.00084	0.00005	0.00066	0.00034
12		675 °C	2980	0.00126	0.00005	0.00024	0.00034
13		700 °C	2980	0.00265	0.00007	0.00078	0.00034
14		725 °C	2980	0.00533	0.00009	0.00071	0.00036
15		750 °C	2980	0.01116	0.00009	0.00334	0.00037
16		775 °C	2980	0.02189	0.00014	0.00730	0.00040
17		850 °C	580	0.02923	0.00016	0.01045	0.00040
18		900 °C	580	0.08407	0.00023	0.02746	0.00050
19		950 °C	580	0.17668	0.00051	0.05908	0.00071
20		1000 °C	580	0.35273	0.00080	0.12093	0.00104
21		1050 °C	580	0.75449	0.00150	0.27668	0.00229
22		1100 °C	580	1.77169	0.00300	0.62842	0.00370
23		1150 °C	580	0.68020	0.00130	0.27101	0.00254
24		CO_2		2.24060	0.00310	0.77961	0.00478
25		CO_2		2.45407	0.00381	0.83748	0.00907
26		CO_2		0.20413	0.00049	0.06915	0.00103
27		CO_2		0.31204	0.00078	0.10622	0.00124
GRAp-1							
1		464 °C	596			0.03280	0.00016
2		464 °C	594			0.01620	0.00019
3		517 °C	595	0.00007	0.00004	0.07824	0.00021
4		518 °C	596	0.00005	0.00005	0.04145	0.00019
5	X	571 °C	596	0.00021	0.00005	0.17356	0.00019
6	X	571 °C	596	0.00002	0.00005	0.08797	0.00021
7	X	623 °C	596	0.00035	0.00006	0.32070	0.00019
8	X	623 °C	596	0.00020	0.00006	0.17638	0.00024
9	X	676 °C	596	0.00074	0.00005	0.64898	0.00025
10	X	676 °C	596	0.00042	0.00006	0.40517	0.00026
11	X	728 °C	596	0.00213	0.00006	1.42335	0.00026
12	X	728 °C	596	0.00092	0.00006	0.86153	0.00027
13	X	780 °C	597	0.00281	0.00008	2.45769	0.00028

#	E_a	Temp (°C)	Time (s)	^{39}Ar ± 1σ (nA)		^{37}Ar ± 1σ (nA)	
14	X	780 °C	596	0.00157	0.00007	1.40032	0.00025
15	X	831 °C	596	0.00398	0.00013	3.65259	0.00051
16	X	831 °C	596	0.00268	0.00010	2.32371	0.00032
17	X	882 °C	596	0.00656	0.00013	5.69492	0.00040
18	X	883 °C	597	0.00489	0.00013	3.98189	0.00046
19		933 °C	596	0.01028	0.00019	8.47431	0.00070
20		933 °C	596	0.00565	0.00013	4.73228	0.00041
21		984 °C	596	0.00897	0.00014	7.82062	0.00048
22		984 °C	595	0.00439	0.00014	3.84121	0.00043
23		1034 °C	597	0.01637	0.00022	9.85342	0.00052
24		1034 °C	596	0.00487	0.00014	4.14033	0.00040
25		1084 °C	594	0.00832	0.00014	6.77068	0.00051
26		1084 °C	596	0.00370	0.00011	3.22509	0.00040
27		1133 °C	596	0.02773	0.00030	23.41318	0.00111
28		1134 °C	596	0.00812	0.00021	6.89871	0.00062
29		1184 °C	596	0.01771	0.00018	15.01148	0.00061
30		1183 °C	596	0.01090	0.00020	9.02487	0.00057
31		1233 °C	597	0.02057	0.00019	17.30948	0.00066
32		1233 °C	596	0.00986	0.00017	8.12548	0.00054
33		1282 °C	597	0.01158	0.00015	9.73264	0.00053
34		1282 °C	596	0.00173	0.00006	1.35196	0.00030
35		1331 °C	596	0.00022	0.00005	0.04554	0.00027
36		1331 °C	597	-0.00008	0.00006	0.02310	0.00033
37		1380 °C	300	-0.00005	0.00005	0.02966	0.00023
38		1381 °C	300	0.00031	0.00007	0.01397	0.00030
39		1429 °C	200	0.00003	0.00006	0.01954	0.00026

ML-15p-1

1		459 °C	596	0.00568	0.00007	0.00124	0.00010
2		459 °C	595	0.00276	0.00006	0.00062	0.00008
3		512 °C	595	0.00645	0.00008	0.00127	0.00006
4		512 °C	596	0.00337	0.00005	0.00054	0.00006
5		565 °C	595	0.00703	0.00010	0.00154	0.00006
6		565 °C	595	0.00391	0.00008	0.00132	0.00015
7		615 °C	595	0.00863	0.00009	0.00455	0.00012
8		616 °C	595	0.00507	0.00005	0.00317	0.00009
9		667 °C	595	0.01314	0.00006	0.01390	0.00022
10		667 °C	595	0.00750	0.00006	0.00860	0.00008
11		720 °C	596	0.01682	0.00010	0.02296	0.00023
12		723 °C	596	0.00793	0.00008	0.01074	0.00010
13		771 °C	596	0.01710	0.00011	0.02601	0.00026
14		775 °C	594	0.00919	0.00007	0.01407	0.00018
15	X	824 °C	596	0.02229	0.00015	0.03616	0.00025
16	X	825 °C	595	0.01359	0.00007	0.02199	0.00015
17	X	873 °C	596	0.03138	0.00016	0.05138	0.00039
18	X	877 °C	595	0.02350	0.00010	0.04466	0.00066
19	X	928 °C	596	0.06104	0.00014	0.10934	0.00070

#	E_a	Temp (°C)	Time (s)	^{39}Ar ± 1σ (nA)		^{37}Ar ± 1σ (nA)	
20	X	925 °C	596	0.06270	0.00022	0.10750	0.00076
21	X	976 °C	595	0.16387	0.00036	0.28100	0.00083
22	X	977 °C	595	0.11492	0.00016	0.20028	0.00099
23	X	1026 °C	597	0.19527	0.00056	0.34712	0.00407
24	X	1029 °C	596	0.13582	0.00040	0.23220	0.00108
25	X	1078 °C	596	0.21481	0.00050	0.38266	0.00305
26	X	1078 °C	596	0.15032	0.00029	0.26244	0.00157
27		1130 °C	595	0.22110	0.00049	0.36667	0.00197
28		1130 °C	596	0.14173	0.00033	0.24577	0.00150
29		1325 °C	594	2.28140	0.00180	3.95917	0.01397
30		1319 °C	595	0.03235	0.00013	0.05483	0.00053
31		???	595	0.00264	0.00009	0.00375	0.00021

ML-15p-2

1		457 °C	594	0.00061	0.00007	0.00035	0.00191
2		???	594	0.00019	0.00006	0.00042	0.00191
3		483 °C	592	0.00039	0.00006	0.00066	0.00193
4		484 °C	594	0.00027	0.00006	0.00050	0.00194
5		507 °C	589	0.00045	0.00006	0.00055	0.00195
6		509 °C	595	0.00029	0.00006	0.00043	0.00196
7		534 °C	595	0.00066	0.00006	0.00081	0.00197
8		535 °C	584	0.00045	0.00006	0.00054	0.00198
9		562 °C	587	0.00082	0.00006	0.00107	0.00199
10		560 °C	590	0.00062	0.00006	0.00063	0.00200
11		587 °C	588	0.00141	0.00007	0.00180	0.00201
12		588 °C	590	0.00102	0.00007	0.00115	0.00203
13		617 °C	584	0.00189	0.00007	0.00312	0.00205
14		639 °C	587	0.00388	0.00007	0.00564	0.00206
15		638 °C	594	0.00317	0.00007	0.00474	0.00207
16		666 °C	585	0.00582	0.00007	0.00887	0.00209
17		600 °C	584	0.00047	0.00006	0.00024	0.00210
18		694 °C	595	0.00809	0.00008	0.01267	0.00212
19		691 °C	589	0.00474	0.00007	0.00726	0.00213
20		724 °C	584	0.00689	0.00008	0.01078	0.00214
21		718 °C	596	0.00479	0.00007	0.00727	0.00215
22		516 °C	2989	0.00007	0.00006	0.00000	0.00217
23		569 °C	2995	0.00028	0.00007	0.00000	0.00219
24		621 °C	2989	0.00061	0.00006	0.00000	0.00220
25		674 °C	2995	0.00325	0.00007	0.00465	0.00222
26		768 °C	584	0.01080	0.00008	0.01773	0.00223
27		771 °C	590	0.00777	0.00008	0.01248	0.00225
28	X	822 °C	583	0.02071	0.00010	0.03447	0.00227
29	X	820 °C	595	0.01376	0.00010	0.02296	0.00228
30	X	875 °C	595	0.03318	0.00013	0.05607	0.00231
31		791 °C	595	0.00280	0.00007	0.00385	0.00231
32	X	922 °C	594	0.07122	0.00018	0.12312	0.00235
33	X	921 °C	595	0.06700	0.00015	0.11578	0.00236

#	E_a	Temp (°C)	Time (s)	^{39}Ar ± 1σ (nA)		^{37}Ar ± 1σ (nA)	
34	X	977 °C	591	0.18424	0.00026	0.31927	0.00248
35	X	977 °C	577	0.13519	0.00023	0.23768	0.00244
36	X	1024 °C	595	0.25290	0.00056	0.43310	0.00247
37	X	1024 °C	590	0.19199	0.00029	0.33047	0.00248
38	X	1078 °C	589	0.31433	0.00073	0.54066	0.00258
39	X	1076 °C	592	0.22089	0.00033	0.38019	0.00254
40	X	1127 °C	589	0.31197	0.00062	0.53432	0.00262
41	X	1129 °C	590	0.22315	0.00038	0.38549	0.00261
42		1226 °C	584	1.76929	0.00200	3.11963	0.00463
XTALp-1 (E_a for this plagioclase based on ^{39}Ar due Ca zoning)							
1	X	464 °C	597	0.00012	0.00002	0.00024	0.00010
2	X	464 °C	597	0.00006	0.00002	---	---
3	X	518 °C	596	0.00052	0.00003	0.00070	0.00012
4	X	571 °C	596	0.00065	0.00004	0.00136	0.00013
5	X	570 °C	597	0.00031	0.00002	0.00101	0.00020
6	X	624 °C	597	0.00099	0.00003	0.00272	0.00015
7	X	623 °C	596	0.00056	0.00004	0.00198	0.00013
8	X	728 °C	596	0.00656	0.00010	0.02969	0.00062
9	X	728 °C	597	0.00269	0.00008	0.01454	0.00024
10	X	831 °C	596	0.02344	0.00021	0.18106	0.00265
11	X	832 °C	597	0.01065	0.00011	0.08150	0.00128
12	X	933 °C	597	0.04837	0.00032	0.45036	0.00353
13	X	933 °C	597	0.01775	0.00018	0.14466	0.00196
14	X	983 °C	596	0.03732	0.00023	0.32953	0.00550
15	X	984 °C	596	0.02624	0.00021	0.21646	0.00472
16	X	1034 °C	597	0.04538	0.00031	0.37657	0.00266
17	X	1034 °C	597	0.02642	0.00024	0.22344	0.00374
18		CO_2		0.00164	0.00003	0.01430	0.00032
19		CO_2		0.00570	0.00010	0.05226	0.00116
20		CO_2		0.02764	0.00023	0.23762	0.00477
21		CO_2		0.00712	0.00010	0.06311	0.00102
22		CO_2		0.01669	0.00013	0.14094	0.00232
23		CO_2		0.04010	0.00022	0.38140	0.00607
24		CO_2		0.05476	0.00030	0.49157	0.00463
25		CO_2		0.01903	0.00014	0.17334	0.00137
26		CO_2		0.02561	0.00018	0.24232	0.00464
27		CO_2		0.00911	0.00011	0.08196	0.00160
28		CO_2		0.01016	0.00012	0.08492	0.00114
29		CO_2		0.00400	0.00008	0.03623	0.00107
30		CO_2		0.00171	0.00005	0.01419	0.00031
31		CO_2		0.00088	0.00005	0.00713	0.00024
32		CO_2		0.00050	0.00003	0.00569	0.00027
FCp-1							
1		???	593	0.00602	0.00024	0.00241	0.00055

#	E_a	Temp (°C)	Time (s)	^{39}Ar ± 1σ (nA)		^{37}Ar ± 1σ (nA)	
2	X	617 °C	595	0.01235	0.00010	0.00665	0.00013
3	X	617 °C	595	0.00634	0.00006	0.00437	0.00010
4	X	670 °C	595	0.01404	0.00014	0.01404	0.00017
5	X	669 °C	596	0.00731	0.00005	0.01030	0.00008
6	X	719 °C	596	0.01528	0.00006	0.03094	0.00029
7	X	720 °C	596	0.00839	0.00006	0.02111	0.00013
8		775 °C	596	0.01806	0.00008	0.05986	0.00082
9		772 °C	596	0.01128	0.00006	0.03610	0.00029
10		826 °C	595	0.02289	0.00009	0.08147	0.00112
11		822 °C	595	0.01593	0.00013	0.05014	0.00036
12		875 °C	596	0.02877	0.00008	0.09589	0.00114
13		876 °C	596	0.01902	0.00008	0.06331	0.00060
14		924 °C	596	0.03092	0.00015	0.10576	0.00151
15		927 °C	595	0.01939	0.00012	0.06172	0.00061
16		975 °C	595	0.03219	0.00014	0.10510	0.00077
17		978 °C	596	0.02481	0.00011	0.08021	0.00068
18		1027 °C	595	0.05021	0.00016	0.16314	0.00086
19		1027 °C	595	0.03720	0.00013	0.11764	0.00099
20		1079 °C	596	0.05400	0.00019	0.16912	0.00078
21		1080 °C	595	0.03471	0.00026	0.10654	0.00122
22		1130 °C	595	0.05179	0.00022	0.16671	0.00142
23		1127 °C	595	0.03403	0.00014	0.10736	0.00089
24		1327 °C	595	0.47784	0.00058	1.44798	0.00910
25		1325 °C	594	-0.00017	0.00008	-0.00007	0.00020
26		1323 °C	595	0.00033	0.00009	-0.00005	0.00020

PR-92p-1

1		457 °C	596	0.00000	0.00006	0.00020	0.00191
2		456 °C	589	0.00033	0.00006	0.00065	0.00192
3	X	483 °C	588	0.00038	0.00006	0.00153	0.00193
4	X	482 °C	594	0.00029	0.00006	0.00089	0.00194
5	X	509 °C	592	0.00052	0.00006	0.00185	0.00195
6	X	509 °C	591	0.00039	0.00006	0.00145	0.00196
7	X	535 °C	591	0.00078	0.00007	0.00265	0.00197
8	X	535 °C	594	0.00060	0.00006	0.00213	0.00198
9	X	560 °C	588	0.00111	0.00006	0.00424	0.00200
10	X	560 °C	594	0.00093	0.00006	0.00323	0.00201
11	X	588 °C	587	0.00170	0.00006	0.00635	0.00202
12	X	587 °C	595	0.00131	0.00006	0.00524	0.00203
13	X	614 °C	585	0.00222	0.00007	0.00952	0.00204
14		612 °C	582	0.00000	0.00006	0.00000	0.00205
15		639 °C	593	0.00299	0.00006	0.01249	0.00207
16		638 °C	591	0.00222	0.00007	0.01011	0.00208
17		666 °C	594	0.00389	0.00007	0.01682	0.00210
18		666 °C	590	0.00291	0.00007	0.01346	0.00212
19		691 °C	590	0.00454	0.00007	0.02060	0.00212
20		692 °C	594	0.00364	0.00007	0.01651	0.00213

#	E_a	Temp (°C)	Time (s)	^{39}Ar ± 1σ (nA)		^{37}Ar ± 1σ (nA)	
21		718 °C	596	0.00554	0.00007	0.02504	0.00215
22		720 °C	582	0.00439	0.00007	0.01924	0.00217
23		768 °C	595	0.01053	0.00008	0.04971	0.00225
24		773 °C	583	0.00786	0.00007	0.03669	0.00229
25		743 °C	596	0.00345	0.00007	0.01507	0.00227
26		827 °C	583	0.01491	0.00009	0.07054	0.00230
27		787 °C	583	0.00567	0.00010	0.02447	0.00230
28		870 °C	595	0.02094	0.00009	0.10043	0.00242
29		926 °C	584	0.02589	0.00016	0.11910	0.00236
30		927 °C	595	0.01393	0.00009	0.06248	0.00236
31		973 °C	590	0.01955	0.00009	0.09055	0.00238
32		975 °C	592	0.01127	0.00008	0.05284	0.00239
33		929 °C	590	0.00395	0.00009	0.01609	0.00241
34		1027 °C	595	0.03997	0.00013	0.18469	0.00247
35		971 °C	595	0.01022	0.00007	0.04807	0.00247
36		973 °C	592	0.00714	0.00008	0.03094	0.00246
37		1122 °C	593	0.04696	0.00021	0.21471	0.00256
38		1131 °C	583	0.01958	0.00009	0.09086	0.00251
39		1228 °C	583	0.16456	0.00035	0.75718	0.00330
40		1228 °C	592	0.11924	0.00030	0.54586	0.00287
41		1325 °C	591	0.24215	0.00060	1.12812	0.00402
42		1307 °C	589	0.42565	0.00060	1.94225	0.00393
43		1369 °C	595	0.06501	0.00016	0.29446	0.00287
NCp-1							
1	X	459 °C	596	0.00084	0.00006	0.00376	0.00016
2	X	459 °C	596	0.00025	0.00004	0.00111	0.00006
3	X	512 °C	595	0.00092	0.00004	0.00506	0.00007
4	X	511 °C	595	0.00043	0.00004	0.00229	0.00006
5	X	565 °C	595	0.00165	0.00005	0.00918	0.00011
6	X	564 °C	594	0.00077	0.00006	0.00571	0.00009
7	X	617 °C	595	0.00358	0.00005	0.02189	0.00014
8	X	617 °C	595	0.00205	0.00005	0.01320	0.00011
9		668 °C	596	0.00700	0.00006	0.05434	0.00074
10		668 °C	595	0.00432	0.00004	0.03391	0.00032
11		716 °C	599	---	---	0.00011	0.00004
12		720 °C	597	0.00817	0.00006	0.06907	0.00038
13		773 °C	595	0.02065	0.00009	0.18331	0.00099
14		771 °C	595	0.01303	0.00011	0.11038	0.00085
15		822 °C	595	0.03066	0.00017	0.26215	0.00162
16		823 °C	597	0.02073	0.00008	0.18607	0.00190
17		875 °C	595	0.04047	0.00023	0.34450	0.00292
18		878 °C	596	0.03015	0.00008	0.27811	0.00330
19		928 °C	596	0.04950	0.00020	0.45408	0.00184
20		925 °C	595	0.02848	0.00015	0.30219	0.00234
21		979 °C	595	0.04607	0.00012	0.42726	0.00337
22		977 °C	595	0.02902	0.00010	0.26881	0.00163

#	E_a	Temp (°C)	Time (s)	^{39}Ar ± 1σ (nA)		^{37}Ar ± 1σ (nA)	
23		689 °C	600	0.00022	0.00009	0.00168	0.00018
24		1027 °C	598	---	---	---	---
25		1031 °C	595	0.03024	0.00012	0.27792	0.00174
26		1079 °C	595	0.04943	0.00021	0.46560	0.00380
27		1080 °C	595	0.03123	0.00013	0.28809	0.00383
28		1128 °C	596	0.05102	0.00014	0.50069	0.00353
29		1127 °C	596	0.02955	0.00011	0.27292	0.00162
30		1327 °C	595	1.18658	0.00074	11.12950	0.05520
31		1323 °C	595	0.14042	0.00024	1.31942	0.00721
32		1319 °C	595	0.05423	0.00014	0.50084	0.00243

NCp-2

1	X	456 °C	587	0.00085	0.00007	0.00315	0.00191
2	X	457 °C	591	0.00021	0.00006	0.00086	0.00191
3	X	484 °C	594	0.00036	0.00006	0.00157	0.00192
4	X	482 °C	595	0.00018	0.00006	0.00094	0.00193
5	X	510 °C	594	0.00038	0.00006	0.00171	0.00195
6	X	509 °C	595	0.00024	0.00006	0.00141	0.00196
7	X	534 °C	591	0.00068	0.00006	0.00368	0.00197
8	X	534 °C	584	0.00036	0.00006	0.00249	0.00198
9	X	562 °C	590	0.00072	0.00007	0.00718	0.00199
10	X	562 °C	585	0.00053	0.00006	0.00367	0.00200
11	X	586 °C	594	0.00093	0.00006	0.00644	0.00201
12	X	586 °C	593	0.00061	0.00007	0.00494	0.00202
13	X	614 °C	594	0.00134	0.00007	0.00983	0.00204
14	X	614 °C	590	0.00106	0.00006	0.00746	0.00205
15	X	639 °C	591	0.00167	0.00007	0.01371	0.00206
16	X	643 °C	590	0.00137	0.00006	0.01155	0.00207
17		668 °C	587	0.00245	0.00007	0.02145	0.00209
18		667 °C	593	0.00198	0.00007	0.01789	0.00210
19		690 °C	589	0.00355	0.00007	0.03166	0.00212
20		690 °C	590	0.00272	0.00007	0.02495	0.00213
21		716 °C	589	0.00431	0.00007	0.04010	0.00215
22		649 °C	594	0.00050	0.00006	0.00444	0.00215
23		621 °C	2989	0.00095	0.00006	0.00845	0.00220
24		771 °C	592	0.00873	0.00007	0.08409	0.00224
25		774 °C	583	0.00630	0.00007	0.05975	0.00226
26		821 °C	590	0.01401	0.00008	0.13505	0.00229
27		820 °C	594	0.00953	0.00008	0.09260	0.00230
28		877 °C	589	0.01743	0.00009	0.16966	0.00234
29		869 °C	592	0.01125	0.00008	0.10741	0.00234
30		925 °C	589	0.01697	0.00008	0.16575	0.00237
31		928 °C	584	0.01037	0.00008	0.10059	0.00236
32		972 °C	589	0.01413	0.00009	0.13854	0.00237
33		976 °C	590	0.00760	0.00007	0.07317	0.00239
34		926 °C	595	0.00242	0.00007	0.02250	0.00239
35		1026 °C	589	0.00925	0.00008	0.08778	0.00243

#	E_a	Temp (°C)	Time (s)	^{39}Ar ± 1σ (nA)		^{37}Ar ± 1σ (nA)	
36		1078 °C	590	0.00917	0.00008	0.10022	0.00244
37		1079 °C	595	0.00487	0.00007	0.04386	0.00246
38		1130 °C	588	0.00768	0.00007	0.07191	0.00248
39		1123 °C	589	0.00441	0.00007	0.03826	0.00249
40		1223 °C	591	0.01857	0.00010	0.19986	0.00257
41		1224 °C	595	0.00559	0.00007	0.05081	0.00253
42		1321 °C	592	0.13193	0.00024	1.27750	0.00315
43		1323 °C	595	0.02711	0.00012	0.25419	0.00262
44		1401 °C	589	0.12627	0.00022	1.23442	0.00341
45		1312 °C	589	0.01588	0.00009	0.18358	0.00265

HMS-2p-1

1		464 °C	596	0.00109	0.00008	0.00163	0.00022
2		464 °C	596	0.00073	0.00007	0.00101	0.00019
3	X	517 °C	596	---	---	0.00456	0.00024
4	X	517 °C	596	0.00173	0.00006	0.00255	0.00024
5	X	571 °C	596	0.00579	0.00013	0.01146	0.00032
6	X	571 °C	596	0.00322	0.00008	0.00725	0.00026
7	X	623 °C	597	0.01080	0.00011	0.02719	0.00037
8	X	624 °C	594	0.00670	0.00012	0.01661	0.00035
9	X	676 °C	596	0.02486	0.00017	0.05520	0.00065
10	X	676 °C	596	0.01214	0.00012	0.03147	0.00042
11	X	728 °C	596	0.03724	0.00020	0.10397	0.00085
12	X	728 °C	596	0.02413	0.00020	0.08193	0.00075
13	X	780 °C	596	0.07808	0.00033	0.23919	0.00194
14	X	780 °C	596	0.05827	0.00022	0.17041	0.00112
15	X	831 °C	597	0.11375	0.00043	0.34668	0.00296
16	X	831 °C	596	0.07291	0.00031	0.22170	0.00219
17		882 °C	596	0.12996	0.00032	0.40260	0.00360
18		882 °C	596	0.09108	0.00032	0.27247	0.00202
19		933 °C	596	0.13595	0.00035	0.42270	0.00244
20		933 °C	597	0.09158	0.00034	0.28317	0.00368
21		983 °C	596	0.11297	0.00046	0.34286	0.00140
22		983 °C	597	0.07263	0.00035	0.21656	0.00186
23		1034 °C	597	0.10466	0.00041	0.32325	0.00293
24		1034 °C	596	0.06350	0.00035	0.18581	0.00142
25		1084 °C	596	0.09808	0.00037	0.29252	0.00256
26		1084 °C	596	0.05785	0.00033	0.16618	0.00123
27		1134 °C	596	0.11536	0.00037	0.35041	0.00280
28		1133 °C	596	0.05087	0.00036	0.14460	0.00120
29		1183 °C	596	0.06870	0.00030	0.19993	0.00207
30		1183 °C	596	0.04562	0.00039	0.13058	0.00102
31		1232 °C	596	0.06560	0.00033	0.18998	0.00150
32		1233 °C	597	0.03897	0.00031	0.10888	0.00109
33		1282 °C	597	0.05757	0.00034	0.16894	0.00118
34		1282 °C	596	0.03565	0.00029	0.08182	0.00093

#	E_a	Temp (°C)	Time (s)	^{39}Ar ± 1σ (nA)		^{37}Ar ± 1σ (nA)	
35		1331 °C	597	0.06566	0.00035	0.18757	0.00168
36		1331 °C	597	0.03841	0.00026	0.10572	0.00095
37		1381 °C	300	0.18114	0.00036	0.54452	0.00314
38		1379 °C	300	0.13679	0.00039	0.41807	0.00361
39		1431 °C	200	0.15641	0.00048	0.47671	0.00339

SURTp-1

1	X	463 °C	2997	0.00005	0.00004	0.00071	0.00003
2	X	463 °C	2997	0.00002	0.00004	0.00035	0.00003
3	X	517 °C	2996	0.00017	0.00004	0.00214	0.00004
4	X	516 °C	2997	0.00010	0.00003	0.00113	0.00004
5	X	569 °C	2997	0.00020	0.00003	0.00504	0.00007
6	X	569 °C	2997	0.00016	0.00004	0.00222	0.00005
7	X	622 °C	1997	0.00019	0.00004	0.00580	0.00006
8	X	622 °C	1996	0.00015	0.00004	0.00355	0.00005
9		674 °C	1997	0.00038	0.00004	0.01324	0.00011
10		674 °C	1996	0.00022	0.00004	0.00697	0.00007
11		727 °C	1996	0.00064	0.00004	0.01925	0.00014
12		727 °C	1996	0.00026	0.00004	0.01010	0.00009
13		778 °C	1997	0.00106	0.00005	0.03071	0.00027
14		779 °C	1997	0.00454	0.00009	0.15267	0.00125
15		829 °C	996	0.02280	0.00013	0.80335	0.00659
16		830 °C	997	0.01130	0.00012	0.38028	0.00459
17		880 °C	996	0.02023	0.00012	0.69595	0.00539
18		881 °C	996	0.01315	0.00013	0.44179	0.00414
19		695 °C	2997	0.00034	0.00004	0.00700	0.00009
20		696 °C	2997	0.00016	0.00004	0.00605	0.00007
21		748 °C	2996	0.00103	0.00005	0.03406	0.00027
22		748 °C	2996	0.00107	0.00005	0.03428	0.00041
23		799 °C	2996	0.00368	0.00006	0.12318	0.00104
24		799 °C	2997	0.00211	0.00006	0.07034	0.00070
25		851 °C	2997	0.00358	0.00008	0.12342	0.00150
26		851 °C	2997	0.00148	0.00005	0.04743	0.00043
27		932 °C	997	0.00168	0.00006	0.05552	0.00069
28		932 °C	997	0.00084	0.00004	0.02820	0.00027
29		983 °C	997	0.00140	0.00005	0.04922	0.00062
30		983 °C	996	0.00093	0.00007	0.02629	0.00018
31		1033 °C	997	0.00138	0.00005	0.04329	0.00036
32		1033 °C	997	0.00110	0.00006	0.03246	0.00036
33		1134 °C	997	0.00292	0.00007	0.09585	0.00133
34		1233 °C	991	0.00484	0.00008	0.15151	0.00237
35		1330 °C	997	0.02033	0.00015	0.70895	0.00671
36		1426 °C	996	0.07901	0.00033	2.84925	0.00860
37		1427 °C	996	0.02028	0.00024	0.73833	0.01051
38		1417 °C	997	0.00138	0.00007	0.03178	0.00034

SURTp-2

#	E_a	Temp (°C)	Time (s)	^{39}Ar ± 1σ (nA)		^{37}Ar ± 1σ (nA)	
1	X	463 °C	2996	0.00009	0.00004	0.00082	0.00003
2	X	463 °C	2997	0.00002	0.00004	0.00056	0.00003
3	X	517 °C	2996	0.00007	0.00004	0.00331	0.00006
4	X	517 °C	2996	0.00007	0.00004	0.00174	0.00004
5	X	570 °C	2996	0.00023	0.00004	0.00760	0.00008
6	X	569 °C	2997	0.00017	0.00004	0.00347	0.00005
7	X	622 °C	1997	0.00027	0.00004	0.00874	0.00008
8	X	622 °C	1997	0.00014	0.00004	0.00512	0.00006
9		675 °C	1997	0.00054	0.00004	0.01948	0.00013
10		674 °C	1996	0.00030	0.00004	0.00978	0.00008
11		727 °C	1994	0.00081	0.00005	0.02723	0.00034
12		726 °C	1997	0.00035	0.00005	0.01386	0.00011
13		779 °C	1997	0.00093	0.00004	0.03853	0.00040
14		779 °C	1997	0.00076	0.00004	0.02334	0.00030
15		830 °C	997	0.00134	0.00005	0.04727	0.00028
16		830 °C	996	0.00343	0.00007	0.13347	0.00158
17		881 °C	997	0.01957	0.00013	0.80870	0.00617
18		881 °C	997	0.01466	0.00013	0.60474	0.00414
19		695 °C	2996	0.00034	0.00004	0.01090	0.00010
20		696 °C	2996	0.00026	0.00004	0.00951	0.00007
21		748 °C	2997	0.00126	0.00005	0.04513	0.00040
22		748 °C	2997	0.00111	0.00005	0.04371	0.00041
23		799 °C	2997	0.00455	0.00009	0.17424	0.00165
24		800 °C	2997	0.00384	0.00008	0.14946	0.00095
25		851 °C	2997	0.00958	0.00011	0.38138	0.00367
26		851 °C	2997	0.00433	0.00009	0.17257	0.00169
27		932 °C	996	0.00507	0.00008	0.19028	0.00194
28		932 °C	996	0.00238	0.00007	0.09355	0.00108
29		983 °C	995	0.00362	0.00008	0.14784	0.00135
30		983 °C	997	0.00205	0.00006	0.07309	0.00077
31		1033 °C	996	0.00283	0.00007	0.10506	0.00116
32		1033 °C	996	0.00186	0.00006	0.07142	0.00069
33		1133 °C	997	0.00495	0.00009	0.18594	0.00190
34		1232 °C	996	0.00557	0.00009	0.20548	0.00334
35		1330 °C	997	0.01093	0.00012	0.45492	0.00580
36		1427 °C	997	0.10146	0.00042	4.20091	0.02120
37		1426 °C	996	0.00368	0.00009	0.14618	0.00164
38		1473 °C	996	0.00144	0.00006	0.04207	0.00056

SURTp-3

1	X	463 °C	2997	0.00007	0.00004	0.00186	0.00004
2	X	463 °C	2996	0.00002	0.00004	0.00081	0.00003
3	X	516 °C	2997	0.00015	0.00004	0.00440	0.00005
4	X	516 °C	2997	0.00008	0.00004	0.00250	0.00005
5	X	570 °C	2997	0.00037	0.00003	0.00999	0.00009
6	X	570 °C	2997	0.00015	0.00004	0.00415	0.00006
7	X	622 °C	1997	0.00028	0.00004	0.00976	0.00010

#	E_a	Temp (°C)	Time (s)	$^{39}Ar \pm 1\sigma$ (nA)		$^{37}Ar \pm 1\sigma$ (nA)	
8	X	622 °C	1997	0.00009	0.00004	0.00545	0.00006
9		675 °C	1996	0.00044	0.00004	0.01985	0.00013
10		675 °C	1997	0.00033	0.00004	0.01058	0.00008
11		726 °C	1996	0.00092	0.00004	0.03109	0.00034
12		726 °C	1996	0.00047	0.00004	0.01735	0.00011
13		779 °C	1995	0.00147	0.00005	0.05448	0.00080
14		779 °C	1997	0.00112	0.00005	0.04253	0.00043
15		830 °C	996	0.00264	0.00006	0.11023	0.00140
16		830 °C	997	0.00820	0.00011	0.31588	0.00460
17		881 °C	997	0.02762	0.00015	1.10810	0.00540
18		881 °C	996	0.01410	0.00014	0.57510	0.00440
19		695 °C	2997	0.00016	0.00004	0.00676	0.00007
20		696 °C	2997	0.00010	0.00004	0.00585	0.00006
21		748 °C	2996	0.00086	0.00004	0.02980	0.00027
22		748 °C	2996	0.00079	0.00005	0.02860	0.00025
23		800 °C	2996	0.00323	0.00008	0.12692	0.00135
24		799 °C	2996	0.00256	0.00006	0.09872	0.00078
25		851 °C	2996	0.00640	0.00009	0.25143	0.00396
26		851 °C	2997	0.00332	0.00007	0.12630	0.00132
27		932 °C	997	0.00405	0.00007	0.15724	0.00183
28		932 °C	996	0.00222	0.00006	0.08208	0.00114
29		983 °C	996	0.00367	0.00008	0.13910	0.00170
30		983 °C	996	0.00187	0.00005	0.07839	0.00089
31		1033 °C	997	0.00317	0.00008	0.11671	0.00113
32		1033 °C	997	0.00192	0.00006	0.06783	0.00069
33		1133 °C	997	0.00501	0.00010	0.18897	0.00244
34		1232 °C	996	0.00824	0.00009	0.31257	0.00425
35		1330 °C	997	0.01349	0.00013	0.54300	0.00458
36		1427 °C	997	0.07931	0.00034	3.26952	0.01537
37		1427 °C	996	0.00117	0.00007	0.03304	0.00043
38		1475 °C	996	0.00028	0.00005	0.00454	0.00008

SURTp-4

1		464 °C	596	0.00005	0.00005	0.00096	0.00010
2		464 °C	597	0.00002	0.00005	0.00086	0.00010
3	X	517 °C	597	0.00019	0.00005	0.00410	0.00011
4	X	517 °C	597	0.00007	0.00005	0.00222	0.00011
5	X	571 °C	597	0.00043	0.00006	0.00889	0.00016
6	X	571 °C	596	0.00021	0.00006	0.00497	0.00014
7	X	624 °C	596	0.00060	0.00007	0.01793	0.00032
8	X	623 °C	596	0.00035	0.00007	0.01056	0.00029
9	X	676 °C	596	0.00107	0.00008	0.03546	0.00042
10	X	676 °C	596	0.00061	0.00007	0.02034	0.00032
11	X	728 °C	596	0.00201	0.00008	0.06694	0.00048
12	X	728 °C	596	0.00121	0.00007	0.03865	0.00039
13	X	780 °C	595	0.00315	0.00009	0.11330	0.00065
14	X	780 °C	596	0.00214	0.00008	0.07611	0.00096

#	E_a	Temp (°C)	Time (s)	^{39}Ar ± 1σ (nA)	^{37}Ar ± 1σ (nA)
15		831 °C	596	0.00678 0.00011	0.22445 0.00204
16		831 °C	596	0.00533 0.00009	0.17861 0.00155
17		882 °C	596	0.02386 0.00014	0.80892 0.00945
18		882 °C	596	0.03087 0.00022	1.08484 0.00850
19		933 °C	596	0.05180 0.00024	1.80712 0.00753
20		933 °C	597	0.02636 0.00014	0.91208 0.00971
21		983 °C	595	0.04231 0.00019	1.47322 0.01158
22		984 °C	596	0.02902 0.00017	1.00033 0.00638
23		1034 °C	594	0.03757 0.00020	1.31608 0.01089
24		1034 °C	596	0.02383 0.00018	0.83975 0.01098
25		1084 °C	597	0.03091 0.00019	1.05432 0.00832
26		1084 °C	596	0.01917 0.00018	0.66264 0.00727
27		1134 °C	596	0.02850 0.00024	1.00743 0.01692
28		1134 °C	596	0.02177 0.00022	0.71332 0.01327
29		1183 °C	597	0.03309 0.00030	1.12540 0.01437
30		1184 °C	596	0.02005 0.00018	0.63078 0.00909
31		1233 °C	596	0.02537 0.00021	0.83754 0.01269
32		1233 °C	596	0.01336 0.00019	0.38359 0.00297
33		1282 °C	596	0.01626 0.00018	0.52030 0.00816
34		1282 °C	596	0.00879 0.00011	0.26951 0.00313
35		1331 °C	596	0.05783 0.00023	1.96523 0.01014
36		1331 °C	596	0.02601 0.00016	0.87113 0.00788
37		1380 °C	596	0.08902 0.00027	3.14160 0.01963
38		1381 °C	596	0.00908 0.00011	0.28978 0.00356
39		1429 °C	596	0.00365 0.00009	0.12207 0.00152
40		1429 °C	596	0.00297 0.00008	0.09025 0.00089
41		1525 °C	597	0.00180 0.00007	0.04080 0.00056
42		1352 °C	595	0.00053 0.00007	0.00123 0.00038

SURTp-5

1		459 °C	594	0.00028 0.00005	0.00125 0.00024
2		459 °C	596	0.00002 0.00004	0.00063 0.00006
3	X	512 °C	596	0.00016 0.00004	0.00340 0.00007
4	X	511 °C	596	0.00005 0.00003	0.00156 0.00006
5	X	565 °C	595	0.00022 0.00004	0.00715 0.00013
6	X	565 °C	595	0.00014 0.00004	0.00441 0.00010
7	X	616 °C	596	0.00044 0.00007	0.01311 0.00034
8	X	616 °C	596	0.00017 0.00004	0.00613 0.00010
9	X	670 °C	595	0.00059 0.00005	0.02320 0.00026
10	X	666 °C	595	0.00040 0.00003	0.01259 0.00018
11	X	720 °C	595	0.00098 0.00005	0.03488 0.00026
12	X	720 °C	595	0.00057 0.00003	0.01806 0.00012
13	X	769 °C	596	0.00149 0.00005	0.04860 0.00028
14	X	776 °C	593	0.00100 0.00004	0.03042 0.00047
15		824 °C	595	0.01552 0.00011	0.53052 0.00383
16		822 °C	596	0.01772 0.00007	0.62374 0.00326
17		878 °C	596	0.02429 0.00010	0.86641 0.00566

#	E_a	Temp (°C)	Time (s)	^{39}Ar ± 1σ (nA)		^{37}Ar ± 1σ (nA)	
18		875 °C	596	0.01511	0.00007	0.53280	0.00201
19		921 °C	596	0.02698	0.00015	0.92146	0.00634
20		923 °C	596	0.01912	0.00009	0.64814	0.00395
21		974 °C	596	0.02705	0.00020	0.89941	0.00550
22		975 °C	595	0.01276	0.00009	0.43314	0.00132
23		689 °C	600	0.00011	0.00009	0.00101	0.00019
24		1025 °C	596	0.01210	0.00010	0.42892	0.00272
25		1027 °C	595	0.00547	0.00009	0.18885	0.00084
26		1079 °C	596	0.00733	0.00009	0.25187	0.00106
27		1079 °C	595	0.00480	0.00011	0.16090	0.00091
28		1128 °C	596	0.00785	0.00009	0.26573	0.00123
29		1129 °C	595	0.00657	0.00010	0.23116	0.00114
30		1325 °C	595	0.16070	0.00023	5.48885	0.02466
31		1321 °C	595	0.02361	0.00012	0.79420	0.00623
32		1321 °C	595	0.00980	0.00011	0.32828	0.00177
SURTp-6							
1		550 °C	180	0.00064	0.00005	0.02536	0.00057
2		650 °C	180	0.00095	0.00005	0.03135	0.00062
3		750 °C	180	0.00309	0.00007	0.09784	0.00104
4		850 °C	180	0.00434	0.00008	0.14926	0.00107
5		950 °C	180	0.05815	0.00022	2.01843	0.00994
6		CO_2		0.32340	0.00420	11.17516	0.09624
OREGp-1							
1	X	463 °C	2997	0.00015	0.00004	0.00760	0.00008
2	X	463 °C	2996	0.00006	0.00004	0.00306	0.00005
3	X	517 °C	2997	0.00039	0.00004	0.01587	0.00012
4	X	517 °C	2997	0.00019	0.00004	0.00833	0.00009
5	X	569 °C	2997	0.00089	0.00004	0.03727	0.00041
6	X	570 °C	2996	0.00049	0.00004	0.02067	0.00020
7	X	622 °C	1996	0.00137	0.00005	0.07131	0.00086
8	X	622 °C	1997	0.00122	0.00005	0.05483	0.00085
9		675 °C	1996	0.00745	0.00011	0.37867	0.00381
10		674 °C	1997	0.00753	0.00010	0.37361	0.00457
11		727 °C	1996	0.01788	0.00013	0.91369	0.00559
12		726 °C	1997	0.01096	0.00011	0.55992	0.00515
13		779 °C	1997	0.02203	0.00015	1.15891	0.00917
14		778 °C	1997	0.01533	0.00013	0.77444	0.00575
15		829 °C	997	0.01539	0.00012	0.78687	0.00734
16		830 °C	997	0.01251	0.00011	0.63222	0.00509
17		881 °C	996	0.02431	0.00016	1.25608	0.00538
18		881 °C	997	0.01830	0.00013	0.95395	0.00671
19		695 °C	2997	0.00128	0.00005	0.06374	0.00052
20		695 °C	2997	0.00118	0.00005	0.06435	0.00074
21		748 °C	2997	0.00422	0.00009	0.19834	0.00219

#	E_a	Temp (°C)	Time (s)	^{39}Ar ± 1σ (nA)		^{37}Ar ± 1σ (nA)	
22		748 °C	2997	0.00382	0.00009	0.18753	0.00178
23		799 °C	2996	0.00980	0.00010	0.49570	0.00520
24		799 °C	2997	0.00883	0.00010	0.45427	0.00610
25		851 °C	2996	0.01983	0.00014	1.03311	0.00787
26		851 °C	2997	0.01651	0.00014	0.86089	0.00655
27		932 °C	997	0.01769	0.00016	0.92680	0.00693
28		932 °C	996	0.01518	0.00013	0.77084	0.00698
29		983 °C	997	0.02558	0.00018	1.30277	0.00907
30		983 °C	996	0.02133	0.00014	1.07812	0.00766
31		1033 °C	997	0.03003	0.00016	1.55422	0.00830
32		1033 °C	997	0.02140	0.00015	1.08694	0.00537
33		1134 °C	994	0.01652	0.00016	0.80531	0.00690
34		1232 °C	996	0.01825	0.00016	0.92283	0.00515
35		1330 °C	996	0.01520	0.00013	0.76615	0.00670
36		1427 °C	997	0.04248	0.00023	2.21826	0.01992
37		1426 °C	997	0.00217	0.00006	0.09710	0.00185
38		1474 °C	997	0.00117	0.00006	0.04647	0.00050

OREGp-2

1	X	463 °C	2996	0.00009	0.00004	0.00488	0.00006
2	X	463 °C	2997	0.00010	0.00003	0.00215	0.00004
3	X	516 °C	2997	0.00031	0.00004	0.01268	0.00009
4	X	517 °C	2997	0.00018	0.00004	0.00672	0.00007
5	X	570 °C	2997	0.00078	0.00004	0.03593	0.00034
6	X	569 °C	2997	0.00051	0.00004	0.02488	0.00021
7		622 °C	1996	0.00232	0.00006	0.10670	0.00117
8		622 °C	1997	0.00198	0.00007	0.09244	0.00099
9		674 °C	1997	0.01176	0.00014	0.59113	0.00572
10		674 °C	1996	0.00897	0.00012	0.45309	0.00409
11		726 °C	1997	0.01956	0.00014	0.98334	0.00510
12		727 °C	1997	0.01236	0.00014	0.62454	0.00614
13		778 °C	1997	0.02542	0.00018	1.34468	0.01066
14		779 °C	1996	0.01773	0.00014	0.91884	0.00651
15		830 °C	996	0.01812	0.00015	0.92446	0.00810
16		829 °C	996	0.01483	0.00012	0.75752	0.00663
17		881 °C	997	0.02915	0.00016	1.49847	0.00846
18		881 °C	996	0.02311	0.00016	1.21938	0.00749
19		695 °C	2996	0.00169	0.00006	0.08411	0.00086
20		695 °C	2997	0.00171	0.00006	0.07941	0.00071
21		748 °C	2996	0.00530	0.00010	0.26256	0.00320
22		748 °C	2997	0.00493	0.00007	0.24869	0.00298
23		799 °C	2997	0.01332	0.00014	0.68053	0.00439
24		799 °C	2997	0.01229	0.00013	0.63336	0.00555
25		851 °C	2997	0.02662	0.00014	1.37920	0.00872
26		851 °C	2996	0.02257	0.00019	1.17999	0.00684
27		932 °C	997	0.02416	0.00014	1.20545	0.00272
28		932 °C	996	0.02102	0.00013	1.06893	0.00756

#	E_a	Temp (°C)	Time (s)	^{39}Ar ± 1σ (nA)		^{37}Ar ± 1σ (nA)	
29		983 °C	997	0.03472	0.00023	1.79694	0.01054
30		983 °C	997	0.02950	0.00018	1.50791	0.01031
31		1033 °C	997	0.04108	0.00020	2.10415	0.01749
32		1033 °C	997	0.02653	0.00015	1.37519	0.00746
33		1232 °C	996	0.04699	0.00017	2.46302	0.01181
34		1330 °C	996	0.04209	0.00020	2.18361	0.00975
35		1427 °C	997	0.06832	0.00030	3.30333	0.02392
36		1425 °C	996	0.00322	0.00009	0.14799	0.00136
37		1474 °C	997	0.00045	0.00005	0.00025	0.00005
OREGp-3							
1	X	463 °C	2997	0.00025	0.00004	0.00665	0.00008
2	X	463 °C	2997	0.00006	0.00004	0.00247	0.00005
3	X	516 °C	2996	0.00045	0.00004	0.01347	0.00011
4	X	516 °C	2997	0.00019	0.00004	0.00694	0.00007
5	X	569 °C	2997	0.00083	0.00005	0.03612	0.00034
6	X	569 °C	2996	0.00062	0.00005	0.02282	0.00035
7		622 °C	1996	0.00207	0.00006	0.09638	0.00110
8		622 °C	1997	0.00168	0.00005	0.07761	0.00066
9		675 °C	1996	0.00997	0.00012	0.47277	0.00596
10		675 °C	1996	0.00953	0.00012	0.45749	0.00505
11		727 °C	1997	0.03023	0.00019	1.56997	0.00681
12		727 °C	1995	0.01976	0.00017	1.00792	0.00860
13		779 °C	1996	0.03546	0.00021	1.85793	0.01141
14		779 °C	1997	0.02338	0.00021	1.21198	0.00877
15		830 °C	997	0.02334	0.00015	1.18531	0.01089
16		830 °C	997	0.01880	0.00015	0.92520	0.00637
17		881 °C	996	0.03209	0.00019	1.67982	0.01052
18		881 °C	997	0.02317	0.00017	1.18416	0.01394
19		696 °C	2997	0.00156	0.00004	0.07098	0.00104
20		696 °C	2995	0.00158	0.00006	0.07549	0.00074
21		748 °C	2996	0.00479	0.00009	0.23625	0.00294
22		748 °C	2997	0.00463	0.00008	0.21429	0.00209
23		799 °C	2997	0.01144	0.00012	0.55825	0.00604
24		799 °C	2996	0.01018	0.00010	0.48850	0.00556
25		851 °C	2997	0.02031	0.00017	1.02682	0.00648
26		851 °C	2996	0.01494	0.00013	0.76151	0.00599
27		932 °C	996	0.01342	0.00012	0.66765	0.00752
28		932 °C	996	0.00961	0.00013	0.47365	0.00698
29		983 °C	996	0.01139	0.00013	0.55421	0.00527
30		983 °C	996	0.00465	0.00008	0.21201	0.00177
31		1033 °C	996	0.00320	0.00007	0.15282	0.00145
32		1033 °C	996	0.00121	0.00005	0.05466	0.00063
33		1133 °C	996	0.00375	0.00007	0.18638	0.00205
34		1232 °C	997	0.00652	0.00009	0.31734	0.00424
35		1330 °C	994	0.00680	0.00010	0.32833	0.00427
36		1427 °C	997	0.27518	0.00086	13.79870	0.02945

#	E_a	Temp (°C)	Time (s)	$^{39}Ar \pm 1\sigma$ (nA)		$^{37}Ar \pm 1\sigma$ (nA)	
37		1426 °C	997	0.01591	0.00018	0.80766	0.00525
38		1475 °C	997	0.00039	0.00004	0.00418	0.00007
OREGp-4							
1	X	459 °C	596	0.00032	0.00004	0.00358	0.00009
2	X	458 °C	596	0.00006	0.00003	0.00126	0.00006
3	X	513 °C	595	0.00033	0.00004	0.00585	0.00014
4	X	511 °C	596	0.00008	0.00005	0.00286	0.00007
5	X	564 °C	596	0.00042	0.00004	0.01270	0.00017
6	X	564 °C	596	0.00021	0.00004	0.00758	0.00010
7		617 °C	596	0.00074	0.00004	0.02950	0.00028
8		616 °C	595	0.00044	0.00004	0.01869	0.00012
9		667 °C	596	0.00173	0.00004	0.07765	0.00052
10		669 °C	595	0.00114	0.00004	0.05685	0.00049
11		720 °C	597	0.00423	0.00005	0.21339	0.00191
12		719 °C	595	0.00286	0.00005	0.14673	0.00087
13		775 °C	596	0.00907	0.00006	0.48767	0.00222
14		771 °C	595	0.00806	0.00006	0.41911	0.00165
15		826 °C	595	0.01591	0.00009	0.82614	0.00355
16		824 °C	595	0.00811	0.00011	0.40828	0.00714
17		873 °C	595	0.01092	0.00007	0.53639	0.00569
18		878 °C	595	0.00567	0.00008	0.27235	0.00181
19		929 °C	595	0.00551	0.00010	0.29503	0.00170
20		925 °C	593	0.00250	0.00006	0.13542	0.00159
21		977 °C	596	0.00239	0.00009	0.12281	0.00080
22		980 °C	595	0.00101	0.00009	0.05279	0.00065
23		1028 °C	596	0.00124	0.00011	0.05696	0.00053
24		1028 °C	596	0.00070	0.00009	0.02736	0.00022
25		1079 °C	595	0.00181	0.00014	0.07960	0.00072
26		1081 °C	595	0.00135	0.00014	0.06420	0.00072
27		1130 °C	595	0.00191	0.00011	0.08271	0.00067
28		1128 °C	596	0.00097	0.00010	0.03918	0.00037
29		1325 °C	595	0.03978	0.00013	2.03135	0.01145
30		1323 °C	596	0.00997	0.00011	0.46959	0.00625
31		1314 °C	596	0.00633	0.00010	0.30131	0.00196
32		1321 °C	595	0.00543	0.00010	0.23848	0.00207
BV-8p-4							
1		420 °C	1200	0.00023	0.00004	0.00311	0.00009
2		420 °C	1200	0.00005	0.00003	0.00092	0.00006
3		466 °C	1200	0.00027	0.00004	0.00260	0.00008
4		466 °C	1200	0.00005	0.00003	0.00111	0.00006
5	X	555 °C	1200	0.00107	0.00004	0.01269	0.00023
6	X	555 °C	1200	0.00028	0.00003	0.00507	0.00016
7	X	599 °C	1200	0.00078	0.00004	0.01316	0.00029
8	X	599 °C	1200	0.00033	0.00003	0.00782	0.00022

#	E_a	Temp (°C)	Time (s)	^{39}Ar ± 1σ (nA)		^{37}Ar ± 1σ (nA)	
9	X	643 °C	1200	0.00092	0.00004	0.02351	0.00043
10	X	643 °C	1200	0.00050	0.00003	0.01542	0.00040
11	X	578 °C	4000	0.00016	0.00003	0.00506	0.00024
12	X	511 °C	5000	---	---	0.00097	0.00009
13	X	444 °C	6000	0.00001	0.00003	0.00009	0.00005
14	X	489 °C	6000	---	---	0.00048	0.00007
15	X	600 °C	6000	0.00049	0.00004	0.01359	0.00022
16	X	556 °C	4000	0.00010	0.00003	0.00234	0.00011
17	X	511 °C	5000	0.00002	0.00003	0.00069	0.00008
18	X	466 °C	6000	0.00000	0.00003	0.00064	0.00010
19	X	489 °C	10000	---	---	0.00042	0.00005
20	X	600 °C	8000	0.00048	0.00004	0.01431	0.00013
21		644 °C	6000	0.00112	0.00004	0.03921	0.00066
22		687 °C	1200	0.00063	0.00003	0.02447	0.00062
23		730 °C	1200	0.00193	0.00004	0.06898	0.00190
24		773 °C	1200	0.00435	0.00005	0.16892	0.00062
25		815 °C	1200	0.00829	0.00007	0.31669	0.00176
26		857 °C	1200	0.01213	0.00007	0.44585	0.00230
27		773 °C	4000	0.00365	0.00005	0.13808	0.00102
28		688 °C	6000	0.00055	0.00003	0.01792	0.00020
29		600 °C	10000	0.00011	0.00003	0.00294	0.00008
30		731 °C	6000	0.00162	0.00004	0.05970	0.00053
31		816 °C	6000	0.02069	0.00011	0.82144	0.00387
32		878 °C	1200	0.01920	0.00010	0.72338	0.00447
33		917 °C	1200	0.02396	0.00023	0.93939	0.00438
34		931 °C	1200	0.01348	0.00006	0.54704	0.00358
35		951 °C	1200	0.01126	0.00009	0.48403	0.00161
36		956 °C	1200	0.00784	0.00006	0.34486	0.00135
37		986 °C	1200	0.01069	0.00008	0.46666	0.00345
38		858 °C	6000	0.00319	0.00005	0.13685	0.00166
39		688 °C	10000	0.00015	0.00003	0.00538	0.00012
40		774 °C	8000	0.00056	0.00004	0.02287	0.00028
41		940 °C	6000	0.00926	0.00007	0.42409	0.00280
42		600 °C	15000	0.00008	0.00003	0.00111	0.00007
43		731 °C	10000	0.00013	0.00003	0.00624	0.00012
44		CO_2		---	---	0.00031	0.00009
45		CO_2		---	---	0.00013	0.00009
46		CO_2		---	---	---	---
47		CO_2		0.00091	0.00003	0.03748	0.00029
48		CO_2		---	---	0.00357	0.00012
49		CO_2		0.02654	0.00021	1.09889	0.00325
50		CO_2		0.01999	0.00006	0.83527	0.00247
51		CO_2		0.00193	0.00005	0.08887	0.00085
52		CO_2		0.00288	0.00006	0.12120	0.00114
53		CO_2		0.01595	0.00006	0.73447	0.00340
54		CO_2		0.00180	0.00004	0.08302	0.00057
55		CO_2		0.00348	0.00004	0.15335	0.00121
56		CO_2		0.02524	0.00012	1.13651	0.00475

#	E_a	Temp (°C)	Time (s)	^{39}Ar ± 1σ (nA)		^{37}Ar ± 1σ (nA)	
57		CO_2		0.02693	0.00016	1.26724	0.00546
58		CO_2		0.02533	0.00025	1.17185	0.00390
59		CO_2		0.00546	0.00004	0.23171	0.00135
60		CO_2		0.00839	0.00010	0.40309	0.00171
61		CO_2		0.00358	0.00004	0.17128	0.00157
62		CO_2		0.00020	0.00003	0.01042	0.00025
BV-8p-2							
1		467 °C	900	0.00006	0.00005	0.00063	0.00012
2		518 °C	900	0.00006	0.00005	0.00065	0.00012
3		517 °C	900	0.00042	0.00005	0.00458	0.00018
4		517 °C	1200	0.00029	0.00005	0.00340	0.00017
5	X	570 °C	900	0.00084	0.00005	0.00671	0.00018
6	X	570 °C	1200	0.00056	0.00005	0.00381	0.00017
7	X	623 °C	900	0.00166	0.00005	0.01186	0.00024
8	X	622 °C	1200	0.00119	0.00005	0.00766	0.00023
9	X	675 °C	900	0.00318	0.00006	0.02398	0.00029
10	X	675 °C	1200	0.00274	0.00006	0.01953	0.00040
11		727 °C	900	0.00727	0.00007	0.05721	0.00031
12		726 °C	1200	0.00684	0.00007	0.05584	0.00039
13		779 °C	900	0.01806	0.00010	0.14803	0.00067
14		779 °C	1200	0.00000	0.00009	0.00000	0.00067
15		829 °C	900	0.03049	0.00012	0.26292	0.00087
16		830 °C	1200	0.02736	0.00014	0.24389	0.00094
17		753 °C	1500	0.00378	0.00006	0.03353	0.00035
18		675 °C	1700	0.00057	0.00005	0.00450	0.00018
19		649 °C	1904	0.00032	0.00004	0.00206	0.00013
20		570 °C	2105	0.00007	0.00004	0.00026	0.00012
21		490 °C	2300	0.00002	0.00004	0.00027	0.00012
22		596 °C	2300	0.00010	0.00004	0.00082	0.00013
23		701 °C	2300	0.00120	0.00004	0.01070	0.00018
24		804 °C	2300	0.01482	0.00010	0.13179	0.00088
25		856 °C	1200	0.02122	0.00011	0.19150	0.00081
26		906 °C	1200	0.04957	0.00016	0.44835	0.00128
27		957 °C	1200	0.07754	0.00018	0.71002	0.00169
28		1008 °C	1200	0.09496	0.00029	0.86082	0.00175
29		1031 °C	1200	0.06736	0.00016	0.61198	0.00095
30		1031 °C	1200	0.04044	0.00017	0.36920	0.00095
31		1031 °C	1200	0.02881	0.00013	0.26475	0.00088
32		1032 °C	1200	0.02321	0.00016	0.21437	0.00095
33		931 °C	1500	0.00502	0.00006	0.04282	0.00040
34		830 °C	2000	0.00097	0.00005	0.00864	0.00016
35		727 °C	2500	0.00015	0.00004	0.00165	0.00013
36		623 °C	3000	0.00003	0.00004	0.00047	0.00011
37		830 °C	2500	0.00092	0.00005	0.00858	0.00019
38		932 °C	2000	0.00371	0.00006	0.03266	0.00037
39		1033 °C	1500	0.01738	0.00013	0.16192	0.00096

#	E_a	Temp (°C)	Time (s)	^{39}Ar ± 1σ (nA)		^{37}Ar ± 1σ (nA)	
40		1057 °C	1200	0.02455	0.00013	0.22042	0.00109
41		1058 °C	1200	0.01987	0.00015	0.18074	0.00076
42		1083 °C	1200	0.02863	0.00013	0.25413	0.00116
43		1082 °C	1200	0.02015	0.00012	0.17919	0.00089
44		1108 °C	1200	0.02559	0.00014	0.22647	0.00103
45		1108 °C	1200	0.01943	0.00012	0.17953	0.00130
46		1132 °C	1200	0.02512	0.00010	0.22538	0.00103
47		1133 °C	1200	0.01879	0.00017	0.16308	0.00089
48		1157 °C	1200	0.02334	0.00011	0.20683	0.00076
49		1157 °C	1200	0.01834	0.00014	0.16212	0.00076
50		1182 °C	1200	0.02134	0.00014	0.18973	0.00103
51		1182 °C	1200	0.01588	0.00010	0.14081	0.00076
52		1207 °C	1200	0.02548	0.00010	0.22304	0.00090
53		1207 °C	1200	0.01805	0.00022	0.15126	0.00076
54		1230 °C	1200	0.02309	0.00012	0.20840	0.00083
55		1231 °C	1200	0.01796	0.00010	0.16083	0.00152
56		1281 °C	1200	0.03963	0.00018	0.36112	0.00234
57		1305 °C	1200	0.03459	0.00016	0.31691	0.00111
58		1330 °C	1200	0.03233	0.00011	0.29480	0.00090
59		1378 °C	1200	0.08929	0.00022	0.86033	0.00463
60		1427 °C	1200	0.34021	0.00066	3.37813	0.01313
61		1473 °C	1200	0.01916	0.00009	0.18777	0.00159
62		1520 °C	1200	0.00570	0.00008	0.05268	0.00053
63		1567 °C	1200	0.00039	0.00005	0.00074	0.00014
64		1545 °C	1200	0.00193	0.00006	0.00107	0.00013
BV-8p-3							
1	X	463 °C	600	0.00435	0.00006	0.00797	0.00012
2	X	464 °C	600	0.00135	0.00004	0.00207	0.00009
3	X	543 °C	600	0.00826	0.00008	0.01598	0.00018
4	X	544 °C	600	0.00274	0.00004	0.00560	0.00012
5	X	623 °C	600	0.01696	0.00009	0.04124	0.00028
6	X	624 °C	600	0.00478	0.00005	0.01474	0.00014
7	X	676 °C	600	0.01438	0.00009	0.06432	0.00053
8	X	676 °C	600	0.00576	0.00007	0.03379	0.00027
9		728 °C	600	0.01711	0.00011	0.13517	0.00162
10		728 °C	600	0.00904	0.00009	0.08199	0.00057
11		780 °C	600	0.03331	0.00014	0.33865	0.00143
12		778 °C	600	0.02013	0.00011	0.22827	0.00112
13		675 °C	2200	0.00326	0.00005	0.03272	0.00024
14		623 °C	2400	0.00000	0.00003	0.00000	0.00013
15		701 °C	2600	0.00602	0.00008	0.06671	0.00053
16		753 °C	2800	0.02417	0.00013	0.29593	0.00150
17		831 °C	600	0.04155	0.00018	0.47967	0.00301
18		827 °C	599	0.02966	0.00015	0.35067	0.00176
19		882 °C	600	0.09615	0.00028	0.99043	0.00395
20		882 °C	600	0.04712	0.00017	0.51448	0.00352

#	E_a	Temp (°C)	Time (s)	^{39}Ar ± 1σ (nA)		^{37}Ar ± 1σ (nA)	
21		933 °C	600	0.08995	0.00021	1.07097	0.00453
22		933 °C	600	0.05424	0.00018	0.66487	0.00321
23		831 °C	2200	0.02061	0.00014	0.21538	0.00176
24		753 °C	2400	0.00392	0.00006	0.03392	0.00020
25		856 °C	2600	0.02709	0.00010	0.29627	0.00145
26		933 °C	2800	0.11230	0.00024	1.56604	0.00594
27		982 °C	600	0.05557	0.00015	0.84116	0.00215
28		984 °C	600	0.04421	0.00017	0.67039	0.00317
29		1009 °C	600	0.05516	0.00017	0.83892	0.00342
30		1007 °C	600	0.03804	0.00041	0.58664	0.00305
31		1033 °C	600	0.05164	0.00021	0.82635	0.00279
32		1033 °C	600	0.03412	0.00014	0.55841	0.00165
33		CO_2		---	---	0.00016	0.00007
34		CO_2		---	---	0.00010	0.00009
35		CO_2		0.00049	0.00004	0.00710	0.00014
36		CO_2		0.07263	0.00026	1.14765	0.00424
37		CO_2		0.28034	0.00069	4.37200	0.02018
38		CO_2		0.20995	0.00037	3.39563	0.02925
39		CO_2		0.17484	0.00033	2.54337	0.02300
40		CO_2		0.04789	0.00016	0.92176	0.00418
41		CO_2		0.01344	0.00012	0.26788	0.00140
42		CO_2		0.10159	0.00022	1.89909	0.01257
43		CO_2		0.00017	0.00003	0.00295	0.00011
44		CO_2		0.00315	0.00005	0.05843	0.00042

DCp-1

1		464 °C	597	0.00002	0.00004	0.00013	0.00006
2		464 °C	596	0.00008	0.00004	0.00015	0.00004
3	X	517 °C	596	0.00035	0.00004	0.00037	0.00008
4	X	517 °C	597	0.00015	0.00004	0.00027	0.00004
5	X	570 °C	596	0.00060	0.00005	0.00056	0.00009
6	X	570 °C	596	0.00040	0.00004	0.00042	0.00005
7	X	624 °C	594	0.00114	0.00006	0.00115	0.00009
8	X	624 °C	597	0.00070	0.00005	0.00040	0.00007
9		676 °C	596	0.00282	0.00007	0.00163	0.00011
10		675 °C	596	0.00153	0.00006	0.00154	0.00009
11		728 °C	596	0.00626	0.00008	0.00384	0.00014
12		728 °C	597	0.00498	0.00008	0.00260	0.00011
13		675 °C	2200	0.00390	0.00009	0.00251	0.00005
14		623 °C	2400	0.00074	0.00005	0.00057	0.00003
15		701 °C	2600	0.00858	0.00012	0.00675	0.00008
16		753 °C	2800	0.03168	0.00017	0.02317	0.00013
17		830 °C	600	0.02906	0.00013	0.01355	0.00018
18		831 °C	600	0.01967	0.00018	0.01646	0.00015
19		883 °C	600	0.03004	0.00017	0.02227	0.00028
20		883 °C	600	0.02012	0.00015	0.01744	0.00017
21		933 °C	600	0.03177	0.00019	0.02520	0.00021

#	E_a	Temp (°C)	Time (s)	^{39}Ar ± 1σ (nA)		^{37}Ar ± 1σ (nA)	
22		933 °C	600	0.02219	0.00012	0.01842	0.00018
23		984 °C	600	0.03124	0.00020	0.02231	0.00014
24		982 °C	600	0.02179	0.00014	0.01650	0.00006
25		CO_2		0.00004	0.00005	0.00024	0.00010
26		CO_2		0.00009	0.00004	0.00029	0.00024
27		CO_2		0.00006	0.00006	0.00045	0.00015
28		CO_2		0.00063	0.00007	0.00051	0.00017
29		CO_2		0.00140	0.00007	0.00130	0.00017
DCp-2							
1		464 °C	596	0.00016	0.00003	0.00388	0.00018
2		464 °C	597	0.00016	0.00002	0.00367	0.00015
3	X	518 °C	597	0.00037	0.00003	0.01981	0.00032
4	X	518 °C	597	0.00024	0.00002	0.00903	0.00025
5	X	571 °C	596	0.00051	0.00002	0.03526	0.00037
6	X	570 °C	597	0.00026	0.00001	0.01901	0.00035
7	X	623 °C	596	0.00086	0.00002	0.07097	0.00053
8	X	624 °C	597	0.00047	0.00002	0.04091	0.00039
9		676 °C	596	0.00198	0.00005	0.17600	0.00133
10		676 °C	597	0.00101	0.00003	0.10001	0.00071
11		728 °C	596	0.00387	0.00004	0.37741	0.00121
12		728 °C	597	0.00290	0.00003	0.28509	0.00266
13		780 °C	596	0.01176	0.00011	1.23901	0.00763
14		780 °C	596	0.00839	0.00006	0.89203	0.00388
15		831 °C	596	0.02035	0.00017	2.16412	0.00994
16		831 °C	597	0.01265	0.00006	1.38168	0.01212
17		983 °C	596	0.04661	0.00020	5.06964	0.03397
18		984 °C	596	0.02105	0.00018	2.19224	0.00874
19		1034 °C	596	0.02230	0.00018	2.36530	0.00959
20		1034 °C	596	0.01291	0.00015	1.40425	0.00838
21		CO_2		0.00007	0.00002	0.00037	0.00024
22		CO_2		0.00009	0.00002	0.00770	0.00030
23		CO_2		0.00019	0.00003	0.01427	0.00039
24		CO_2		0.00054	0.00005	0.05834	0.00060
25		CO_2		0.00169	0.00007	0.16069	0.00144
26		CO_2		0.00125	0.00004	0.12174	0.00084
27		CO_2		0.00331	0.00008	0.32467	0.00312
28		CO_2		0.00652	0.00009	0.70526	0.00445
29		CO_2		0.06432	0.00028	6.76300	0.05192
30		CO_2		0.01650	0.00010	1.77854	0.01039
31		CO_2		0.06851	0.00028	7.37123	0.04601
32		CO_2		0.00936	0.00006	1.02298	0.00520
33		CO_2		0.09216	0.00014	9.84147	0.04011
34		CO_2		0.04739	0.00024	4.96664	0.03270
35		CO_2		0.03674	0.00021	4.02542	0.02676
36		CO_2		0.00049	0.00004	0.04432	0.00083

#	E_a	Temp (°C)	Time (s)	^{39}Ar ± 1σ (nA)		^{37}Ar ± 1σ (nA)	
DCp-3							
1	X	464 °C	596	0.00004	0.00005	0.00324	0.00011
2	X	464 °C	596	0.00001	0.00005	0.00157	0.00010
3	X	518 °C	597	0.00016	0.00006	0.00660	0.00015
4	X	517 °C	596	0.00004	0.00005	0.00354	0.00012
5	X	571 °C	595	0.00021	0.00006	0.01471	0.00018
6	X	571 °C	596	0.00004	0.00006	0.00852	0.00017
7	X	624 °C	596	0.00031	0.00008	0.03225	0.00034
8	X	624 °C	596	0.00021	0.00007	0.02096	0.00036
9		675 °C	597	0.00088	0.00008	0.08316	0.00075
10		676 °C	596	0.00065	0.00007	0.06225	0.00042
11		728 °C	596	0.00195	0.00007	0.18532	0.00117
12		728 °C	597	0.00141	0.00007	0.12643	0.00086
13		780 °C	596	0.00301	0.00010	0.29597	0.00176
14		780 °C	596	0.00200	0.00008	0.19068	0.00120
15		831 °C	596	0.00418	0.00008	0.39972	0.00237
16		831 °C	591	0.00241	0.00008	0.25241	0.00172
17		882 °C	596	0.00458	0.00010	0.45190	0.00234
18		883 °C	596	0.00318	0.00008	0.30187	0.00142
19		933 °C	596	0.00539	0.00010	0.52590	0.00439
20		933 °C	596	0.00386	0.00008	0.37978	0.00171
21		983 °C	596	0.00658	0.00009	0.64603	0.00358
22		984 °C	596	0.00471	0.00009	0.45258	0.00263
23		1034 °C	596	0.00714	0.00009	0.69773	0.00483
24		1034 °C	596	0.00481	0.00010	0.46962	0.00286
25		1084 °C	596	0.00632	0.00010	0.59052	0.00371
26		1084 °C	596	0.00310	0.00009	0.30547	0.00217
27		1134 °C	596	0.00457	0.00009	0.42619	0.00472
28		1134 °C	596	0.00277	0.00008	0.24763	0.00193
29		1184 °C	596	0.00461	0.00008	0.40420	0.00309
30		1183 °C	596	0.00260	0.00008	0.22629	0.00196
31		1233 °C	596	0.00262	0.00009	0.23123	0.00218
32		1233 °C	596	0.00160	0.00008	0.12781	0.00104
33		1282 °C	596	0.00193	0.00007	0.16572	0.00124
34		1281 °C	596	0.00107	0.00007	0.08592	0.00106
35		1331 °C	596	0.00158	0.00008	0.11704	0.00117
36		1331 °C	595	0.00078	0.00007	0.05832	0.00052
37		1380 °C	595	0.00134	0.00008	0.11190	0.00105
38		1380 °C	596	0.00069	0.00007	0.05755	0.00052
39		1429 °C	596	0.00215	0.00007	0.18028	0.00142
40		1429 °C	596	0.00987	0.00011	0.95541	0.00385
41		1525 °C	595	0.01350	0.00012	1.25938	0.01013
42		1505 °C	595	0.00231	0.00008	0.11859	0.00125
JAPp-1							
1	X	459 °C	595			0.01505	0.00018

#	E_a	Temp (°C)	Time (s)	$^{39}Ar \pm 1\sigma$ (nA)	$^{37}Ar \pm 1\sigma$ (nA)
2	X	459 °C	595	0.00636	0.00009
3	X	511 °C	596	0.03753	0.00023
4	X	512 °C	596	0.02801	0.00047
5	X	565 °C	596	0.13370	0.00158
6	X	565 °C	596	0.09091	0.00123
7	X	616 °C	596	0.32776	0.00561
8	X	617 °C	596	0.14931	0.00133
9	X	669 °C	596	0.45735	0.00936
10	X	670 °C	595	0.28787	0.00191
11	X	722 °C	596	1.33875	0.01063
12	X	720 °C	596	1.24137	0.00491
13	X	772 °C	595	2.44173	0.01338
14	X	772 °C	596	1.31846	0.03218
15	X	822 °C	596	1.95948	0.01089
16	X	823 °C	596	1.01798	0.00651
17		873 °C	596	0.95460	0.00953
18		873 °C	596	0.20973	0.00141
19		923 °C	596	0.16946	0.00157
20		925 °C	596	0.06046	0.00091
21		977 °C	595	0.07898	0.00101
22		980 °C	595	0.04301	0.00038
24		1027 °C	596	0.06458	0.00053
25		1029 °C	595	0.03839	0.00053
26		1077 °C	595	0.05630	0.00045
27		1078 °C	595	0.03391	0.00034
28		1127 °C	596	0.04935	0.00051
29		1129 °C	595	0.03034	0.00043
22		1179 °C	596	0.04359	0.00052
24		1323 °C	595	0.21009	0.00108
25		1324 °C	595	0.09941	0.00071
26		1321 °C	595	0.06863	0.00075

JAPp-2

1	X	458 °C	595	0.00509	0.00009
2	X	459 °C	595	0.00211	0.00006
3	X	512 °C	595	0.01257	0.00019
4	X	512 °C	596	0.00882	0.00008
5	X	563 °C	596	0.04729	0.00072
6	X	565 °C	595	0.03757	0.00056
7	X	618 °C	596	0.13974	0.00168
8	X	618 °C	596	0.06019	0.00099
9	X	670 °C	595	0.17007	0.00085
10	X	668 °C	596	0.14275	0.00160
11	X	720 °C	595	0.58423	0.00104
12	X	721 °C	595	0.52918	0.00434
13	X	775 °C	595	0.85226	0.00698
14	X	773 °C	595	0.43141	0.00290

#	E_a	Temp (°C)	Time (s)	$^{39}Ar \pm 1\sigma$ (nA)		$^{37}Ar \pm 1\sigma$ (nA)	
15	X	824 °C	596			0.52673	0.00324
16	X	877 °C	596			0.13869	0.00087
17		873 °C	596			0.03752	0.00025
18		929 °C	595			0.05009	0.00045
19		927 °C	595			0.02154	0.00015
20		975 °C	596			0.03569	0.00064
21		975 °C	596			0.02165	0.00019
22		1031 °C	595			0.03837	0.00050
23		1029 °C	595			0.02479	0.00022
24		1076 °C	596			0.04340	0.00054
25		1078 °C	595			0.02648	0.00023
26		1127 °C	595			0.03795	0.00048
27		1124 °C	595			0.02361	0.00025
28		1324 °C	595			0.12157	0.00157
29		1325 °C	596			0.03716	0.00049
30		1322 °C	595			0.02066	0.00024

TROCp-1

1	X	460 °C	597	0.00012	0.00004	0.02781	0.00058
2	X	459 °C	596	0.00006	0.00003	0.01443	0.00056
3	X	513 °C	596	0.00039	0.00004	0.06079	0.00077
4	X	513 °C	596	0.00021	0.00004	0.02932	0.00062
5	X	566 °C	596	0.00083	0.00004	0.12393	0.00104
6	X	566 °C	596	0.00035	0.00004	0.06168	0.00083
7	X	619 °C	597	0.00143	0.00005	0.24727	0.00141
8	X	619 °C	597	0.00086	0.00005	0.13868	0.00088
9		672 °C	597	0.00301	0.00006	0.51263	0.00325
10		673 °C	597	0.00175	0.00005	0.31808	0.00168
11		724 °C	596	0.00612	0.00008	1.11394	0.00718
12		724 °C	596	0.00416	0.00007	0.75222	0.00492
13		777 °C	597	0.01256	0.00013	2.28644	0.01176
14		775 °C	597	0.00791	0.00009	1.47656	0.01064
15		829 °C	597	0.02006	0.00016	3.67104	0.01446
16		827 °C	597	0.01257	0.00011	2.26263	0.01637
17		879 °C	596	0.02680	0.00019	4.65417	0.04192
18		879 °C	596	0.01562	0.00014	2.76918	0.01222
19		931 °C	597	0.02510	0.00021	4.49722	0.02527
20		930 °C	597	0.01274	0.00013	2.23455	0.01380
21		982 °C	596	0.01804	0.00015	3.26895	0.02303
22		982 °C	597	0.00967	0.00012	1.73756	0.00769
23		1033 °C	597	0.01170	0.00014	2.05610	0.01194
24		1032 °C	597	0.00659	0.00010	1.17802	0.00694
25		1082 °C	596	0.00909	0.00010	1.65791	0.01447
26		1083 °C	597	0.00480	0.00010	0.87612	0.00549
27		1132 °C	597	0.00538	0.00008	0.95156	0.00628
28		1132 °C	597	0.00237	0.00006	0.43484	0.00312
29		1231 °C	597	0.00526	0.00007	0.97961	0.00551

#	E_a	Temp (°C)	Time (s)	^{39}Ar ± 1σ (nA)		^{37}Ar ± 1σ (nA)	
30		1231 °C	596	0.00120	0.00006	0.20328	0.00141
31		1329 °C	597	0.00390	0.00008	0.70182	0.00434
32		1330 °C	597	0.00181	0.00005	0.29370	0.00162
33		???	594	0.00155	0.00005	0.27767	0.00204
34		???	594	0.16646	0.00055	29.88402	0.12937
35		???	594	0.01976	0.00016	3.57034	0.01299
36		???	596	0.01446	0.00012	2.52098	0.01561
37		???	596	0.09071	0.00039	15.45525	0.14067
VZ699-1							
1	X	464 °C	596	0.00534	0.00008	0.02226	0.00020
2	X	464 °C	597	0.00172	0.00007	0.00774	0.00015
3	X	517 °C	597	0.00749	0.00010	0.03756	0.00026
4	X	517 °C	596	0.00338	0.00007	0.01947	0.00020
5	X	570 °C	596	0.01451	0.00013	0.10390	0.00069
6	X	570 °C	596	0.00736	0.00008	0.05733	0.00031
7	X	623 °C	596	0.02368	0.00017	0.19232	0.00127
8	X	623 °C	596	0.01278	0.00012	0.07757	0.00081
9	X	675 °C	596	0.03563	0.00024	0.18403	0.00200
10	X	675 °C	596	0.01877	0.00017	0.09018	0.00092
11	X	728 °C	596	0.04458	0.00024	0.26260	0.00212
12	X	728 °C	596	0.02351	0.00014	0.13492	0.00094
13	X	779 °C	596	0.04888	0.00023	0.31707	0.00167
14	X	780 °C	596	0.02663	0.00018	0.16117	0.00152
15	X	831 °C	596	0.04844	0.00028	0.33845	0.00303
16	X	831 °C	596	0.02665	0.00019	0.17956	0.00130
17		882 °C	596	0.04453	0.00025	0.35476	0.00225
18		883 °C	597	0.02429	0.00016	0.17343	0.00167
19		933 °C	597	0.03755	0.00021	0.25841	0.00264
20		933 °C	596	0.01969	0.00021	0.09412	0.00092
21		984 °C	597	0.03155	0.00018	0.10566	0.00102
22		984 °C	597	0.01712	0.00019	0.04218	0.00045
23		1034 °C	597	0.03057	0.00020	0.06977	0.00062
24		1034 °C	595	0.01753	0.00021	0.03797	0.00044
25		1084 °C	597	0.03917	0.00028	0.10595	0.00106
26		1084 °C	596	0.02097	0.00019	0.06589	0.00055
27		1134 °C	596	0.05699	0.00023	0.24204	0.00227
28		1134 °C	596	0.02548	0.00017	0.10896	0.00127
29		1184 °C	596	0.03453	0.00018	0.12632	0.00083
30		1183 °C	596	0.00761	0.00010	0.04492	0.00048
31		1233 °C	596	0.00569	0.00008	0.07928	0.00060
32		1233 °C	595	0.00155	0.00007	0.02494	0.00041
33		1282 °C	597	0.00156	0.00008	0.04869	0.00046
34		1282 °C	586	0.00087	0.00007	0.01883	0.00042
35		1331 °C	532	0.00121	0.00007	0.07330	0.00053
36		1331 °C	595	0.00044	0.00007	0.01681	0.00039
37		1380 °C	596	0.00101	0.00007	0.03507	0.00045

#	E_a	Temp (°C)	Time (s)	^{39}Ar ± 1σ (nA)		^{37}Ar ± 1σ (nA)	
38		1379 °C	596	0.00079	0.00007	0.04772	0.00049
39		1428 °C	596	0.00160	0.00008	0.09456	0.00090
40		1429 °C	594	0.00267	0.00008	0.13659	0.00143
41		1518 °C	596	0.00077	0.00007	0.00751	0.00039
42		1440 °C	596	0.00069	0.00008	0.00071	0.00038

SW-1-1

1	X	416 °C	594	0.00042	0.00008	0.00099	0.00010
2	X	464 °C	597	0.00174	0.00007	0.00717	0.00015
3	X	517 °C	596	0.00613	0.00010	0.03810	0.00033
4	X	517 °C	596	0.00196	0.00007	0.01835	0.00021
5	X	570 °C	596	0.00820	0.00013	0.13851	0.00070
6	X	570 °C	597	0.00246	0.00008	0.06754	0.00041
7	X	623 °C	596	0.00974	0.00014	0.35019	0.00204
8	X	623 °C	597	0.00289	0.00011	0.15676	0.00090
9	X	676 °C	597	0.01137	0.00013	0.73094	0.00397
10	X	676 °C	596	0.00487	0.00011	0.35745	0.00201
11	X	728 °C	596	0.01062	0.00013	0.88509	0.00420
12	X	728 °C	596	0.00470	0.00009	0.43351	0.00294
13	X	780 °C	596	0.01076	0.00011	0.95403	0.00550
14	X	780 °C	596	0.00489	0.00010	0.43219	0.00291
15	X	830 °C	596	0.01106	0.00011	0.73194	0.00503
16	X	832 °C	596	0.00560	0.00009	0.31142	0.00213
17		883 °C	596	0.02082	0.00014	0.53280	0.00157
18		882 °C	596	0.00940	0.00010	0.23329	0.00116
19		933 °C	596	0.01501	0.00011	0.37356	0.00229
20		933 °C	597	0.00743	0.00010	0.19458	0.00135
21		984 °C	596	0.01251	0.00011	0.39947	0.00206
22		984 °C	596	0.00624	0.00009	0.19092	0.00208
23		1034 °C	596	0.01138	0.00011	0.44581	0.00201
24		1034 °C	596	0.00501	0.00011	0.20479	0.00122
25		1084 °C	595	0.00800	0.00009	0.42442	0.00287
26		1084 °C	596	0.00293	0.00008	0.14369	0.00085
27		1134 °C	596	0.00492	0.00010	0.31422	0.00190
28		1134 °C	596	0.00155	0.00008	0.08909	0.00084
29		1183 °C	596	0.00437	0.00009	0.27092	0.00222
30		1184 °C	596	0.00165	0.00008	0.10070	0.00101
31		1233 °C	596	0.00443	0.00010	0.25972	0.00178
32		1233 °C	596	0.00182	0.00008	0.10651	0.00122
33		1282 °C	596	0.00560	0.00011	0.32609	0.00201
34		1283 °C	596	0.00230	0.00008	0.16314	0.00115
35		1332 °C	596	0.01122	0.00011	0.60432	0.00446
36		1331 °C	596	0.00104	0.00007	0.07836	0.00052
37		1380 °C	595	0.01679	0.00020	1.28522	0.00557
38		1381 °C	596	0.00401	0.00010	0.33366	0.00241
39		1429 °C	596	0.06296	0.00028	6.58542	0.02203
40		1429 °C	595	0.00130	0.00008	0.12667	0.00122

#	E_a	Temp (°C)	Time (s)	^{39}Ar ± 1σ (nA)		^{37}Ar ± 1σ (nA)	
41		1524 °C	595	0.00945	0.00012	1.00626	0.00408
42		1524 °C	596	0.00026	0.00007	0.00160	0.00038
GV-09-1							
1	X	464 °C	597	0.01405	0.00018	0.06764	0.00065
2	X	464 °C	596	0.00454	0.00009	0.01953	0.00034
3	X	517 °C	593	0.01346	0.00015	0.12095	0.00067
4	X	517 °C	596	0.00640	0.00012	0.06310	0.00068
5	X	570 °C	596	0.02081	0.00019	0.41526	0.00383
6	X	570 °C	596	0.00696	0.00013	0.21877	0.00258
7	X	624 °C	596	0.02159	0.00015	0.92959	0.00574
8	X	624 °C	596	0.00808	0.00015	0.49055	0.00224
9	X	676 °C	596	0.02523	0.00020	1.79293	0.00977
10	X	676 °C	596	0.01145	0.00010	0.92183	0.00360
11	X	728 °C	596	0.02874	0.00022	2.45573	0.01242
12	X	728 °C	596	0.00872	0.00017	1.22345	0.00673
13	X	780 °C	597	0.02946	0.00021	2.51839	0.01377
14	X	780 °C	595	0.03872	0.00021	1.20781	0.00644
15	X	831 °C	597	0.02830	0.00019	1.76212	0.00886
16	X	831 °C	596	0.02014	0.00015	0.76628	0.00279
17		882 °C	596	0.04314	0.00031	1.22305	0.00640
18		883 °C	596	0.01848	0.00014	0.55722	0.00404
19		933 °C	596	0.02935	0.00019	0.85010	0.00427
20		933 °C	596	0.01606	0.00016	0.47176	0.00389
21		984 °C	596	0.02873	0.00019	0.95153	0.00352
22		984 °C	596	0.01601	0.00014	0.51405	0.00312
23		1034 °C	596	0.02915	0.00020	1.03026	0.00608
24		1034 °C	596	0.01229	0.00016	0.48178	0.00381
25		1084 °C	596	0.01787	0.00017	0.95062	0.00809
26		1084 °C	597	0.00683	0.00011	0.33470	0.00258
27		1134 °C	596	0.01288	0.00013	0.71350	0.00517
28		1134 °C	596	0.00476	0.00014	0.25267	0.00260
29		1184 °C	596	0.01615	0.00018	1.06052	0.00717
30		1184 °C	596	0.00632	0.00018	0.39110	0.00327
31		1233 °C	596	0.01500	0.00017	0.86961	0.00548
32		1233 °C	597	0.00596	0.00010	0.44571	0.00264
33		1283 °C	597	0.02104	0.00017	1.13622	0.00618
34		1282 °C	594	0.00440	0.00015	0.33792	0.00269
35		1332 °C	597	0.02583	0.00027	1.73857	0.00690
36		1332 °C	597	0.00467	0.00011	0.34052	0.00246
37		1381 °C	300	0.07782	0.00030	7.04240	0.01322
38		1382 °C	300	0.01155	0.00014	1.14071	0.00811
39		1431 °C	200	0.09927	0.00044	10.59124	0.07458
BG-1p-1							
1		399 °C	900	0.00009	0.00005	0.00157	0.00034

#	E_a	Temp (°C)	Time (s)	^{39}Ar ± 1σ (nA)	^{37}Ar ± 1σ (nA)
2		422 °C	900	0.00045 0.00005	0.00319 0.00038
3		446 °C	900	0.00094 0.00005	0.00675 0.00042
4		468 °C	900	0.00151 0.00006	0.01056 0.00043
5		491 °C	900	0.00272 0.00006	0.01654 0.00049
6		514 °C	900	0.00520 0.00008	0.03665 0.00059
7		558 °C	900	0.01446 0.00011	0.14226 0.00098
8		580 °C	900	0.00932 0.00008	0.11903 0.00076
9		601 °C	900	0.01119 0.00009	0.14516 0.00106
10		622 °C	900	0.01304 0.00010	0.16202 0.00128
11		643 °C	900	0.01640 0.00011	0.19018 0.00121
12		644 °C	1200	0.01455 0.00010	0.17184 0.00120
13		601 °C	1200	0.00279 0.00006	0.03112 0.00071
14		558 °C	1200	0.00051 0.00005	0.00593 0.00054
15		514 °C	1200	0.00010 0.00004	0.00119 0.00050
16		592 °C	1200	0.00163 0.00005	0.01801 0.00042
17		644 °C	1200	0.00911 0.00009	0.10689 0.00092
18		665 °C	900	0.01249 0.00008	0.14852 0.00127
19		685 °C	900	0.01982 0.00011	0.24958 0.00137
20		705 °C	900	0.03088 0.00011	0.40622 0.00178
21		725 °C	900	0.03820 0.00013	0.50559 0.00209
22		745 °C	900	0.04626 0.00015	0.62089 0.00199
23		765 °C	900	0.05251 0.00018	0.72702 0.00214
24		784 °C	900	0.06146 0.00021	0.83202 0.00273
25		802 °C	900	0.05765 0.00018	0.76350 0.00249
26		803 °C	900	0.03612 0.00012	0.47613 0.00157
27		765 °C	900	0.00993 0.00008	0.12458 0.00099
28		725 °C	900	0.00275 0.00005	0.03860 0.00068
29		685 °C	900	0.00078 0.00005	0.01090 0.00054
30		644 °C	900	0.00018 0.00004	0.00376 0.00039
31		705 °C	900	0.00136 0.00005	0.01752 0.00046
32		746 °C	900	0.00418 0.00006	0.05283 0.00065
33		785 °C	900	0.01185 0.00009	0.15259 0.00110
34		803 °C	900	0.01713 0.00010	0.22008 0.00144
35		822 °C	900	0.02297 0.00012	0.30762 0.00161
36		839 °C	900	0.02989 0.00014	0.39002 0.00159
37		857 °C	900	0.03624 0.00013	0.46887 0.00176
38		876 °C	900	0.04036 0.00014	0.50905 0.00175
39		894 °C	900	0.03919 0.00015	0.49095 0.00180
40		911 °C	900	0.04603 0.00015	0.55467 0.00200
41		911 °C	900	0.02370 0.00010	0.27698 0.00142
42		875 °C	900	0.00697 0.00006	0.07762 0.00080
43		839 °C	900	0.00269 0.00005	0.03155 0.00066
44		802 °C	900	0.00104 0.00005	0.01238 0.00047
45		765 °C	900	0.00041 0.00004	0.00499 0.00043
46		725 °C	900	0.00025 0.00004	0.00139 0.00043
47		783 °C	900	0.00054 0.00004	0.00608 0.00046
48		821 °C	900	0.00131 0.00005	0.01458 0.00052
49		858 °C	900	0.00281 0.00006	0.03497 0.00062

#	E_a	Temp (°C)	Time (s)	^{39}Ar ± 1σ (nA)		^{37}Ar ± 1σ (nA)	
50		894 °C	900	0.00649	0.00007	0.07704	0.00081
51		911 °C	900	0.01009	0.00009	0.10722	0.00103
52		927 °C	900	0.01663	0.00009	0.16863	0.00098
53		944 °C	900	0.02669	0.00011	0.28871	0.00169
54		961 °C	900	0.02749	0.00011	0.28002	0.00125
55		979 °C	900	0.03054	0.00015	0.32897	0.00122
56		995 °C	900	0.03167	0.00012	0.36333	0.00164
57		1011 °C	900	0.03690	0.00014	0.47352	0.00177
58		1027 °C	900	0.07441	0.00020	1.06831	0.00279
59		1043 °C	900	0.09535	0.00024	1.44234	0.00380
60		1058 °C	900	0.06947	0.00021	1.08265	0.00249
61		1073 °C	900	0.04686	0.00019	0.98295	0.00355
62		1103 °C	900	0.10242	0.00023	3.39489	0.00686
63		1131 °C	900	0.09209	0.00032	2.09383	0.00687
64		1158 °C	900	0.37556	0.00074	5.27144	0.00814
65		???	900	2.05410	0.00411	31.11745	0.04321

BG-2p-1

1		399 °C	1200	0.00022	0.00004	0.00327	0.00051
2		399 °C	1200	0.00013	0.00004	0.00078	0.00048
3		422 °C	1200	0.00066	0.00005	0.00395	0.00051
4		422 °C	1200	0.00040	0.00004	0.00499	0.00051
5		445 °C	1200	0.00115	0.00005	0.00943	0.00056
6		445 °C	1200	0.00080	0.00004	0.00554	0.00059
7		469 °C	1200	0.00214	0.00005	0.01526	0.00059
8		469 °C	1200	0.00125	0.00004	0.00853	0.00056
9		491 °C	1200	0.00541	0.00007	0.04090	0.00066
10		491 °C	1200	0.00190	0.00005	0.01767	0.00058
11		514 °C	1200	0.00546	0.00007	0.04233	0.00066
12		514 °C	1200	0.00454	0.00006	0.03693	0.00063
13		536 °C	1200	0.00571	0.00006	0.06152	0.00091
14		536 °C	1200	0.00388	0.00005	0.05034	0.00083
15		558 °C	1200	0.00636	0.00007	0.09351	0.00104
16		558 °C	1200	0.00415	0.00006	0.05332	0.00060
17		580 °C	1200	0.00868	0.00007	0.10550	0.00102
18		601 °C	1200	0.01074	0.00009	0.13605	0.00124
19		622 °C	1200	0.01446	0.00009	0.19231	0.00127
20		643 °C	1200	0.01949	0.00010	0.26867	0.00144
21		623 °C	1200	0.00679	0.00006	0.09045	0.00089
22		601 °C	1200	0.00270	0.00004	0.03494	0.00073
23		580 °C	1200	0.00120	0.00004	0.01278	0.00066
24		558 °C	1200	0.00048	0.00003	0.00585	0.00054
25		536 °C	1200	0.00023	0.00003	0.00175	0.00048
26		514 °C	1200	0.00011	0.00003	0.00143	0.00050
27		491 °C	1200	0.00003	0.00003	0.00057	0.00054
28		514 °C	1200	0.00010	0.00004	0.00168	0.00044
29		536 °C	1200	0.00025	0.00004	0.00235	0.00044

#	E_a	Temp (°C)	Time (s)	^{39}Ar ± 1σ (nA)	^{37}Ar ± 1σ (nA)
30		558 °C	1200	0.00054 0.00004	0.00434 0.00046
31		580 °C	1200	0.00096 0.00005	0.01245 0.00060
32		601 °C	1200	0.00218 0.00005	0.02715 0.00062
33		622 °C	1200	0.00422 0.00005	0.05845 0.00078
34		643 °C	1200	0.00830 0.00007	0.11445 0.00086
35		665 °C	1200	0.01372 0.00010	0.19949 0.00140
36		685 °C	1200	0.02091 0.00011	0.31796 0.00174
37		705 °C	1200	0.02633 0.00012	0.40410 0.00175
38		724 °C	1200	0.03136 0.00012	0.48579 0.00180
39		744 °C	1200	0.03900 0.00015	0.60353 0.00220
40		765 °C	1200	0.04243 0.00012	0.65903 0.00247
41		784 °C	1200	0.04936 0.00016	0.76546 0.00229
42		802 °C	1200	0.05002 0.00017	0.78521 0.00253
43		821 °C	1200	0.04798 0.00016	0.75605 0.00212
44		840 °C	1200	0.04611 0.00017	0.70933 0.00195
45		857 °C	1200	0.04469 0.00017	0.68493 0.00206
46		876 °C	1200	0.04378 0.00017	0.65893 0.00218
47		876 °C	1500	0.03365 0.00012	0.49602 0.00168
48		875 °C	1500	0.02380 0.00010	0.35138 0.00168
49		802 °C	1500	0.00367 0.00005	0.04713 0.00089
50		725 °C	1500	0.00053 0.00004	0.00639 0.00054
51		685 °C	2000	0.00027 0.00003	0.00113 0.00051
52		745 °C	2000	0.00117 0.00004	0.01720 0.00060
53		803 °C	2000	0.00458 0.00006	0.06438 0.00089
54		840 °C	2000	0.01066 0.00008	0.14633 0.00121
55		876 °C	2000	0.02327 0.00012	0.33620 0.00188
56		891 °C	1200	0.01826 0.00009	0.25821 0.00122
57		911 °C	1200	0.02479 0.00010	0.33009 0.00152
58		929 °C	1200	0.03161 0.00012	0.39950 0.00184
59		945 °C	1200	0.04125 0.00014	0.44758 0.00194
60		945 °C	1203	0.02610 0.00011	0.29860 0.00168
61		945 °C	1200	0.01939 0.00010	0.21908 0.00115
62		875 °C	1200	0.00321 0.00004	0.03493 0.00075
63		803 °C	1200	0.00063 0.00004	0.00557 0.00055
64		911 °C	1200	0.00542 0.00005	0.06420 0.00079
65		927 °C	1200	0.00709 0.00006	0.09135 0.00090
66		945 °C	1200	0.01121 0.00008	0.13860 0.00109
67		952 °C	1200	0.01441 0.00007	0.14705 0.00130
68		958 °C	1200	0.01789 0.00010	0.16204 0.00145
69		964 °C	1200	0.02024 0.00009	0.16942 0.00119
70		972 °C	1200	0.02169 0.00011	0.18325 0.00128
71		978 °C	1200	0.02488 0.00010	0.19828 0.00138
72		979 °C	1200	0.01892 0.00008	0.15480 0.00111
73		979 °C	1200	0.01515 0.00011	0.12900 0.00119
74		995 °C	1200	0.02179 0.00010	0.18378 0.00131
75		1011 °C	1200	0.02289 0.00010	0.22946 0.00176
76		1042 °C	1200	0.02382 0.00012	0.38095 0.00194
77		1073 °C	1200	0.01777 0.00012	0.30229 0.00182

#	E_a	Temp (°C)	Time (s)	$^{39}Ar \pm 1\sigma$ (nA)	$^{37}Ar \pm 1\sigma$ (nA)
78		1088 °C	1200	0.01695 0.00010	0.31456 0.00247
79		1103 °C	1200	0.01422 0.00011	0.24832 0.00198
80		1103 °C	1200	0.00917 0.00008	0.16813 0.00185
81		1103 °C	1200	0.01034 0.00010	0.17031 0.00249
82		1116 °C	1200	0.51968 0.00073	9.82337 0.01163
83		1089 °C	1200	0.11588 0.00056	1.97430 0.00944

Isotope abundances given in nanoamps (spectrometer sensitivity is ~1.4 x 10^{-14} moles/nA), and corrected for ^{37}Ar and ^{39}Ar decay, with half-lives of 35.2 days and 269 years, respectively, and for spectrometer discrimination.

Average analytical blanks are ^{39}Ar = 0.0001 and ^{37}Ar = 0.0001 (nanoamps).

Temperature was controlled with approximately ± 5 °C precision and ± 10 °C accuracy.

--- indicates data are indeterminate or negligibly above the detection limit.

X indicates data were included in activation energy calculations.

CO_2 indicates the sample was heated with CO_2 laser.

??? indicates there was a problem with erratic temperature control.